THERMOELECTRIC AND HEAT FLOW PHENOMENA IN MESOSCOPIC SYSTEMS

by

JASON E. MATTHEWS

A DISSERTATION

Presented to the Department of Physics
and the Graduate School of the University of Oregon
in partial fulfillment of the requirements
for the degree of
Doctor of Philosophy

December 2011

DISSERTATION APPROVAL PAGE

Student: Jason E. Matthews

Title: Thermoelectric and Heat Flow Phenomena in Mesoscopic Systems

This dissertation has been accepted and approved in partial fulfillment of the requirements for the Doctor of Philosophy degree in the Department of Physics by:

Dr. Richard Taylor	Chair
Dr. Heiner Linke	Advisor
Dr. David Cohen	Member
Dr. John Toner	Member
Dr. David Johnson	Outside Member

and

Kimberly Andrews Espy	Vice President for Research & Innovation/ Dean of the Graduate School

Original approval signatures are on file with the University of Oregon Graduate School.

Degree awarded December 2011

© 2011 Jason E. Matthews

DISSERTATION ABSTRACT

Jason E. Matthews

Doctor of Philosophy

Department of Physics

December 2011

Title: Thermoelectric and Heat Flow Phenomena in Mesoscopic Systems

Low-dimensional electronic systems, systems that are restricted to single energy levels in at least one of the three spatial dimensions, have attracted considerable interest in the field of thermoelectric materials. At these scales, the ability to manipulate electronic energy levels offers a great deal of control over a device's thermopower, that is, its ability to generate a voltage due to a thermal gradient. In addition, low-dimensional devices offer increased control over phononic heat flow. Mesoscale geometry can also have a large impact on both electron and phonon dynamics. Effects such as ballistic transport in a two-dimensional electron gas structure can lead to the enhancement or attenuation of electron transmission probabilities in multi-terminal junctions.

The first half of this dissertation investigates the transverse thermoelectric properties of a four-terminal ballistic junction containing a central symmetry-breaking scatterer. It is believed that the combined symmetry of the scatterer and junction is the key component to understanding non-linear and thermoelectric transport in these junctions. To this end, experimental investigations on this type of junction were carried out to demonstrate its ability to generate a transverse thermovoltage. To aid in interpreting the results, a multi-terminal scattering-matrix theory was developed that

relates the junction's non-linear electronic properties to its thermoelectric properties. The possibility of a transverse thermoelectric device also motivated the first derivation of the transverse thermoelectric efficiency.

This second half of this dissertation focuses on heat flow phenomena in InAs/InP heterostructure nanowires. In thermoelectric research, a phononic heat flow between thermal reservoirs is considered parasitic due to its minimal contribution to the electrical output. Recent experiments involving heterostructure nanowires have shown an unexpectedly large heat flow, which is attributed in this dissertation to an interplay between electron-phonon interaction and phononic heat flow. Using finite element modeling, the recent experimental findings have provided a means to probe the electron-phonon interaction in InAs nanowires. In the end, it is found that electron-phonon interaction is an important component in understanding heat flow at the nanoscale.

This dissertation includes previously unpublished co-authored material.

CURRICULUM VITAE

NAME OF AUTHOR: Jason E. Matthews

GRADUATE AND UNDERGRADUATE SCHOOLS ATTENDED:
University of Oregon, Eugene, Oregon
Southern Oregon University, Ashland, Oregon

DEGREES AWARDED:
Doctor of Philosophy in Physics, 2011, University of Oregon
Bachelor of Science in Physics, 2006, Southern Oregon University

AREAS OF SPECIAL INTEREST:
Mesoscale Physics, Thermal management, Thermoelectrics, Energy Production

PROFESSIONAL EXPERIENCE:

Graduate Research Assistant, University of Oregon, 2011

Graduate Teaching Fellow, University of Oregon, 2006 - 2008

GRANTS, AWARDS AND HONORS:

NSF IGERT Fellowship, University of Oregon, 2010 - 2011

Technology Entrepreneurship Fellowship, University of Oregon, Summer 2010

NSF GK-12 Science Outreach Program, University of Oregon, 2009 - 2010

NSF GK-12 Science Outreach Program, University of Oregon, 2008 - 2009

PUBLICATIONS:

Matthews J. E., Sánchez D., Larsson. M., and Linke H., "Thermally driven ballistic rectifier," *Submitted to Physical Review Letters*, (2011), (see also e-print: arXiv:1107.3179v1 [cond-mat.mes-hall]

Hoffmann, E. A., Nilsson H. A., Matthews J. E., Nakpathomkun N., Persson A. I., Samuelson L., and Linke H., "Measuring Temperature Gradients over Nanometer Length Scales," Nano Lett. **9**, 779 (2009)

ACKNOWLEDGEMENTS

I would like to thank Stefano Roddaro, David Sánchez, and Hongqi Xu for the their valuable input through discussions and collaborations. I thank my advisor, Heiner Linke, who has helped me evolve as a physicist and a researcher. I would also like to thank my fellow graduate students, since much of what I learned as a graduate student was through them: Eric Hoffmann, Billy Scannell, Matt Fairbanks, Ian Pilgrim, Rick Montgomery, and Marcus Larsson.

I must also thank my family for their continued support. They instilled me with a sense of responsibility and drive to see that tasks are properly finished. I also thank my late grandpa for showing me what it means to be strong. Lastly I must thank my wife for her support and care. She has helped me realize what is important in my life.

To my loving wife and family.

TABLE OF CONTENTS

Chapter Page

I. INTRODUCTION 1

II. THERMOELECTRICS 8

2.1. Thermoelectric Phenomena 8

2.2. Thermoelectric Cells 9

2.3. Flux and Conservation Equations for Thermoelectric Materials 11

2.4. Heat Equation for Thermoelectric Materials 12

2.5. Thermoelectric Surface Effects 15

2.6. Derivation of Maximum Thermoelectric Efficiency for Isotropic Mediums 17

2.7. Nano-Engineered Future of Thermoelectrics 21

III. LOW-DIMENSIONAL SYSTEMS 23

3.1. Defining a Low-Dimensional System 23

3.2. Properties of Low-Dimensional Electron Systems 24

3.3. Properties of Low-Dimensional Phonon Systems 27

3.4. Landauer-Büttiker Formalism and Quantized Transport 28

3.5. Hall Voltage and Shubnikov-de Haas Oscillations 32

Chapter Page

IV. EXPERIMENTAL AND COMPUTATIONAL METHODS 35

4.1. Device Fabrication 35

4.2. Experimental Methods 41

4.3. Simulation Methods 47

4.4. Modeling Using COMSOL Multiphysics 51

V. THERMOELECTRIC RESPONSE OF A FOUR-TERMINAL BALLISTIC RECTIFIER 54

5.1. Towards a Mesoscopic Transverse Thermoelectric Response . . 54

5.2. Wafer Characterization 55

5.3. Experimental Results 57

5.4. Multi-Terminal Scattering Theory for a Non-Linear Ballistic Junction 62

5.5. Multi-Terminal Scattering Theory Applied to the Four-Terminal Junction 69

5.6. Antidot Conclusions and Outlook 75

VI. ANISOTROPIC THERMOELECTRIC MATERIALS 78

6.1. Introduction to Anisotropic Thermoelectric Materials 78

6.2. Artificial Anisotropic Materials 82

6.3. Analytic Analysis of the Anisotropic Thermoelectric System 84

6.4. Modeling the Anisotropic Thermoelectric Systems 98

6.5. Advantages of Anisotropic Thermoelectric Materials 102

Chapter Page

6.6. Conclusion 105

VII. HEAT FLOW IN INDIUM ARSENIDE NANOWIRES 106

7.1. Heterostructure Nanowire Experiments 106

7.2. Governing Equations for a Coupled Electron-Phonon System 110

7.3. Heterostructure Nanowire System Model and Heat Flow Mechanisms 119

7.4. Heating Mechanisms 127

7.5. Preliminary Fitting to Experiments 134

7.6. Electron-Phonon Simulation Results 136

7.7. Revisiting the Assumptions 141

7.8. Conclusion 143

VIII. CONCLUSION 144

8.1. Research Summary 144

8.2. Research Outlook 146

APPENDICES

A. DERIVATION OF THE FIGURE OF MERIT 148

Chapter Page

B. FABRICATION METHODS 152

B.1. Wafer Cleaning 153

B.2. Defining the Hall Bar 153

B.3. Creating the Contact Pads 154

B.4. Fine Structure EBL Procedure for InGaAs/InP 154

B.5. Procedure for Cross Linked PMMA Isolated Top Gate for InGaAs/InP 156

B.6. Electron Beam Lithography Parameters 159

C. INSTRUMENTS USED 160

C.1. Stanford SRS830 Dual-Phase Digital Lock-In Amplifier 160

C.2. DC Sources and Multimeters 162

D. HARMONICS IN AN AC DRIVEN NON-LINEAR DEVICE 163

E. LINEARIZED SOLUTION TO THE COUPLED DIFFUSIVE EQUATIONS 165

F. TABULATED THERMAL PROPERTIES 171

F.1. Silicon and Silicon Oxide 171

F.2. Gold 172

F.3. InAs and InP Lattice Parameters 173

Chapter Page

G. INAS NANOWIRE SYSTEM WITH SUPERCONDUCTING LEADS . . . 174

G.1. Experiments on InAs Nanowire with Superconducting Leads . . . 174

G.2. Model of the InAs Nanowire with Superconducting Leads . . . 175

H. NELDER-MEAD OPTIMIZATION METHOD . . . 178

REFERENCES CITED . . . 181

LIST OF FIGURES

Figure Page

1.1. Schematic of a transverse thermoelectric cell 3

1.2. SEM picture of the geometry of a typical four-terminal ballistic junction 4

2.1. Transient charge motion 9

2.2. Practical thermoelectric devices 10

2.3. A junction between two thermoelectric materials. 16

2.4. Thermoelectric module with two different materials 17

2.5. Efficiencies of commercial technologies and a few thermoelectric materials 22

3.1. Energy diagram for the InGaAs/InP heterostructure quantum well . . 25

3.2. Examples of a (a) diffusive and (b) ballistic geometry 27

3.3. Schematics of (a) electron and (b) phonon transport 30

3.4. Landau quantization in a 2DEG. 33

4.1. Heterostructure of the InGaAs/InP 2DEG wafer 36

4.2. An optical image of an etched Hall bar 37

4.3. Procedure to create an Ohmic contact between the 2DEG and chip surface 38

4.4. Dark field optical image of an etched fine structure. 39

4.5. Procedure to fabricate the insulating top gate 41

4.6. Diagram of the heating circuit connected to the right heating channel 42

4.7. Setup for measuring the lateral, V_{12}, and transverse, V_{34}, thermovoltages 45

4.8. Experimental setup to measure the junction's transverse voltage 46

Figure Page

4.9. Examples of rectangular and triangular two-dimensional meshes 48

4.10. A 1-dimensional set of linear basis functions 50

5.1. Basic geometry for the four-terminal ballistic rectifier 55

5.2. Measurement setup for the Hall, V_H, and Shubnikov de Haas, V_{SH}, measurements 56

5.3. Energy diagram for the conduction, C, and valence, V, bands 56

5.4. Schematic of D1, and SEM image of a similar device 58

5.5. First and second transverse response to a laterally applied voltage . . . 58

5.6. First four harmonics of the transverse thermovoltage 60

5.7. Transverse response due to a lateral thermal gradient 61

5.8. Second generation devices designed to measure the symmetries of the four-terminal junction 76

5.9. SEM of a two-dimensional array of triangular scatterers 77

6.1. Schematics of the two methods to create a thermoelectric cell 80

6.2. Schematic of a stacked multilayer (a) before and (b) after tilting and cutting 82

6.3. Anisotropic module for the efficiency derivation 86

6.4. 3-D geometry used for the thermoelectric COMSOL simulations 98

6.5. Efficiency of an anisotropic thermoelectric cell 100

6.6. Effects in the COMSOL simulations due to the side electrode 102

7.1. SEM picture and schematic of the HNW and the connecting leads . . . 108

7.2. Measured source and drain electron temperatures 109

7.3. Two schematics of the heat flow through a rod 112

7.4. Simulated temperature profiles across a rod 115

7.5. Schematic of the geometry created for the HNW substrate 120

7.6. Schematic of the HNW nanowire geometry and geometry used to simulate the nanowire 122

Figure Page

7.7. Simulated electron temperature profile along the nanowire axis 129

7.8. Electron heating in the cold contact due to phonon heat diffusion . . . 130

7.9. Flow chart showing how heat in the source electron reservoir can heat the drain electron reservoir 132

7.10. Electron temperature profile along the nanowire axis 133

7.11. Logic table for the nine possibilities for λ and δ 135

7.12. Relationship between C_{e} and C_{p} from the optimized HNW parameter sets 139

7.13. Relationship between n_{InAs} and Γ_{InAs} 140

7.14. Relationship between n_{InAs} and carrier density normalized Γ_{InAs} 140

B.1. Steps to fabricate a 2DEG device 152

G.1. SEM of the InAs nanowire connected to superconducting Al leads . . . 175

G.2. COMSOL geometry for the SNW simulations 177

LIST OF TABLES

Table | Page

5.1. Estimated contributions to the transverse electronic response due to lateral voltages 62

6.1. Bulk transport properties for Al and Si 99

B.1. Electron beam lithography parameters 159

F.1. Thermal conductivity as a function of phonon temperature for crystalline silicon 171

F.2. Thermal conductivity for silicon oxide as a function of phonon temperature 171

F.3. Debye temperature of gold as a function of phonon temperature 172

F.4. Lattice properties of InAs and InP 173

CHAPTER I

INTRODUCTION

In recent decades there has been a push towards expanding the world's portfolio of energy sources to encompass a greater diversity of technologies. One such technology in the mix is thermoelectrics [1], which has the potential to expand the applicable scope of waste-heat recovery systems [2]. In short, thermoelectric phenomena are solid-state devices that transduce energy between the electronic and thermal components of a system, though not as efficiently as state-of-the-art mechanical heat engines [3].

Since the initial discovery of thermoelectric effects in the early 1800s, a solid theoretical foundation has been developed. Probably the most important result from this theory was the introduction of the thermoelectric figure of merit (FOM) by Ioffe [4], which neatly describes how material properties affect the thermoelectric efficiency. Written out, the thermoelectric efficiency is given by [5]

$$\eta_{max} = \left(1 - \frac{T_c}{T_h}\right) \frac{\sqrt{1 + Z\bar{T}} - 1}{\sqrt{1 + Z\bar{T}} + \frac{T_c}{T_h}} , \tag{1.1}$$

where the FOM, $Z\bar{T}$, is

$$Z\bar{T} = \frac{S^2 \sigma \bar{T}}{\kappa} , \tag{1.2}$$

S is the thermopower, σ is the electrical conductivity, κ is the thermal conductivity, $\bar{T} = (T_h + T_c)/2$ is the average temperature, and T_h and T_c are the temperatures of the applied hot and cold thermal reservoirs. Qualitatively, the FOM can be thought of as the ratio of power generated to heat energy used. To see this, $S^2\sigma$ can be thought of as the square of a voltage multiplied by a conductance, similar to Joule heating in

a resistor. Likewise, κ can be thought of as a thermal conductance that controls the amount of heat flux through a system. Though the analogy is not perfect, it does provide some insight into the form of the FOM. The primary goal in thermoelectric research is to maximize the efficiency, and thus the FOM [2, 3]. This requires us to either increase the amount of power delivered to the load resistor—that is, increase $S^2\sigma$—or decrease the amount of heat flux through the system—that is, decrease κ.

Over the years, the FOM has steadily increased, ultimately leading to values peaking around one—corresponding to an efficiency around 5%—but no further. Due to this perceived limit, by the mid to the late 1900's some researchers started to wonder if thermoelectric research was approaching a fundamental limit to the FOM [6], in spite of any theoretical reasoning for such a limit. The advent of mesoscale engineering in recent decades has since changed this, prompting the application of both old and new ideas to further improve the FOM [7–9].

The advantages of mesoscale engineering for thermoelectric research comes from its ability to fundamentally control the transport properties of a system. One such advantage is based on the fact that the thermopower of a material is dependent on the energy dependence of the transmission function [10]. Using mesoscale engineering, this energy dependence can be tailored by utilizing quantum confinement effects. Furthermore, phonon scattering can be enhanced by introducing specific defects into a device, such as surface scattering or lattice impurities, thereby decreasing the parasitic phononic heat flow. In recent years, nanoscale engineering has given rise to experimental FOM values around 1.4 [2, 3], and theoretical values even higher yet [11, 12]. Surprisingly, devices that electronically approach the Carnot limit have even been fabricated; however, once the phononic contributions to the thermal conductivity are taken into account, the efficiency drops significantly [13].

A far less commonly studied field of thermoelectrics, whether at macro- or mesoscales, is known as transverse anisotropic thermoelectrics [14]. In contrast to the vast majority of thermoelectric materials, anisotropic materials can generate orthogonal charge and thermal fluxes, Fig. 1.1. This is of great interest when considering how the parameters in the FOM are commonly linked, such as the commonly obeyed Wiedemann-Franz law, $\kappa_e \propto \sigma$. By decoupling such parameters,

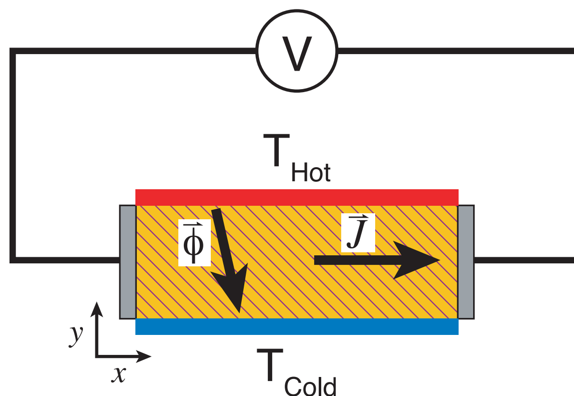

FIGURE 1.1. Schematic of a transverse thermoelectric cell. A key interest in these materials is their potential to decouple the current density, $\vec{J}$, from the heat flux, $\vec{\phi}$.

new avenues to improving the FOM are opened [15]. Over the past few decades, sporadic research on anisotropic thermoelectrics has been primarily focused on the basic characterization of bulk materials [16–19]. Not surprisingly then, research on transverse anisotropic thermoelectrics has yet to utilize nanoscale engineering as isotropic materials have.

One novel anisotropic device that utilizes mesoscale engineering is the four-terminal ballistic junction, Fig. 1.2. These devices are believed to act in a similar manner to four quantum point contacts in a bridge-like configuration [20]. As such, their behavior is highly controllable through both fabrication methods as well as gating voltages [21]. Missing from the literature, however, is experimental

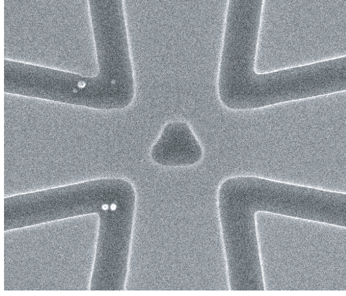

FIGURE 1.2. SEM picture of the geometry of a typical four-terminal ballistic junction.

confirmation of their ability to generate transverse thermovoltages. Also missing is a quantitative theory that details their behavior to both applied electronic and thermal gradients.

This dissertation is primarily focused on studying the fundamental physics of these four-terminal devices with an emphasis on their thermoelectric properties. To that end, I conduct proof of principle measurements on a four-terminal ballistic junction at sub-Kelvin temperatures. The goal of these experiments is to conclusively demonstrate that these junctions do indeed generate transverse thermovoltages, and that those voltages are not due to electronic effects already detailed in the literature [21–24]. To complement this research, I will also combine two previously separate theoretical results for mesoscopic systems: namely, a non-linear electronic transport theory [25] with a linear response, multi-terminal scattering approach [26]. This new theory can quantitatively describe both the non-linear voltage and linear temperature behavior of these junctions. I will also show that the non-linear response and thermal response share the same dependence on the transmission function, t, namely $\partial t/\partial E$. This shared dependence will ultimately allow me to extract the thermopower of the junction by measuring its non-linear voltage characteristics.

Surprisingly, also missing in the literature is a theory detailing the thermoelectric efficiency of an anisotropic thermoelectric material operating with the net electric current orthogonal to the thermal gradient, Fig. 1.1. A particular problem with this point is that researchers have used two incompatible forms of the anisotropic FOM [7, 16, 17, 27, 28], one of which predicts an incredible $ZT = 4$.

$$Z\bar{T}_\sigma = \frac{S_{xy}^2 \sigma_{xx}}{\kappa_{yy}} \bar{T}$$

$$Z\bar{T}_\rho = \frac{S_{xy}^2}{\kappa_{yy} \rho_{xx}} \bar{T}$$

The components of these equations are the same as for the isotropic case above, but here the anisotropy of the material must be taken into account by using matrix elements. The fault is whether the electrical conductivity or resistivity is the correct form for the FOM. By analyzing the equations governing anisotropic thermoelectric materials [14], I will show through both analytic and computational means that the correct choice is $Z\bar{T}_\rho$.

One important aspect of thermoelectric research is to understand how heat moves through a system. Having such knowledge is key to controlling heat flows in a manner that improves the thermoelectric FOM. One such heat flow is electron-phonon (e-ph) interaction in nanowires. Recent experimental temperature measurements made on two InAs nanowires can only be explained by invoking e-ph interaction. In this dissertation, I combine these measurements with finite element simulations to extract information about e-ph interaction in InAs nanowires. The results presented here suggest that the e-ph coupling strength is highly dependent on the electron carrier density.

This dissertation begins with an overview of the necessary physics on thermoelectric materials, Chapter II. Chapter III follows with the physics of low-dimensional systems, with a primary focus on two-dimensional structures. Finishing the necessary background is Chapter IV, which discusses the experimental, fabrication, and computational methods used throughout the remaining chapters.

In Chapter V, I will cover my experimental and theoretical research on the thermoelectric properties of a four-terminal ballistic junction. I will first introduce the specifics about the two-dimensional experimental system studied here; after which I will present the experimental results demonstrating the junction's transverse thermovoltage. Following this will be a theoretical derivation of a multi-terminal scattering theory extended to the weakly non-linear regime in the applied voltage. The purpose of this theory is to relate the non-linear electronic aspects of the junction with its thermoelectric properties. Finally, the derived scattering theory will be used to extract the transverse thermopower of the four-terminal ballistic junction. This chapter includes previously unpublished co-authored material.

Following the experimental findings on a transverse thermoelectric device, Chapter VI focuses on the first derivation of the transverse thermoelectric efficiency. This efficiency describes a thermoelectric device that operates with the net electric current orthogonal to the thermal gradient. Specifically, I will show that the proper thermoelectric figure of merit depends more on the electrical resistivity than the electrical conductivity.

In a slight deviation from the previous two chapters, Chapter VII will focus more on the heat flow dynamics in nanoscale thermoelectric systems. This chapter's primary goal is to investigate e-ph interaction in an InAs heterostructure nanowire. By combining experimental results with computational methods, I will show that e-ph

interaction in nanowires is an important component in understanding the dynamics of nanowire heat flow at liquid helium temperatures. This chapter includes previously unpublished co-authored material.

CHAPTER II

THERMOELECTRICS

Thermoelectric effects describe the coupling between electrical and thermal transport in a material. The two primary thermoelectric effects are known as the Seebeck and Peltier effect, which when combined with conservation laws can be used to derive all other thermoelectric heating effects [14]. After defining the Seebeck and Peltier effects, I will give an overview of deriving thermoelectric efficiency and where current research is today.

2.1. Thermoelectric phenomena

2.1.1. Seebeck effect

When a material is subjected to a thermal gradient, charge carriers will diffusively flow from the hot to cold regions; this charge flow is known as the Seebeck effect. In the open circuit case, charge carriers will accumulate in the cold region, resulting in the formation of an opposing electric field that halts the diffusive motion. These processes are schematically shown in Fig. 2.1. The voltage drop generated by this electric field is known as the thermovoltage, V_{Th}, and is proportional to the temperature differential and a material dependent constant known as the thermopower, S.

$$V_{\mathrm{Th}} = -S\Delta T \tag{2.1}$$

The thermopower of a material can be either negative or positive, depending on the dominant type of charge carriers. For an electron dominated material, n-type, $S < 0$, while for a hole dominated material, p-type, $S > 0$.

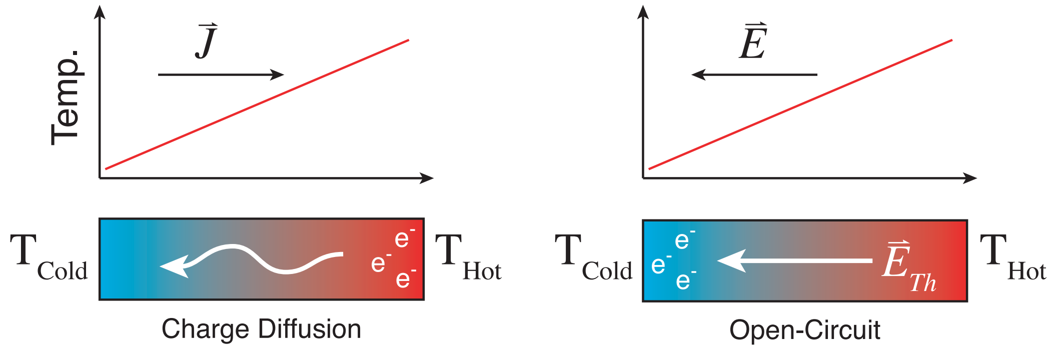

FIGURE 2.1. (Left) Charge diffusion in response to the thermal gradient. (Right) Stable open-circuit condition once the transient charge motion has ceased.

2.1.2. Peltier effect

The reverse of the Seebeck effect is the Peltier effect. Electrons can transport heat in two ways: by diffusing heat through collisions with other electrons, or by carrying the heat themselves directly to a different location. The former case is simply standard heat diffusion. The latter case is the thermoelectric effect known as the Peltier heat flux. The Peltier heat flux characterizes the amount of heat an electric current carries with it, and is given by,

$$\phi_{Peltier} = TSJ\,, \tag{2.2}$$

where T is the temperature, S is the thermopower, and J is the electric current density. The Onsager relations [29, 30] show that the thermopower here is the same as the thermopower defined in the Seebeck effect.

2.2. Thermoelectric cells

Typical thermoelectric cells are not made of a single material; instead they are constructed from two dissimilar materials, called elements here, Fig. 2.2. The reason

for this comes from the need to complete an electric circuit for the cell to be useful. The total thermovoltage generated by a cell is given by the difference between the thermovoltages generated by each element.

$$V^{Th}_{Cell} = V_1 - V_2 = -(S_1 - S_2)\Delta T \tag{2.3}$$

In order to maximize the cell's thermovoltage, Eq. (2.3) tells us to pair elements that have thermopowers that are as different as possible. The typical choice for commercial cells is one n-type and one p-type [5].

Thermoelectric cells can operate in one of two ways: as a generator, or as cooler. In the generator configuration, the Seebeck effect is utilized to generate useful electric power from an applied thermal gradient. In the the cooler configuration, the Peltier effect allows an electric current to move heat from one thermal reservoir to the other.

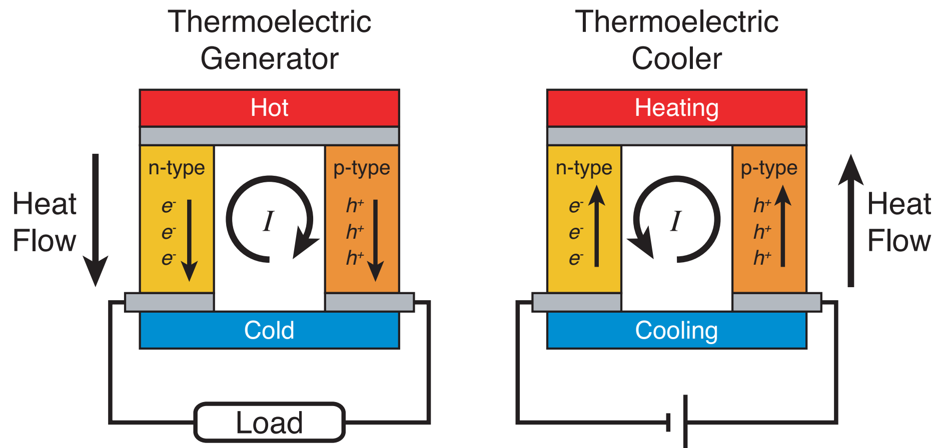

FIGURE 2.2. Practical thermoelectric devices are composed of two materials with thermopowers that are as different as possible, one n-type and one p-type. Such thermoelectric cells can be used in one of two ways, as a generator or a cooler. If a thermal gradient is applied to the thermal contacts, the cell will operate as a generator. If a current is driven through the cell, it can operate as a cooler. In the cooler mode, the direction of heat flow can be reversed by reversing the direction of the electric current.

In order to fully describe the heat flow through a thermoelectric material, and thus describe a thermoelectric generator or cooler, I must first discuss how the electric current density and heat flux are affected by the Seebeck and Peltier effects.

2.3. Flux and conservation equations for thermoelectric materials

In general, the electric current density, $\vec{J}$, and heat flux, $\vec{\phi}$, are related to the electric field, $\vec{E}$, and thermal gradient, $\vec{\nabla}T$, through the following two equations:

$$\vec{J} = \tilde{\sigma} \cdot \vec{E} - \tilde{\sigma} \cdot \tilde{S} \cdot \vec{\nabla}T \tag{2.4}$$

$$\vec{\phi} = T\tilde{S} \cdot \vec{J} - \tilde{\kappa} \cdot \vec{\nabla}T\,, \tag{2.5}$$

where $\tilde{\sigma}$ is the electrical conductivity, $\tilde{\kappa}$ is the thermal conductivity, and $\tilde{S}$ is the thermopower. These last three quantities, $\tilde{\sigma}$, $\tilde{\kappa}$, and $\tilde{S}$, will be referred to as the material transport properties throughout this dissertation. Each is represented as a matrix in order to support the description of anisotropic materials. The second term in the first equation, $-\tilde{\sigma} \cdot \tilde{S} \cdot \vec{\nabla}T$, is known as the thermocurrent, and represents the contribution to the electric current density due to the Seebeck effect. The first term in the second equation, $T\tilde{S} \cdot \vec{J}$, describes the Peltier heat flux through the material. The remaining two terms describe standard voltage-driven electric currents, and thermally-driven heat flux. Note that as a consistency check, Eq. (2.4) reduces to Eq. (2.1) in the open circuit case as it should.

In addition to the two flux equations, we also have the conservation of energy,

$$\vec{\nabla} \cdot \vec{\phi} = \vec{J} \cdot \vec{E}, \tag{2.6}$$

and conservation of charge,

$$\vec{\nabla} \cdot \vec{J} = 0. \tag{2.7}$$

Together, these four equations are sufficient to describe the linear response of thermoelectric phenomena in any material. In Chapter 6 I will use these equations to study the efficiency of an anisotropic thermoelectric generator. Before calculating the efficiency for the isotropic case, however, it is instructive to discuss Eq. (2.6) in greater depth for a thermoelectric material.

2.4. Heat equation for thermoelectric materials

For a general thermoelectric material, there are three volumetric heat sources in addition to Joule heating, all of which are obscured by the notation in Eqs. (2.4)-(2.6). To highlight these sources, I start by rewriting Eq. (2.4) as,

$$\begin{aligned} \vec{J} &= \tilde{\sigma} \cdot \left(\vec{E} - \tilde{S} \cdot \vec{\nabla} T \right) \\ \vec{E} &= \tilde{\rho} \cdot \vec{J} + \tilde{S} \cdot \vec{\nabla} T \,, \end{aligned} \tag{2.8}$$

where $\tilde{\rho} = \tilde{\sigma}^{-1}$ is the electrical resistivity. Inserting this and Eq. (2.5) into the energy conservation equation, Eq. (2.6), gives

$$\begin{aligned} \vec{\nabla} \cdot \vec{\phi} &= \vec{J} \cdot \vec{E} \\ \vec{\nabla} \cdot \left(T \tilde{S} \cdot \vec{J} - \tilde{\kappa} \cdot \vec{\nabla} T \right) &= \vec{J} \cdot \left(\tilde{\rho} \cdot \vec{J} + \tilde{S} \cdot \vec{\nabla} T \right) \\ \vec{\nabla} T \cdot \tilde{S} \cdot \vec{J} + T \vec{\nabla} \cdot \left(\tilde{S} \cdot \vec{J} \right) - \vec{\nabla} \cdot \left(\tilde{\kappa} \cdot \vec{\nabla} T \right) &= \vec{J} \cdot \tilde{\rho} \cdot \vec{J} + \vec{J} \cdot \tilde{S} \cdot \vec{\nabla} T \,. \end{aligned}$$

If I assume that the material has symmetric transport properties, $M_{jk} = M_{kj}$, the first term on the left will be equivalent to the last term on the right. Rearranging

then gives the general heat equation for a thermoelectric material.

$$-\vec{\nabla} \cdot \left(\tilde{\kappa} \cdot \vec{\nabla} T\right) = \vec{J} \cdot \tilde{\rho} \cdot \vec{J} - T\vec{\nabla} \cdot \left(\tilde{S} \cdot \vec{J}\right) \tag{2.9}$$

The left hand side of this equation represents standard heat diffusion, while the first term on the right hand side is traditional Joule heating. The second term on the right hand side is solely due to thermoelectric effects, and when expanded will show the three thermoelectric heat source terms.

For a general anisotropic material, the volume thermoelectric heat source does not vanish, $\vec{\nabla} \cdot \left(\tilde{S} \cdot \vec{J}\right) \neq 0$. This additional heat source can be expanded into three individual components as follows,

$$\begin{aligned} -T\vec{\nabla} \cdot \left(\tilde{S} \cdot \vec{J}\right) &= -T \sum_{j,k} \frac{d}{dx_j} S_{jk} J_k \\ &= -T \sum_{j,k} \left[\frac{dS_{jk}}{dx_j} J_k + S_{jk} \frac{dJ_k}{dx_j}\right] \end{aligned} \tag{2.10}$$

In general, the thermopower is a function of both space and temperature, $\tilde{S}(\vec{x}, T)$. The differential for S_{jk} is then

$$dS_{jk} = \sum_i \left(\frac{\partial S_{jk}}{\partial x_i}\right)_T dx_i + \left(\frac{\partial S_{jk}}{\partial T}\right)_{\vec{x}_o} dT,$$

which leads to a spatial derivative of

$$\frac{dS_{jk}}{dx_i} = \left(\frac{\partial S_{jk}}{\partial x_i}\right)_T + \left(\frac{\partial S_{jk}}{\partial T}\right)_{\vec{x}_o} \frac{dT}{dx_i}\,. \tag{2.11}$$

Here $\vec{x}_o$ is the spatial point at which S_{jk} is expanded about. Inserting this into Eq.(2.10) gives

$$
\begin{aligned}
-T\vec{\nabla}\cdot\left(\tilde{S}\cdot\vec{J}\right) &= -T\sum_{j,k}\left[\left(\left(\frac{\partial S_{jk}}{\partial x_j}\right)_T+\left(\frac{\partial S_{jk}}{\partial T}\right)_{\vec{x}_o}\frac{dT}{dx_j}\right)J_k+S_{jk}\frac{dJ_k}{dx_j}\right] \\
&= -T\sum_{j,k}\left[\left(\frac{\partial S_{jk}}{\partial x_j}\right)_T J_k+\left(\frac{\partial S_{jk}}{\partial T}\right)_{\vec{x}_o}\frac{dT}{dx_j}J_k+S_{jk}\frac{dJ_k}{dx_j}\right].
\end{aligned}
\tag{2.12}
$$

These three volume heating effects are known as the Peltier, Q_p, Thomson, Q_T, and Bridgman, Q_B, heat sources [14].

$$
\begin{aligned}
\text{Peltier:}\quad & Q_p = -T\textstyle\sum_{j,k}\left(\frac{\partial S_{jk}}{\partial x_j}\right)_T J_k \\
\text{Thomson:}\quad & Q_T = -T\textstyle\sum_{j,k}\left(\frac{\partial S_{jk}}{\partial T}\right)_{\vec{x}_o}\frac{dT}{dx_j}J_k \\
\text{Bridgman:}\quad & Q_B = -T\textstyle\sum_{j,k}S_{jk}\frac{dJ_k}{dx_j}
\end{aligned}
\tag{2.13}
$$

The volume Peltier heat arises from spatial inhomogeneities in the thermopower of a material, while Thomson heat is present when a material's thermopower is a function of temperature. Probably the least known is the Bridgman heat, which is only present in materials with an anisotropic thermopower.

For homogeneous, isotropic materials, all of the transport properties can be expressed as $\tilde{M} = M_o(T)\tilde{\mathbb{I}}$. Under this condition, the Peltier and Bridgman heat sources then vanish, and Eq. (2.9) reduces to the commonly known heat equation for a homogeneous, isotropic material [5].

$$
-\vec{\nabla}\cdot\left(\kappa\cdot\vec{\nabla}T\right) = \rho\vec{J}\cdot\vec{J} - T\left(\frac{\partial S}{\partial T}\right)\vec{\nabla}T\cdot\vec{J}
\tag{2.14}
$$

2.5. Thermoelectric surface effects

At the interface between two thermoelectric materials, Fig. 2.3., neither change nor heat can continuously accumulate. If either of these quantities begins to accumulate at a surface, the system will eventually reach a steady state point, where both the charge and heat flux normal to the surface are equal on either side of the interface:

$$\hat{n} \cdot \vec{J}_L = \hat{n} \cdot \vec{J}_R \tag{2.15}$$

$$\hat{n} \cdot \vec{\phi}_L = \hat{n} \cdot \vec{\phi}_R \,. \tag{2.16}$$

Here $\hat{n}$ is the unit normal to the interface, and is defined to point from material 1 to 2. Writing these equations out and rearranging terms reveals the two thermoelectric surface effects.

$$\left[\tilde{\sigma}_2 \cdot \vec{E}_R - \tilde{\sigma}_1 \cdot \vec{E}_L\right] \cdot \hat{n} = \left[\tilde{\sigma}_2 \cdot \tilde{S}_2 \cdot \vec{\nabla} T_R - \tilde{\sigma}_1 \cdot \tilde{S}_1 \cdot \vec{\nabla} T_L\right] \cdot \hat{n} \tag{2.17}$$

$$\left[\tilde{\kappa}_1 \cdot \left(\vec{\nabla} T\right)_L - \tilde{\kappa}_2 \cdot \left(\vec{\nabla} T\right)_R\right] \cdot \hat{n} = T\left[\tilde{S}_1 \cdot \vec{J}_L - \tilde{S}_2 \cdot \vec{J}_R\right] \cdot \hat{n} \tag{2.18}$$

Eq. (2.17) states that as surface charge builds up at the interface, an interfacial electric field forms that is proportional to the difference of the thermocurrents in the two materials. This interfacial thermoelectric field is distinct from the fields generated by the materials themselves, and is simply a variant of the well known surface charge effect from classical electrostatics [31].

Eq. (2.18) states that there will be a heat source or sink at the interface when the Peltier heat flux normal to the surface is not balanced. Except for special cases,

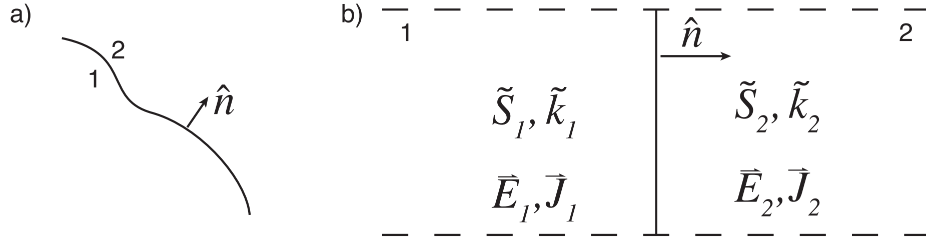

FIGURE 2.3. (a) A junction between two thermoelectric materials with an arbitrarily shaped boundary. Positive flow is directed from material 1 to 2. (b) A blown-up, infinitesimal section of the curve in (a). The dashed lines are merely figurative and do not denote physical boundaries.

this will always occur between any two materials, and is simply reflecting the fact that electric currents in different materials carry different amounts of heat. Energy is conserved in the system by a commensurate amount of heat absorbed from or evolved to the surrounding medium at the interface. This heat is known as the interfacial Peltier Heat, q_p.

$$q_p = T\left[\tilde{S}_1 \cdot \vec{J}_L - \tilde{S}_2 \cdot \vec{J}_R\right] \cdot \hat{n}. \tag{2.19}$$

The more commonly known form of q_p is found by writing Eq. (2.19) in the isotropic case, where all transport properties can be represented as scalars, $\tilde{M} = M_o\mathbb{I}$,

$$q_p = T\left[S_1 - S_2\right] \vec{J} \cdot \hat{n}. \tag{2.20}$$

The sign of q_p determines if heat is absorbed or evolved at the junction. If $q_p > 0$ then there is an excess amount of Peltier heat flowing into the junction and heat is evolved into the surroundings. In the opposite case, $q_p < 0$, there is a excess of heat flowing away from the junction and heat is absorbed from the surroundings.

2.6. Derivation of maximum thermoelectric efficiency for isotropic mediums

With all of the equations describing heat flow in a thermoelectric material now defined, we can finally turn our attention to the derivation of the efficiency for a thermoelectric cell operating as a generator. The efficiency derived here is of a thermoelectric cell consisting of two thermoelectric elements, one n-type and one p-type, each connected to hot and cold thermal baths of temperatures T_h and T_c, see Fig. 2.4. This derivation follows that from reference [5].

In order to derive the thermoelectric efficiency, we first assume the following: (1) all sides of the elements not connected to the thermal baths are perfect insulators; (2) the thermoelectrics and load resistor are the only sources of electrical resistance; (3) the material properties are isotropic constants, so the volume Peltier, Thomson, and Bridgman heats are zero; (4) there is zero contact resistance, both thermal and electrical, at all interfaces; (5) the thermoelectric elements have constant cross sectional area; and (6) the current through the system can be approximated using the open circuit voltage.

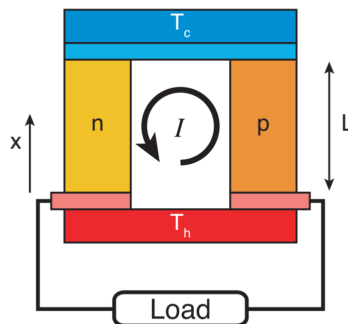

FIGURE 2.4. Thermoelectric module with two different materials for the elements, connected to hot and cold reservoirs. The length of each elements is L. The lighter red and blue components represent ideal electric contacts, $\sigma = \infty$, $\kappa = \infty$, and $S = 0$.

The efficiency of a thermoelectric generator, η, is given by the ratio of the electric power delivered to the load resistor, $P_{Load} = I^2 R_L$, to the total heat exiting the hot reservoir, Q_h.

$$\eta = \frac{P_{Load}}{Q_h} \tag{2.21}$$

The heat leaving the hot reservoir is comprised of three components: diffusive heat flow, Joule heat, and Peltier heat. We can determine Q_h by first calculating the temperature profile through the two elements using the isotropic heat equation, Eq. (2.14), which is restated here.

$$-\nabla\left(\kappa \nabla T\right) = \rho J^2 \tag{2.22}$$

The solution to this equation is

$$T(x) = \left[T_h - \Delta T \frac{x}{L}\right] + \frac{\rho J^2}{2\kappa} x \left(L - x\right) \,, \tag{2.23}$$

where I have defined $T(x=0) = T_h$, $T(x=L) = T_c$, and $\Delta T = T_h - T_c$. The amount of heat leaving the hot reservoir and entering the n-type element is then given by the element's cross sectional area, A_n, multiplied by the total heat flux at $x = 0$.

$$\begin{aligned} Q_h^n &= A_n \phi|_{x=0} \\ &= A_n \left(-T S_n J_n - \kappa_n \frac{\partial T}{\partial x}\right)_{x=0} \\ &= -A_n T_h S_n J_n + A_n \kappa_n \frac{\Delta T}{L} - A_n L \frac{\rho_n J_n^2}{2} \\ &= -T_h S_n I + \gamma_n \kappa_n \Delta T - \frac{1}{2} I^2 \frac{\rho_n}{\gamma_n} \end{aligned} \tag{2.24}$$

Here I have defined $\gamma_n = A_n/L$, and used the definition of current density $J_n = I/A_n$. In order, the terms in this equation represent the Peltier heat at the hot junction, the diffusive heat due to the applied thermal gradient, and the fraction of Joule heat generated in the element that enters the hot reservoir. The negative sign in front of the Peltier term is due to the direction of the electric current. Likewise, for the p-type element we have,

$$Q_h^p = T_h S_p I + \gamma_p \kappa_p \Delta T - \frac{1}{2} I^2 \frac{\rho_p}{\gamma_p}, \tag{2.25}$$

where the Peltier term has changed sign due to the change in direction of the electric current. Adding Eqs. (2.24) and (2.25) gives the total heat leaving the hot reservoir.

$$Q_h = T_h S I + K \Delta T - \frac{1}{2} I^2 R \tag{2.26}$$

Here I have defined the effective thermopower as

$$S = S_p - S_n, \tag{2.27}$$

the effective thermal conductance as

$$K = \gamma_p \kappa_p + \gamma_n \kappa_n, \tag{2.28}$$

and the effective electrical resistance as

$$R = \frac{\rho_p}{\gamma_p} + \frac{\rho_n}{\gamma_n}. \tag{2.29}$$

The current is estimated from the open circuit voltage and R.

$$I = \frac{V_{Th}}{R + R_L} = \frac{S\Delta T}{R + R_L} \tag{2.30}$$

Inserting Eq. (2.26) into Eq. (2.21) and solving for the maximum efficiency condition yields,

$$\eta_{max} = \eta_C \frac{\sqrt{1 + Z\bar{T}} - 1}{\sqrt{1 + Z\bar{T}} + \frac{T_c}{T_h}}\,, \tag{2.31}$$

where $\eta_C = \Delta T/T$ is the Carnot efficiency, $\bar{T} = (T_h + T_c)/2$ is the average temperature, and

$$Z\bar{T} = \frac{S^2\bar{T}}{\left((\kappa_p\rho_p)^{1/2} + (\kappa_n\rho_n)^{1/2}\right)^2} \tag{2.32}$$

is the thermoelectric figure of merit (FOM). See Appendix A for the full derivation. Like all other types of heat engines, the maximum thermoelectric efficiency is limited by Carnot efficiency, $0 \leq \eta_{max} \leq \eta_C$. From Eq. (2.31), we see that in order to increase the efficiency at given temperatures, we must increase the FOM. This is one of the main goals in thermoelectric research [2, 3, 8].

In some instances, it is more convenient to write the FOM in a form that represents a single element. The derivation for this efficiency is the same as for the two element case above, resulting only in a slight modification to the FOM [32].

$$Z\bar{T} = \frac{S^2\sigma\bar{T}}{\kappa} = \frac{S^2\bar{T}}{\rho\kappa} \tag{2.33}$$

Qualitatively, the FOM can be thought of as the ratio of power generated to heat energy used, similar to the definition for efficiency. To see this, $S^2\sigma$ can be thought of as the square of a voltage multiplied by a conductance, or Joule heating in a resistor. Likewise, κ can be thought of as a thermal conductance, which controls the amount of

heat flux through a system. Though the analogy is not perfect, it does provide some insight into the form of the FOM. If we want to increase the thermoelectric efficiency, we need to either increase the amount of power delivered to the load resistor, increase $S^2\sigma$, or decrease the amount of heat flux through the system, decrease κ.

Since phonons do not contribute to electric power generation, phonon heat flux is considered a parasitic heat flux. With this in mind, it is useful to rewrite Eq. (2.33) once more to reflect the electronic, κ_{e}, and phononic, κ_{p}, components of the thermal conductivity.

$$Z\bar{T} = \frac{S^2\sigma\bar{T}}{\kappa_{\mathrm{e}} + \kappa_{\mathrm{p}}} \tag{2.34}$$

When written in this way, two avenues of research are highlighted: to increase the power factor, $S^2\sigma$; or to reduce the phonon thermal conductivity, $\kappa_e + \kappa_p$. Many novel nanoscale engineering techniques have been developed to achieve these effects, examples of which are: superlattices [33], skutterudites [34], and rough-surfaced nanowires [35] to decrease the phonon thermal conductivity; and selective energy filtering through nanostructures such as quantum dots [36, 37]. Other research has focused on studying the thermoelectric properties of 1D-nanowires [11].

2.7. Nano-engineered future of thermoelectrics

Thermoelectric materials have a long way to go to become competitive with conventional mechanical technologies, Fig. 2.5. Current mechanical technologies have efficiencies between 10 and 50 %, depending on the operating temperature. Current thermoelectric efficiencies however, range from a few percent to 18%, again depending on the operating temperature, which limits their use to niche applications, such as deep space satellites. In order for thermoelectric materials to approach the efficiencies of current mechanical technologies, a mass producible material with a $Z\bar{T}$ value

around 3 to 4 is required [3]. Most thermoelectric materials in commercial use today have a max $Z\bar{T}$ around 1. Nanoscale engineered thermoelectric materials, having reached $Z\bar{T}$ values approaching 2, may change this situation in the near future.

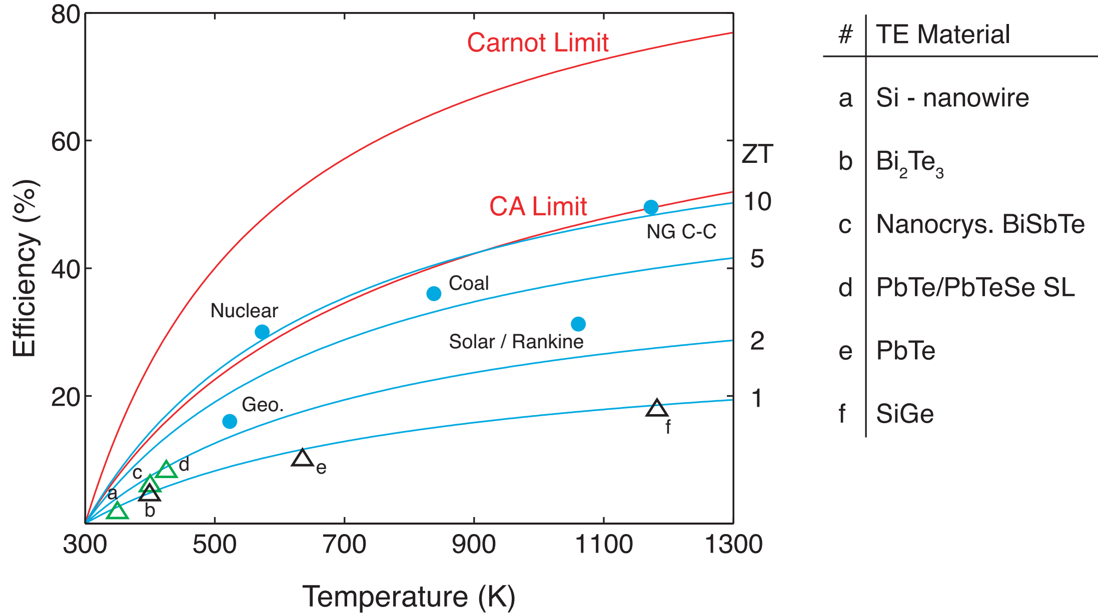

FIGURE 2.5. Efficiencies of commercial technologies and a few thermoelectric materials. The solid lines denote the efficiency calculated from Eq. (2.31) with $T_c = 300$ K for various ZT values, which are shown on the right hand side of the graph. Carnot efficiency and the Curzon-Ahlborn (CA) efficiency are shown as red lines. The filled circles label best practice power plants, NG C-C stands for natural gas combined cycle. The open triangles label current thermoelectric efficiencies, with black labeling current commercial thermoelectric technology, and green labeling state-of-the-art thermoelectrics. The type of each thermoelectric is shown on the right with its corresponding letter. The data in here is compiled from Refs. [3, 9, 33, 38–41].

CHAPTER III

LOW-DIMENSIONAL SYSTEMS

3.1. Defining a low-dimensional system

In many applications, the size of electrons allows them to be treated essentially as point particles. This description holds for scales down to roughly 100 nm, at which point quantum effects start to play a dominating role in their behavior. The specific length at which this transition occurs is around the Fermi wavelength, λ_F,

$$\lambda_F = \frac{h}{\sqrt{2m^* E_F}}\,, \tag{3.1}$$

where h is Planck's constant, m^* is the electron effective mass, and E_F is the Fermi energy.

To understand these effects, consider a cubic piece of conducting material that is initially macroscopic in size. At large scales the spacing between energy levels is much smaller than the thermal energy, $k_B T$, causing the numerous energy levels to appear continuous. If one dimension of the cube is now decreased in size, I'll call it the width, the spacing between energy levels along this direction increases. As the energy spacing increases, higher energy levels will become either thermally inaccessible or non-existent; that is, electrons at those energy levels would have enough energy to escape the material. By the time the width is comparable to λ_F, however, a quantum well will have been formed that contains only a handful of energy levels. Furthermore, if the thermal energy is much less than the energy spacing, $k_B T \ll (E_i - E_{i\pm1})$, where E_i is the ith energy level, electrons will be thermally confined to single energy levels. If only the ground state is occupied, the system is referred to as a two-dimensional

(2D) electron gas (2DEG). If any of the first few excited states are occupied then the system is considered quasi-2D.

By following this same procedure in the remaining two axes, one-dimensional (1D) and even zero-dimensional (0D) systems can be constructed. These systems are referred to as quantum wires and quantum dots, respectively. Except where noted, the rest of this chapter will primarily focus on 2DEGs, with the knowledge that everything discussed is readily transferrable to 1D and 0D systems.

Fabricating an actual 2DEG is typically carried out through the epitaxial growth of a heterostructure on the surface of a semiconductor wafer. In this dissertation, a 9 nm InGaAs quantum well was grown between layers of InP on an InP wafer (see Ch. IV and Appendix B for more details). The formation of the quantum well relies on the fact that InGaAs has a smaller band gap than the surrounding InP. For a width of 9 nm two bound states are formed in the well, Fig. 3.1. At temperatures around a Kelvin, where measurements in this dissertation are conducted, thermal confinement energies are around $k_B T \sim 0.1$ meV. Since the energy gap between the two bound states is one thousand times greater than this, in most cases the excited state will remain unpopulated.

3.2. Properties of low-dimensional electron systems

Electronic systems can be categorized by a few well known parameters: the Fermi energy, E_F; effective mass, m^*; and carrier mobility, μ, from which other electronic properties such as velocity, wavelength, carrier density, and elastic mean free path can be calculated. By utilizing these relations, the task of characterizing an electronic system is reduced to a few select measurements.

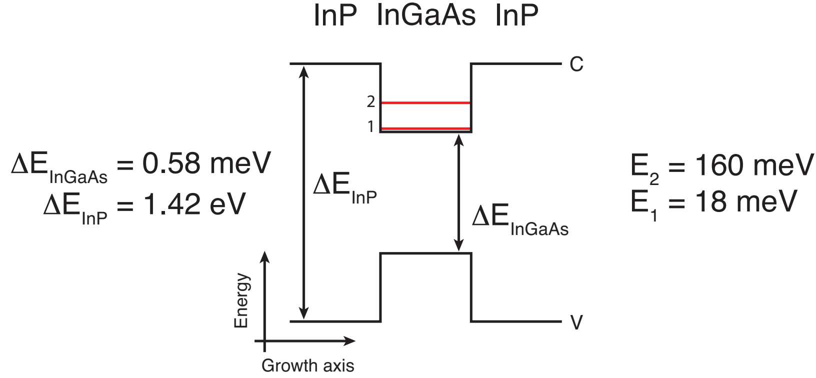

FIGURE 3.1. Energy diagram for the conduction, C, and valence, V, bands in a InGaAs/InP heterostructure. For the devices studied here, the InGaAs layer has a width of 9 nm. The two bound state energy levels of the quantum well are drawn as red lines and were calculated using the finite quantum-well approximation with an effective mass of $0.047m_e$. The quantum well energy values are measured from the bottom of the well in the conduction band. The data here was compiled from Refs. [42–44], and personal correspondence with M. Larsson at Lund University.

An example of one of these relationships is between the carrier density, n, Fermi energy, and effective mass. For 3D, 2D, and 1D systems in the spin degenerate case, this relationship is:

$$E_F = \frac{\hbar^2}{2m^*} \begin{cases} \left(3\pi^2 n_{3D}\right)^{2/3} & : D = 3 \\ 2\pi n_{2D} & : D = 2 \\ \left(\frac{\pi n_{1D}}{2}\right)^2 & : D = 1 \end{cases} , \tag{3.2}$$

where $\hbar$ is the reduced Planck constant, and n_d has units of m^{-d}. In systems with a dimensionality of two or less, E_F and n can easily be raised or lowered through doping, or electrostatic gating. For 2DEGs, the typical method is to use a combination of the two. During the fabrication process, the wafer is modulation doped a few 10's of nm away from the actual 2DEG layer. This way the carrier density can be increased, while keeping any additional impurity scattering to a minimum. The second control

comes from an electrostatic top gate that is capacitively coupled to the 2DEG. By applying a voltage to this top gate, the Fermi level in the 2DEG can be raised or lowered, thereby increasing or decreasing n. Furthermore, through the relation

$$\sigma = ne\mu \,, \tag{3.3}$$

the top gate can also change the electrical conductivity mid-experiment.

A second useful quantity in mesoscale transport is the electron mean free path, l_e.

$$l_e = \tfrac{\hbar}{e}\sqrt{2\pi n}\mu \quad : \; D = 2 \tag{3.4}$$

At room temperature, l_e is limited by inelastic scattering mechanisms, such as electron-phonon scattering, and is at most around a few 10's nm. At low temperatures, however, l_e is limited by elastic scattering events. In elastic scattering, the velocity of an electron changes in direction only, an example of which is electron scattering by lattice impurities. For system sizes larger than l_e, electrons scatter multiple times within the confines of a device, Fig. 3.2.a. Such systems are called diffusive. For systems smaller than l_e, however, electrons will predominantly interact with the system's bounding walls, Fig. 3.2.b. Between these interactions, electrons travel ballistically, and can be described using classical trajectories [45, 46]. State of the art growth techniques have achieved elastic mean free paths in the range of 10 μm's at a few Kelvin, which is much larger than current fabrication technologies, 10's nm.

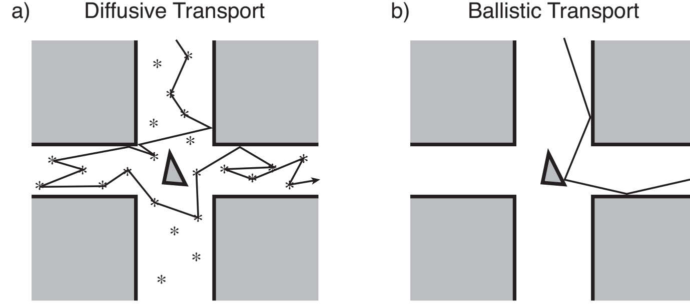

FIGURE 3.2. Examples of a (a) diffusive and (b) ballistic geometry. In the diffusive system, there are many scattering points to change either the direction or magnitude of the electron velocity. In the ballistic case, scattering is dominated by the boundaries of the geometry. If the surface features on the bounding walls are small compared to λ_F, specular reflection takes place and the entire trajectory can be described using a classical description.

3.3. Properties of low-dimensional phonon systems

Just like electrons, phonons can be confined and made to undergo ballistic transport. The main change between the two dynamics is the condition for confinement. To determine if a phonon system is confined, we need to determine when phonons no longer travel along a particular spatial axis. This condition can be calculated from Boson statistics, which states that the number of phonons, N, at energy E_{ph} in a material with temperature T is

$$N(E_{ph}, T) = \frac{1}{\exp\left(\frac{E_{ph}}{k_B T}\right) - 1} \,. \tag{3.5}$$

The phonon energy is given by

$$E_{ph} = \hbar\omega = \frac{hc}{\lambda_{ph}} \,, \tag{3.6}$$

where ω is the phonon angular frequency, c is either the longitudinal or transverse speed of sound, and λ_{ph} is the phonon wavelength. Note the the second equality only holds for low temperature acoustic phonons. To determine N in the low temperature limit, where $\hbar\omega \leq k_B T$ and T is on the order of a few Kelvin, we must first determine λ_{ph}.

The quantum theory of crystal lattices tells us that λ_{ph}, and thus E_F, can only take on discrete values [42]. For a crystal with dimensions of L_x, L_y, and L_z, those values are given by

$$\frac{2\pi}{\lambda_{ph}} = |\vec{k}_{ph}| = \sqrt{\left(\frac{\pi n_x}{L_x}\right)^2 + \left(\frac{\pi n_y}{L_y}\right)^2 + \left(\frac{\pi n_z}{L_z}\right)^2}, \tag{3.7}$$

where $\vec{k}_{ph}$ is the phonon wave vector; the n_i are the phonon quantum numbers, and take on integer values between $\pm L_i/a$; and a is the lattice constant of the crystal.

For phonon confinement, we need to determine the number of phonons in the lowest non-zero energy state along a particular direction. Once the total number of phonons along this direction drops well below one, the system is said to be confined in this direction. As an example, to determine if phonons are confined along the x-axis, the lowest energy state is given by $E_{ph}(n_x = 1, n_y = n_z = 0)$. If the average number of phonons in this state is less than one, as calculated by Eq. (3.5), then phonons are confined along the x-axis.

3.4. Landauer-Büttiker formalism and quantized transport

The Landauer-Büttiker formalism relates the currents and voltages through each terminal in a multi-terminal, phase-coherent, ballistic device [47], and has been an extremely useful theoretical tool in analyzing mesoscopic systems [26, 48–50]. Here,

'terminal' refers to the number of electrical contacts made to a device; an example of a four terminal device is shown in Fig. 3.2.b. The theory posits that electrons emitted from a terminal with electrochemical potential, μ, and temperature T, are described by the Fermi-Dirac distribution, Fig. 3.3.a,

$$f(E-\mu,T)=\frac{1}{\exp\left(\frac{E-\mu}{k_BT}\right)+1} \tag{3.8}$$

where E is the electron energy, and k_B is Boltzmann's constant. Once emitted from a terminal, electrons elastically scatter around the device area until finally leaving through another terminal, which can include back scattering into the emitting terminal. The probability of an electron being emitted by one terminal, α, and collected by another, β, is given by the energy-dependent transmission function $t_{\alpha\beta}$(E). From here it is instructive to consider only two of the terminals, Fig. 3.3.a, which I will continue to label and refer to as α and β. The net current leaving α and entering β is given by

$$I_{\alpha\to\beta}=\frac{2e}{h}\int_0^\infty dEf(E-\mu_\alpha,T_\alpha)t_{\alpha\beta}(E)\,. \tag{3.9}$$

Similarly, the current leaving β and entering α is given by

$$I_{\beta\to\alpha}=\frac{2e}{h}\int_0^\infty dEf(E-\mu_\beta,T_\beta)t_{\beta\alpha}(E)\,. \tag{3.10}$$

The net current in α due to β is given by the difference between these two currents.

$$\begin{aligned}I_{\alpha\beta}&=I_{\alpha\to\beta}-I_{\beta\to\alpha}\\&=\frac{2e}{h}\int_0^\infty dE\left[f(E-\mu_\alpha,T_\alpha)t_{\alpha\beta}(E)-f(E-\mu_\beta,T_\beta)t_{\beta\alpha}(E)\right]\end{aligned} \tag{3.11}$$

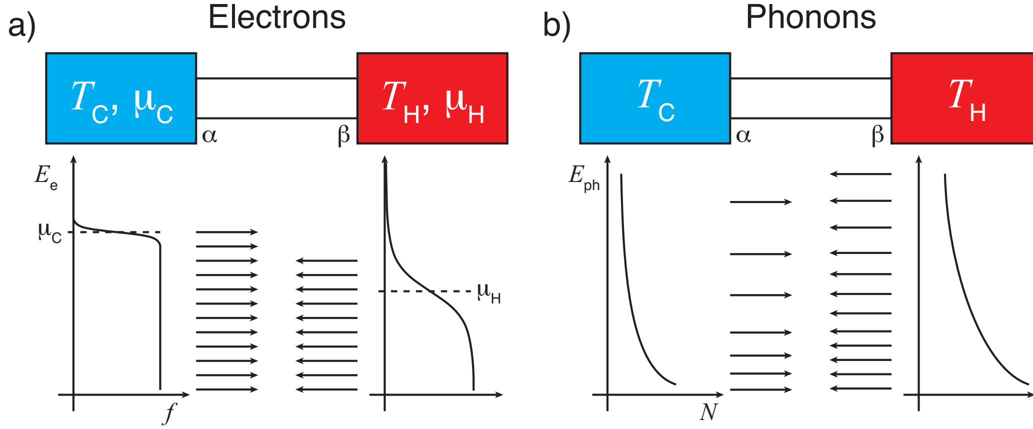

FIGURE 3.3. Schematics of (a) electron and (b) phonon transport through a fully-ballistic junction between two thermal baths of temperatures T_H and T_C. Note that additional reservoirs are not drawn here, but could be present in the system. The graphs below the baths depict the relevant statistics: the probability, f, of an electron energy state, E_e, being occupied; and the number of phonons, N, at energy E_{ph}. Arrows indicate particles leaving the thermal reservoirs. For electrons, both the electrochemical potentials, $\mu_{(\text{C,H})}$, and temperatures must be taken into account to determine the net flow of electrons. The net flow of phonons will always be directed towards the cold reservoir.

Gauge invariance requires that the transmission probabilities be equal, $t_{\alpha\beta} = t_{\beta\alpha}$, which simplifies this to

$$I_{\alpha\beta} = \frac{2e}{h} \int_0^\infty dE \left[f(E - \mu_\alpha, T_\alpha) - f(E - \mu_\beta, T_\beta) \right] t_{\alpha\beta}(E) \,. \tag{3.12}$$

Finally, to determine the total current through α, I_α, we simply sum β over all of the terminals.

$$I_\alpha = \frac{2e}{h} \sum_\beta \int_0^\infty dE \left[f(E - \mu_\alpha, T_\alpha) - f(E - \mu_\beta, T_\beta) \right] t_{\alpha\beta}(E) \,. \tag{3.13}$$

Eq. (3.13) is the Landauer-Büttiker formalism for electron flow in a multi-terminal device. If the $t_{\alpha\beta}(E)$ are known, then Eq. (3.13) can be used to calculate the electrical

conductance, G; thermopower, S; and, with a slight modification [32], the thermal conductance, K, of any coherent ballistic junction. It is this generality that makes the theory so useful to a multitude of applications.

This same analysis can be applied to one-dimensional phonons, which leads to the phonon version of the Landauer-Büttiker formalism [51].

$$\dot{Q}_\alpha = \frac{1}{2\pi} \sum_\beta \sum_\gamma \int_0^\infty dk\ \hbar\omega_\gamma(k) v_\gamma(k) \left[N(\hbar\omega_\gamma(k), T_\alpha) - N(\hbar\omega_\gamma(k), T_\beta) \right] \zeta_{\alpha\beta}(\omega_\gamma(k)) \,. \tag{3.14}$$

Here $\dot{Q}_\alpha$ is the phonon energy leaving the αth terminal per unit time; $\omega_\gamma(k)$ and $v_\gamma(k)$ represent the phonon dispersion relations and velocities, respectively; and $\zeta_{\alpha\beta}$ is the phonon transmission function between the αth and β^{th} terminals. A general two terminal schematic of this is shown in Fig. 3.3.b.

At low temperatures both Eqs. (3.13) and (3.14) lead to quantized conductances, that is, the unit of conductance contributed by each carrier mode. The quantum of electrical conductance is

$$G = \frac{2e^2}{h} \,, \tag{3.15}$$

and the quantum of thermal conductance is

$$K = \frac{\pi^2 k_B^2 T}{3h} \,. \tag{3.16}$$

Though electrons and phonons obey different statistics, they have the same quantized thermal conductance [51, 52]. This was quite a surprise at its discovery, but has since been explained as a universal phenomenon that is independent of the carrier statistics [53–55].

3.5. Hall voltage and Shubnikov-de Haas oscillations

A common method to measure the charge carrier density, n, in macroscopic conductors is by measuring the Hall voltage they generate. For small magnetic fields, this same method can be used on 2DEG systems. Like the macroscopic case, a current is first driven through the 2DEG along the x-axis, I_x. The application of a magnetic field perpendicular to the plane of the 2DEG, B_z, will then cause electron trajectories to tend toward one side of the material, specifically along the y-axis. The difference in voltage established by the buildup of charge along the y-axis, V_y, is known as the Hall voltage. By measuring each of these quantities, the two-dimensional carrier density can be determined through the relation

$$\frac{V_y}{I_x B_z} = -\frac{1}{ne} \, . \tag{3.17}$$

Note that this equation is strictly for 2DEGs. The resulting sign of n informs us if the system is dominated by electrons, $n < 0$, or holes, $n > 0$.

Starting at magnetic fields around 0.5 to 1 Tesla, the above equation no longer holds for 2DEGs due to an increasing quantization of the electron energy levels. These energy levels, known as Landau levels, can be written as [42, 44]

$$E(k_z, \nu) = \frac{\hbar^2 k_z^2}{2m^*} + \left(\nu + \frac{1}{2}\right) \hbar\omega_c \qquad \nu = 0, 1, 2, \cdots \tag{3.18}$$

where k_z is the electron wave vector in the confined direction, $\omega_c = eB/m^*$ is the cyclotron frequency, and ν denotes the Landau level. The result of the magnetic field is to reorganize the electron density of states to Lorentzian functions about these discrete energy levels, Fig. 3.4.

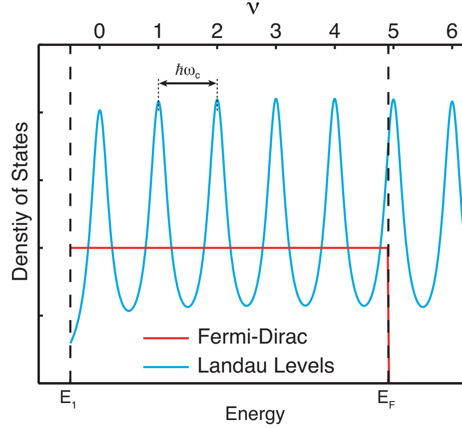

FIGURE 3.4. Landau quantization in a 2DEG. The effect of the magnetic field is to center electronic states about discrete energy levels separated by $\hbar\omega_c$. As the magnetic field strength increases, the density of states at the Fermi energy oscillates, which can be seen in transport measurements.

As can be seen from ω_c and Eq. (3.18), the spacing between successive Landau levels increases with the magnetic field strength. A consequence of these shifting levels is an oscillation in the density of states at the Fermi energy, known as Shubnikov-de Haas (SdH) oscillations. Since transport properties are commonly dependent on the number of states at the Fermi energy, quantities like the electrical resistivity will also oscillate as a function of magnetic field. The νth Landau level will cross the Fermi energy when there are exactly ν landau levels at or below the Fermi energy:

$$\begin{aligned} \nu &= \frac{E_F}{\hbar\omega_c} \\ &= \frac{\pi\hbar n}{eB} \,. \end{aligned} \tag{3.19}$$

These oscillations are ultimately the origin of the quantum hall effect as well as the aptly named Shubnikov-de Haas oscillations of the longitudinal resistivity, ρ_{xx}. By identifying the peaks in ρ_{xx} as a function of the magnetic field, we can use Eq. (3.19)

to again extract the carrier density. However, unlike the carrier density from the Hall voltage, which yields the total carrier density in the 2DEG, the SdH measurements can obtain the density for each two-dimensional sub-band in the 2DEG [44] by identifying different oscillation frequencies in ρ_{xx}. Comparing these two measurements is an excellent way to determine if any sub-bands beyond the ground state are populated.

One last quantity that we can determine from the ρ_{xx} measurement is the carrier mobility, μ. This can easily be calculated through Eq. (3.3) once the carrier density and zero-field longitudinal resistivity, $\rho_{xx}(B=0)$, have been measured.

$$\sigma(B=0) = \frac{1}{\rho_{xx}(B=0)} = ne\mu\,. \tag{3.20}$$

In the end, by measuring the Hall voltage and SdH oscillations in ρ_{xx}, we can determine the carrier density, and carrier mobility. Typical 2DEG values for these quantities are around 10^{12} cm^{-2} and 10^{5} cm^{2}/Vs. Assuming that we also know the effective mass, which is easily obtainable from literature, these three quantities allow us to calculate the elastic mean free path, as well as any Fermi value. If no additional sub-bands are occupied, these measurements could theoretically be done using only the SdH measurement; however, additional populated sub-bands are not always detectible in SdH oscillations [44]. Therefore, in order to confirm that higher energy sub-bands are not populated, the Hall measurement must be included.

CHAPTER IV

EXPERIMENTAL AND COMPUTATIONAL METHODS

The projects described in this dissertation use low-temperature electronic and thermoelectric measurements, Chapter V, as well as computational simulations of heat flow and thermoelectric phenomena, Chapters VI and VII. The first two sections of this chapter will cover the device fabrication and experimental techniques used in the four-terminal ballistic rectifier research in Chapter V. The final two sections will discuss simulation methods and COMSOL Multiphysics, both of which are used in Chapters VI and VII.

4.1. Device fabrication

The measurements conducted in this dissertation were carried out on two-dimensional electron gas (2DEG) devices embedded in InGaAs/InP heterostructure wafers. These heterostructures are grown on the surface of InP wafers at Lund University using metal organic vapor phase epitaxy. The composition of the heterostructure and the purpose for each layer are, Ref. [46, 56, 57]: a 50 nm buffer layer of not intentionally doped (NID) InP smooths out any imperfections on the initial wafer; a 9 nm $In_{0.77}Ga_{0.23}As$ layer defines a quantum well in the growth direction that becomes the 2DEG plane; a 20 nm NID InP spacer layer to separate the quantum well from the dopant layer; a 2 nm Si-doped InP layer provides excess electrons to increase the carrier concentration in the quantum well; all covered by a 20 nm NID InP capping layer. This structure is shown in Fig. 4.1. Wafers grown in this material and manner are nearly perfectly flat, offer high electron mobilities

($\mu_e > 10^5$ cm^2/Vs, Ref. [56, 57]), and can be chemically etched without the risk of surface oxidization when exposed to air.

All of the fabrication steps used to create the device geometry on the 2DEG wafer are done using electron beam lithography (EBL), wet chemical etching, metallization, and rapid thermal annealing. The general steps to fabricating a 2DEG device are described in the following sections, while the step-by-step fine details are relegated to Appendix B.

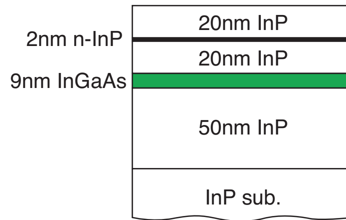

FIGURE 4.1. Heterostructure of the InGaAs/InP 2DEG wafer grown using metal organic vapor phase epitaxy. The 2DEG is located in the green layer of InGaAs. The thin black layer is the Si-doped InP layer used to increase the 2DEG carrier concentration.

4.1.1. Fabricating the Hall bar

After the heterostructure growth, the wafer is cleaved to produce 3 mm $\times$ 4 mm pieces, referred to as the "chip" from here on. Nine individual devices can easily be made on each cleaved chip by patterning the surface with an array of Hall bars. Defining a Hall bar is a method to isolate a section of the 2DEG from the rest of the wafer, and typically consists of a rectangular section connected to some number of macroscopic contact pads. The contact pads act as the electrical interface between the relatively large measurement instruments and the mesoscale electronics that will later be defined inside the Hall bar area.

The process of creating a Hall bar, Fig. 4.2., is started by first cleaning the surface of the chip by rinsing in acetone, then isopropyl alcohol (IPA), and finally dried with dry N_2 gas. Once the surface is free of debris, two layers of ZEP 520 A7 resist are deposited on the surface through spin coating. The resist layers are exposed using EBL and developed in oxylene. Once developed, the wafer is etched for 2 minutes in

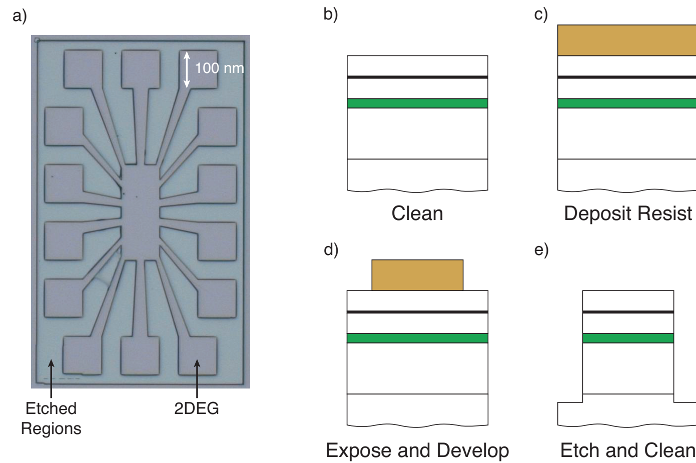

FIGURE 4.2. (a) An optical image of an etched Hall bar. The 100 μm squares along the edge are the contact pads. The Hall bar itself is the central rectangle. The steps to creating a Hall bar are to (b) clean the surface; (c) spin-coat the resist on; (d) expose the Hall bar pattern into the resist using EBL, followed by development in oxylene; and (e) etch the hall bar pattern into the surface and re-clean. The brown layers here are the resist, and are not to scale.

a solution of hydrobromic acid, nitric acid, saturated bromine water, and deionized water. The goal is to etch completely through the bottom InP buffer layer to ensure that there are no electrical connections between the Hall bar and the surrounding medium. This acid solution will also attack the resist, which is why two layers were deposited. Once etching is complete, the remaining resist on the chip is removed and the surface is again cleaned for the creation of the Ohmic contact pads.

4.1.2. Creating Ohmic contact pads

Electrical connections to the contact pads can now be made to interface with the Hall bar. It is not enough to simply place probes on the surface of the contact pads. Doing so would create metal-semiconductor contacts that act like Schottky diodes, which have the undesired property of non-linear I-V characteristics. Schottky contacts are avoided by metallizing the surface of the contact pads with a layering

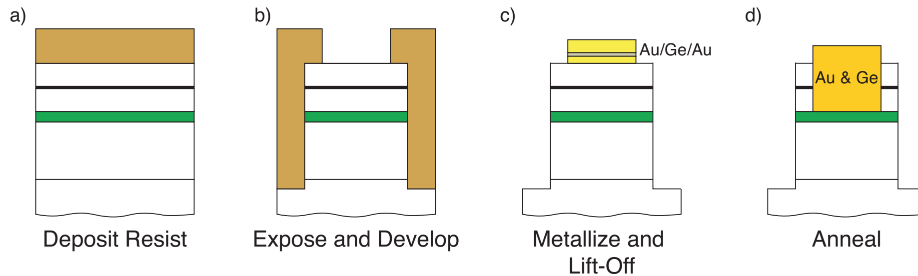

FIGURE 4.3. Procedure to create an Ohmic contact between the 2DEG and chip surface: (a) spin-coat the surface with PMMA resist; (b) expose the contact pad regions using EBL, and develop; (c) metallize the contact pad regions with a Au / Ge / Au layering; and (d) rapidly thermal anneal the chip to diffuse the Au and Ge into the surface. Note that the layer thicknesses are not to scale. The brown layers in (a) and (b) are the resist. The yellow and gold layers in (c) and (d) are the Au and Ge layers.

of 400 Å Au / 200 Å Ge / 1600 Å Au, performing standard lift-off, and diffusing the metal into the top InP layers by rapid thermal annealing, Fig. 4.3. This process creates a highly-doped Ohmic region between the 2DEG and the surface that acts as the electrical interface to the fine structured electronics of the Hall bar.

4.1.3. Defining the fine structures

The actual geometry of the device to be studied is defined by wet etching the device's boundaries into the chip's surface. This process consists of writing single pixel lines through EBL to define the devices edges, as well as the channels leading

between the device and contact pads. An example of a fine structure etch is shown in Fig. 4.4.a. Single pixel lines are used instead of exposing whole areas of the Hall bar to decrease the EBL writing time. Once the device pattern has been developed, the surface is etched in a solution of hydrobromic acid, nitric acid, saturated bromine water, and deionized water for 15 seconds, Fig. 4.4.b-d.

Though similar to the Hall bar etching procedure, the fine structure etch requires a tighter EBL focus to allow the 20 nm pixels in the single pixel lines to be resolved. A bad focus leads to either an underexposed resist, at which point the etching solution will not reach the surface, or larger pixel sizes if the exposure time is increased accordingly. The fine structure etch also requires a weaker acid solution to more accurately control the etched depth. The goal here is to etch through the 2DEG to ensure that adjacent regions are electrically isolated, known as deep etching. The compromise for ensuring electrical isolation is a decreased etching resolution: as the etched depth increases, so to does the etched width. For structures much larger than the etch depth, this is of little consequence. However, for EBL-exposed structures

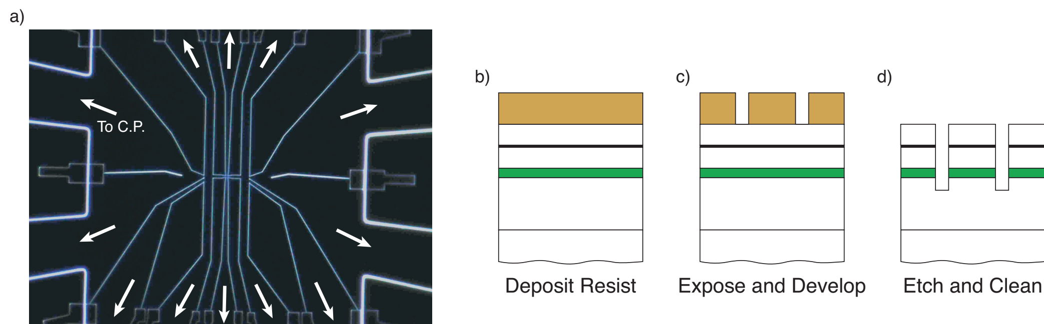

FIGURE 4.4. (a) Dark field optical image of an etched fine structure. The thin white lines are the result of the fine structure etch, while the thicker white lines are the result of the Hall bar etch. The white arrows show the paths leading to the contact pads (C.P.). The fine structure etch is procedure is: (b) spin coat on a resist layer; (c) expose the resist using EBL, and develop; and (d) etch the surface using an acid solution and remove the resist layer.

comparable in size or smaller than the etch depth, single pixel lines for example, the minimum etched width is roughly twice the etched depth.

With the fine structure etches complete, the Hall bar device can finally be measured on. Such measurements, however, would be limited to a single Fermi energy. Many mesoscopic measurements require the ability to change the Fermi-energy, some of which are: changing the electron energy levels in quantum dots, Ref. [57]; low dimensional conductance measurements, Ref. [58]; and coulomb blockade measurements, Ref. [59]. This functionality can be achieved by means of a top gate.

4.1.4. Electrically isolated top gate fabrication

The implementation of a top gate allows the Fermi energy of the 2DEG directly below the top gate to be manipulated through applied DC voltages. If a negative voltage is applied, electrons are pushed away from the region below the top gate. At a sufficiently negative voltage, no electrons will occupy the region under the top gate, and this area is said to be depleted.

A metal top gate cannot be deposited directly on the InP surface since a Schottky contact would form. A top gate made in this fashion would leak current into the 2DEG, and adversely affect any measurements being performed. An insulating layer of resist between the surface and the top gate prevents this from occurring. Unlike the etching procedure, where the EBL exposure process causes the resist to become soluble, the insulating layer of resist is overexposed to the point where its molecular chains become linked, Fig. 4.5.a-b. This creates an insoluble layer of resist that acts as an insulating barrier between the top gate and 2DEG. Once the insulating resist is

in place, the top gate is defined by exposing and developing one final layer of resist, evaporating Ti then Au onto the surface, and performing standard lift-off, Fig. 4.5.c-e.

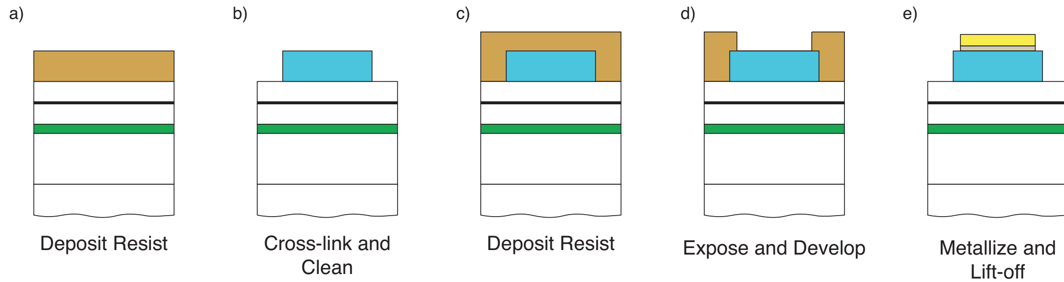

FIGURE 4.5. Procedure to fabricate the insulating top gate: (a) Spin coat on the first resist to create the insulation layer; (b) overexpose the insulated layer pattern to the point of cross-linking, followed by cleaning; (c) spin coat on the second resist layer for metallization; (d) expose the top gate pattern, and develop; (e) deposit the Ti and Au layers for the top gate, and perform standard lift-off. The resist layers are colored brown, the cross-linked insulation layer are blue, and the metal layers are yellow.

4.2. Experimental methods

In this dissertation, AC signals were used to apply currents, voltages, and thermal gradients. Most applied and measured voltages were carried out through Stanford Research Systems (SRS) Model SRS830 dual-phase digital lock-in amplifiers (LI). The exceptions are gate voltages and DC-shifts, described below, that were applied using Yokogawa voltage sources and measured with a Keithley 2000 Digital Multimeter. All instruments used in this dissertation, and their relevant functions, can be found in Appendix C.

4.2.1. Applying thermal gradients to mesoscopic systems

Generating thermal gradients in mesoscopic systems typically involves evolving Joule heat somewhere in the system. This heat can either be evolved in the actual

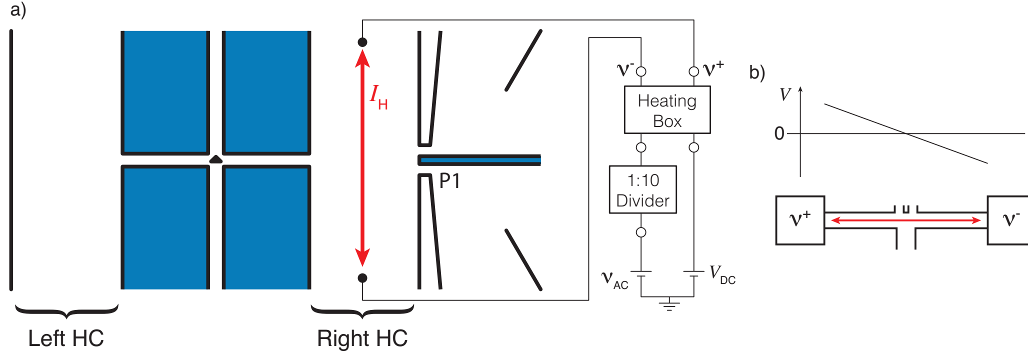

FIGURE 4.6. (a) Diagram of the heating circuit connected to the right heating channel (HC). The heating current, I_{H}, raises the electron temperature in the channel thermally biasing the junction. An AC supply voltage is fed into the heating box through a 1:10 voltage divider. The heating box further reduces the input AC signal to 4.928×10^{-4} of the original amplitude, ν_{AC}, and outputs two signals, $\nu^{\pm}$. One of these signals is in phase with ν_{AC}, while the other has been phase shifted by 180°. The heating current is then generated by connecting these two voltages to the ends of one of the heating channels; the right heating channel here. In (b) the resulting voltage profile due to the two voltages from the heating box is sketched along the heating channel. Since ν^{+} and ν^{-} are out of phase, a zero voltage point will occur at some point in the HC. Using contact P1 as a voltage probe, the amplitude of ν^{-} is adjusted through a variable voltage divider, integrated into the heating box, until the 1ω voltage at P1 is minimized. After minimizing the 1ω component, any remaining DC component at P1 is minimized by a DC voltage shift, V_{DC}, applied to the heating box. Assuming $\nu^{\pm}$ are equal in magnitude and ignoring phase, the final output of heating box is $\nu^{\pm} = a\nu_{\mathrm{AC}} + bV_{\mathrm{DC}}$, where $a = 4.928 \times 10^{-4}$ and $b = 9.2 \times 10^{-3}$.

electric circuit to be measured on, or in a heating circuit electrically isolated from the measurement circuit. The measurements in this dissertation heat the measurement circuit directly, Fig. 4.6. The important criterion to implement the direct heating method is to bias the junction thermally and not electrically.

Thermal biasing without an electrical bias is achieved by using two heating voltages, $\nu^{\pm}$, generated from a single 37 Hz input signal, ν_{AC}. The circuit diagram describing the generation of these two heating voltages can be found in Ref. [13]. One of these heating voltages is phase shifted by 180°, after which both are applied to the ends of the electronic path to be heated, the left and right heating channels. With

the heating circuit having a time constant around 0.1 ms or less, corresponding to a frequency of 10 kHz, the voltage profiles in the heating channels form at a much faster rate than the rate at which the applied heating voltages change. It is sufficient then to analyze the voltage profile in the heating channel due to the two AC heating voltages at any single instant in time, Fig. 4.6.b. If ν^+ and ν^- are perfectly out of phase, and no additional phase shifting occurs, then the two voltages will always have opposite polarities. It will always be true then, that somewhere along the heating channel, the voltage will be equal to zero. This point can be moved to the junction terminal, thus minimizing the applied electrical bias, by manipulating the amplitude of ν^- via a variable resistor located in the heating box. The correct amplitude for ν^- is found be minimizing the 1ω signal measured using the side voltage probe P1.

In the ideal case, where the system responds linearly, the voltage at P1 is zero as described above; however, non-linearities in the circuit can produce DC components at the junction. Examples of non-linear sources are: temperature dependent resistivities; changes in carrier concentration, and thus electrical conductivity, due to the applied electric potentials; and imperfect circuitry in the heating box. Appendix D details how non-linearities can generate DC and higher harmonic signals. A DC off-set voltage, V_{DC}, simultaneously applied to both ν^+ and ν^- is used to cancel out any DC voltages measured at P1.

All of the junction terminals not connected to the channel carrying the heating current were either floating or connected to a high impedance voltage probe. As such, since zero or negligible electric current flows through these terminals, the voltage drop between the junction and the contact pads is negligible.

4.2.2. Measuring the lateral and transverse thermovoltage due to laterally applied thermal gradients

As stated in the introduction, a thermal gradient across a material will generate a thermovoltage. At the mesoscale, thermovoltages are commonly accompanied by additional voltage drops. These additional voltages can be due to either electric current flow, or other thermovoltages. If the thermoelectric element has an electric current flowing through it, the thermovoltage is isolated by applying a bias voltage along with the thermal gradient. Assuming there are no additional voltage sources, the bias voltage at which the electric current through the circuit is zero is the open-circuit thermovoltage. In the open-circuit case, the thermovoltage is simply measured as the voltage drop across the material.

Any thermal gradient generated via Joule heating, $Q_{\mathrm{J.H.}}$, will be proportional to the square of the heating current, $Q_{\mathrm{J.H.}} \propto I^2 R$. If the heating current is AC the thermal gradient will have a DC component and a component at twice the frequency of the heating current, see Appendix D.

$$V_{\mathrm{Th}} \propto \Delta T \propto Q_{J.H.} \propto 1 + \cos(2\omega t) . \tag{4.1}$$

When using AC heating currents the thermovoltage must be determined by measuring either the DC component or response at the second harmonic of the the heating frequency. In this dissertation, thermovoltages were measured using the second harmonic of the heating signal.

Since negligible electric currents were flowing through the junction terminals, the thermovoltages were measured simply by measuring the lateral and transverse voltage drops across the junction. The measurement setup is shown in Fig. 4.7. Using the

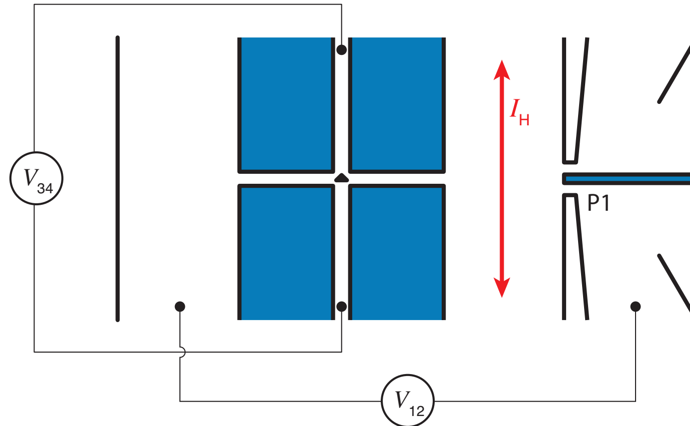

FIGURE 4.7. Setup for measuring the lateral, V_{12}, and transverse, V_{34}, thermovoltages due to a heating current I_{H}. For more details on applying the heating current, see Fig. 4.6. Each voltage probe here corresponds to multiple LIs, each measuring a different frequency.

connections shown here, the first and second harmonic of V_{12} and V_{34} were measured simultaneously via multiple LI's and the LI's HARM setting, see Appendix C for an explanation of the LI's HARM function.

For the measurement of V_{12}, the right connection in Fig 4.7. must be connected to the junction through the voltage probe P1, instead of the main side channel, to avoid unwanted voltage drops due to the heating current. Since P1 was initially constructed to function as a quantum point contact, there is the possibility for it to produce an additional thermovoltage that would interfere with measuring V_{12}. Measurements on a similar system show P1 to generate a thermovoltage around 100 nV at a heating voltage of 0.5mV.

A second pair of thermovoltages that are present are the 2DEG thermovoltages between the heating channel and the contact pads for V_{12} and V_{34}. These thermovoltages are of little concern though, since the voltages cancel out when the voltage difference between contact pairs is measured.

4.2.3. Measuring the transverse response to laterally applied voltages

The junctions studied in this dissertation are expected to exhibit non-linear electrical characteristics due to symmetry breaking, Ref. [23]. To measure these non-linearities, both the first and second harmonics of all voltages must be characterized.

For the non-linear electrical measurements, the circuit was driven using a LI

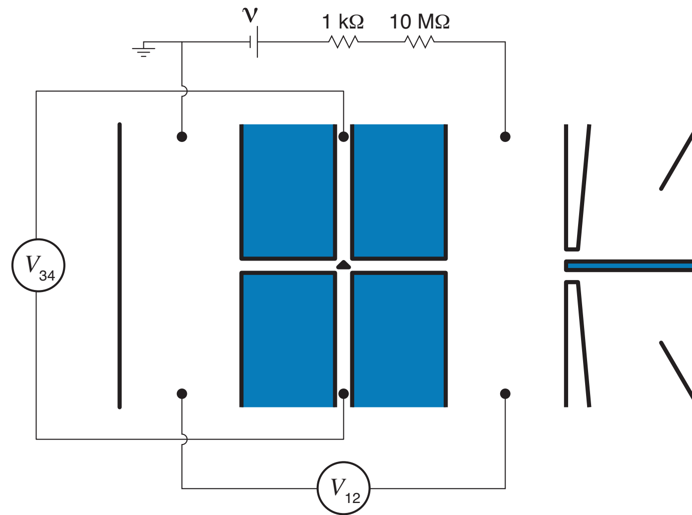

FIGURE 4.8. Experimental setup to measure the junction's transverse voltage response to a laterally applied voltage. Using the source voltage from a LI, ν, and a 10 MΩ ballast resistor, a lateral current was applied to the junction. The current through the circuit was determined by measuring the voltage drop across a 1 kΩ resistor and Ohm's law. The lateral, V_{12}, and the transverse, V_{34}, voltages were then measured using the bottom pair of side channels and the junction's vertical terminals, respectively. Each voltage probe here corresponds to multiple LIs, each measuring a different frequency.

outputting a 37 Hz AC voltage, ν, applied between the top pair of side channel contacts, Fig. 4.8. Two resistors placed in series with the junction, a 10 MΩ ballast resistor and a 1 kΩ resistor, allowed the current through the circuit to be controlled and measured, respectively, by utilizing Ohm's law. The first and second harmonics of the laterally applied voltage, V_{12}, were measured using two LIs connected to the

bottom pair of side channel contacts. The first and second harmonics of the transverse voltage response of the junction, V_{34}, were measured using LIs connected to the junction's two vertical terminals.

4.3. Simulation methods

There are two primary computational methods used to simulate physical systems that are described by differential equations: the Finite Difference Method (FDM) and Finite Element Method (FEM). In short FDM approximates the differential equations, while FEM approximates the solution to the differential equation. For reasons given in the next section, the computational modeling in this dissertation uses the FEM method. The next section gives a brief overview of the FDM method. Following this is a slightly more extensive overview of the FEM method.

4.3.1. Finite difference method

The FDM method approximates the continuous differential equations governing a system as discretized equations. For example, for equally spaced points in space, the second derivative of a function can be approximated as

$$\frac{d^2 f}{dx^2} = \frac{f(x + \Delta x) - 2f(x) + f(x - \Delta x)}{\Delta x^2} \,. \tag{4.2}$$

Using similar expressions to approximate any other terms in a given differential equation leads to a set of equations for the various $f(x)$ values. Solving the set of equations yields the solution to the differential equation. The grid of points used to analyze the $f(x)$, known as a mesh, is typically rectilinear, Fig. 4.9.a, and has

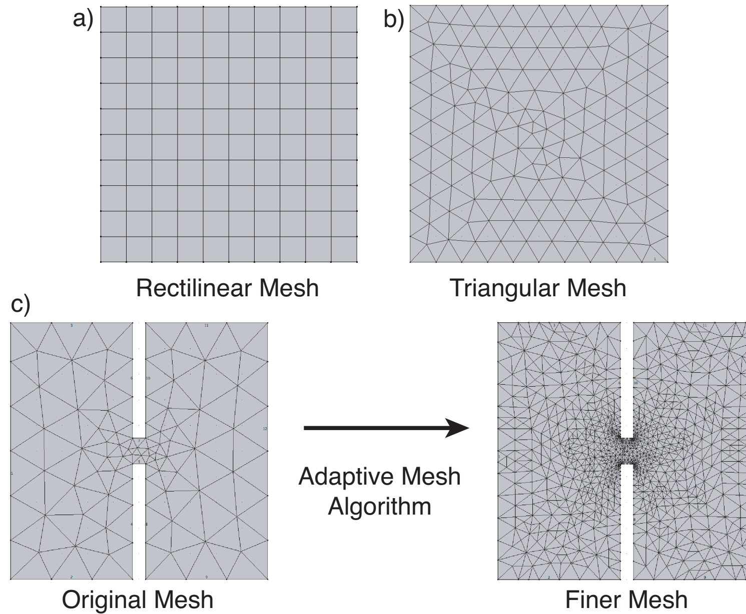

FIGURE 4.9. (a and b) Examples of rectangular and triangular two-dimensional meshes used in computational modeling. (c) Starting with a standard triangular mesh, the adaptive mesh algorithm refines the mesh where the simulation error is greatest. For the case shown here, the largest errors are located around the corners near the central connector. The algorithm increased the mesh resolution here more than in the side regions.

equal spacing between points, $\Delta x = \Delta y = \Delta z = const.$, to minimize computational errors.

The primary disadvantage of the FDM method occurs when complicated geometries are being simulated. Using FDM to model curved surfaces, for example, will always result in one of two undesired outcomes. The curved surface will always be approximated by cubes. Increasing the mesh resolution to compensate for the surface also increases the resolution in open areas where the finer resolution is not required, leading to increased memory usage and computation time. If a free mesh is used, one with varying distances to neighboring points, to accommodate the irregular surface, the discretized equations lose accuracy, computer coding is more complex,

and the computation time increases. It is for these reasons that the FDM method is not used in this dissertation.

4.3.2. Finite element method

The FEM method uses basis functions, $\phi_i(x, y, z)$, and coefficients to those functions, a_i, to approximate the solution to a given system of differential equations. The solution to the problem then takes the form

$$f(x, y, z) = \sum_i a_i \phi_i \,. \tag{4.3}$$

To solve for the solution vector $\vec{a}$, the differential equation is multiplied by the kth basis function, and integrated over the entire domain. For each value of k, a single algebraic equation is produced that only depends on the unknown elements of $\vec{a}$, resulting in an algebraic system of equations for the a_i's. Solving this set of equations yields the solution to the differential equation.

The most simple example of a basis function is a first degree polynomial between neighboring mesh points, or nodes, Fig. 4.10.a. Each basis function has unit value at its designated node and linearly decreases to zero toward its neighboring nodes. In a system with one independent coordinate, this amounts to simple lines between nodes.

The primary advantage of the FEM method is its ability to handle complex geometries. Nodes can be moved, removed, or added in with zero to minimal extra computation time and complexity, allowing any geometry to be modeled using the same computational techniques. In the past half century, powerful solving algorithms have been developed by researchers that intentionally change the mesh while solving

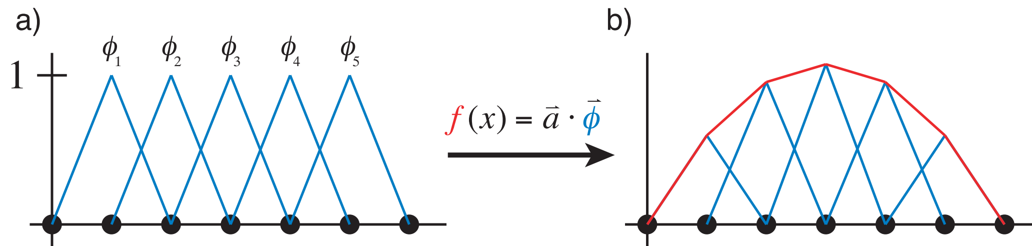

FIGURE 4.10. (a) A 1-dimensional set of linear basis functions. The nodes are depicted as the black circles on the x-axis. Though the nodes are shown equally spaced here, this is not a requirement for the FEM method. (b) Once the solution vector $\vec{a}$ has been found, the basis functions can be used to approximate the solution between the endpoints as a series of straight lines. The case shown here has its boundary conditions set to zero, but non-zero boundary conditions can be imposed by forcing the ends, a_1 and a_5 here, to specific values.

to minimize the computational error of a given simulation. These algorithms can automatically increase the mesh density where it's needed and reduce it where it's not, leading to accurate solutions without compromising the calculation time. An example output of the adaptive mesh algorithm is shown in Fig. 4.9.c.

4.3.3. Limitations to models of mesoscale systems

One concern to keep in mind when simulating mesoscale systems is the presence of ballistic or quantum phenomena. The use of the FEM method to simulate these systems is not in question. What must be considered is using the appropriate governing equations. One must always keep in mind the limitations of the models being used. For example, a diffusive heat model should not be used to describe the heat flow through a device with a size much smaller than the mean free path of the energy carriers.

4.4. Modeling using COMSOL Multiphysics

COMSOL Multiphysics is a commercial software package that uses FEM methods to simulate physical systems. The software is capable of combining any number of physical phenomena and applying them to any geometrical system. Many standard system-of-equations are available, called modules, such as Joule heating, heat transfer, electrostatics, and electrodynamics. Examples of other physical processes available are chemical reactions and stress analysis. The modules used in this dissertation are heat transfer and electric currents.

4.4.1. The heat transfer module

The heat transfer module in COMSOL, simulates thermal processes using the standard diffusive heat equation,

$$-\vec{\nabla} \cdot \left(\tilde{\kappa} \cdot \vec{\nabla} T \right) = Q, \tag{4.4}$$

where $\tilde{\kappa}$ is the thermal conductivity, T is the temperature, and Q represents any heat sources or sinks. The heat sources relevant to this dissertation are Joule heat,

$$Q_{\text{J.H.}} = \vec{J} \cdot \vec{E}\,, \tag{4.5}$$

electron-phonon coupling,

$$Q_{\text{e-p}} = \Gamma \left(T_e^n - T_p^n \right)\,, \tag{4.6}$$

and the thermoelectric volume heat sources – Peltier, Thomson, and Bridgman – Eq. (2.13). Here $\vec{J}$ and $\vec{E}$ are the total electric current density and electric field,

respectively, in the system, Γ and n are constants characterizing the coupling between electrons and phonons, and $T_{e,p}$ are the electron and phonon temperatures.

4.4.2. The electric currents module

The primary equation for the electric current module is that of charge conservation,

$$\vec{\nabla} \cdot \vec{J} = \vec{\nabla} \cdot \left(\tilde{\sigma} \vec{E} + \vec{J}_{ext.} \right) = 0, \tag{4.7}$$

where $\tilde{\sigma}$ is the electric conductivity, and $\vec{J}_{ext.}$ represents additional driving forces for electric current density, called the external current density here. The external current density that is of interest for this dissertation is the thermocurrent, see Eq. (2.4).

$$\vec{J}_{Th} = -\tilde{\sigma} \cdot \tilde{S} \cdot \vec{\nabla} T \tag{4.8}$$

4.4.3. Boundary conditions

With the governing equations and physical constants defined, the last step to any simulation is to define the boundary conditions (BC). COMSOL has multiple BCs available for the modules' numerous applications. For the simulations presented here, only six are of any concern.

There are two types of thermal BCs. The first thermal BC is the simple case of setting a boundary to specific temperature. The second BC is thermal insulation, which states that the normal heat flux through a given surface be zero,

$$\hat{n} \cdot \vec{\phi} = 0\,, \tag{4.9}$$

where $\hat{n}$ is the normal vector to the surface. In physical systems, the ideal of a thermally insulating boundary as defined here does not exist. Even in vacuum, there is radiative heat flux between the surface and the surroundings. Therefore, the thermal insulation BC is used on surfaces that are expected to have very low heat fluxes compared to the rest of the system.

There are three BCs for the electric currents module. The first is setting a surface to a specific electric potential. In COMSOL this is broken into two similar BCs: named 'electric potential' and 'ground.' The electric potential BC is used to set a surface to a specific voltage. The ground BC is simply a subset of the electric potential BC with a set voltage of zero.

The second electric BC is electrical insulation, which states that the electric current through a surface be zero,

$$\hat{n} \cdot \vec{J} = 0\,. \tag{4.10}$$

Unlike the thermal insulation BC, electric insulation occurs at any surface between conducting and non-conducting materials.

The last electric BC is that of setting an inward electric current density on a surface. In many experiments set currents are applied to materials instead of set voltages. This BC is used to apply such conditions. Positive current density for this BC is defined as a current entering the material, $J_{BC} > 0$, while negative current density, $J_{BC} < 0$, represents an exiting current. Note that in order to apply this type of BC, at least one surface must have an electric potential defined. This condition is due to the gauge invariance of the electric potential. With no voltage defined, the COMSOL solving algorithms for the electric potential will diverge, and return a 'no solution' message.

CHAPTER V

THERMOELECTRIC RESPONSE OF A FOUR-TERMINAL BALLISTIC RECTIFIER

The multi-terminal scattering theory derived in this chapter was co-developed by David Sánchez and I. At the time of this dissertation, David conducts research at the Instituto de Física Interdisciplinar y Sistemas Complejos in Mallorca, Spain. I performed all of the experiments, analyses, and writing.

5.1. Towards a mesoscopic transverse thermoelectric response

Recent studies on four-terminal ballistic junctions in a 2DEG, Fig. 5.1., have shown a transverse, non-linear voltage response when driven by a laterally applied voltage [21–24, 60, 61]. This response is due to the voltage-dependent transmission functions in the quantum-point-contact-like constrictions within the junction. The QPC-like behavior seen in those experiments suggests that such junctions may also be able to generate a transverse thermovoltage due to laterally applied thermal gradients.

Interest in transverse thermoelectric materials comes from their ability to directionally decouple the electric current from the thermal gradient, as well as other conflicting material properties such as the electronic thermal conductivity and electrical conductivity. Such an ability could allow greater control over the thermoelectric figure of merit [15]. The four-terminal ballistic junction represents one method to potentially accomplish this; however, such thermoelectric experiments had yet to be conducted until this dissertation.

In this chapter I will present experimental evidence that four-terminal ballistic junctions with a central scatterer do indeed generate transverse thermovoltages. I

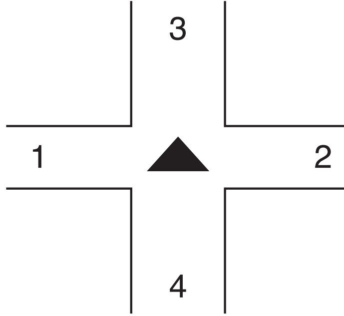

FIGURE 5.1. Basic geometry for the four-terminal ballistic rectifier. The central scatterer in drawn as the black triangle. The basic symmetry here, lateral but not vertical symmetry, is the standard configuration for such junctions. This numbering scheme for the terminals will be used throughout the chapter.

will also derive a quantitative model of the junction, based on the multi-terminal scattering approach [26], that will describe the linear thermoelectric response as well as the non-linear voltage response. This model will show that the transverse thermoelectric and non-linear electronic effects depend on the junction's energy-dependent transmission functions in the same way. I will first show Hall and SdH measurements that characterize the wafer material, followed by the specific junction studied here.

5.2. Wafer characterization

The carrier mobility and concentration for the chip measured on here were determined through Hall and Shubnikov de Haas measurements on an empty Hall bar. The measurement setup and results are shown in Fig. 5.2. Using Eqs. (3.17), (3.19), and (3.20), the carrier concentration and mobility were found to be $n = 2.93 \times 10^{12}$ cm^{-2} and 1.16×10^5 cm^2/Vs, respectively. Using these values and Eq. (3.4), the elastic mean free path is calculated to be $l_e = 3.3$ μm.

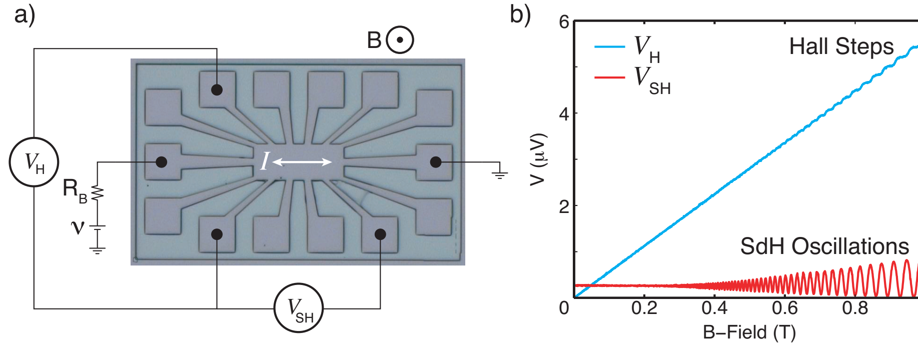

FIGURE 5.2. (a) Measurement setup for the Hall, V_H, and Shubnikov de Haas, V_{SH}, measurements. The current was symmetrically driven through the Hall bar, and was driven by a 37 Hz driving voltage, ν. A 100 MΩ ballast resistor, R_B, was used to control the current. The magnetic field was applied perpendicular to the plane of the Hall bar. (b) Measured Hall voltage and Shubnikov de Haas oscillations as a function of magnetic field. Landau levels can be seen starting at roughly 0.4 T.

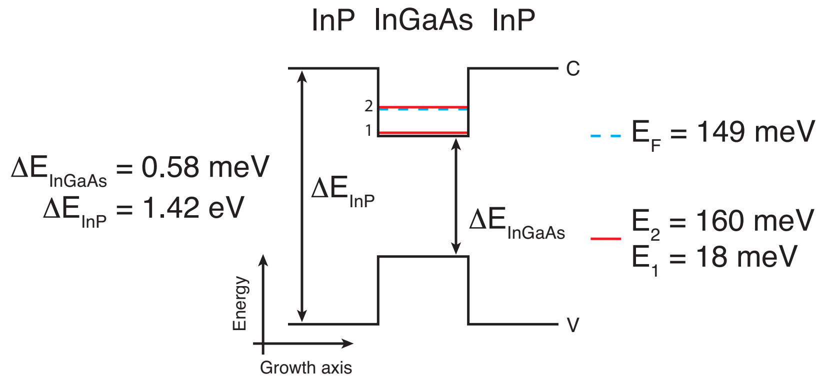

FIGURE 5.3. Energy diagram for the conduction, C, and valence, V, bands in the InGaAs/InP heterostructure wafer. Also shown are the two quantum-well bound states and the Fermi energy. For the device studied here, the InGaAs layer has a width of 9 nm. The two bound state energy levels of the quantum well were calculated using the finite quantum-well approximation with an effective mass of $0.047m_e$. Data used for the bound state calculation was compiled from Refs. [42–44], and personal correspondence with M. Larsson at Lund University.

The difference between carrier densities from the Hall and SdH measurements was less than 1%, signifying that system was truly 2D with only one occupied sub-band. This result can also be conceptually checked as well by comparing the Fermi energy with the bound states in the InGaAs quantum well, Fig. 5.3. Using Eq. (3.2) and an effective mass of $m^* = 0.047m_e$, the 2D Fermi energy is calculated to be 149 meV. At a background temperature of 0.75 K, the thermal energy in these experiments is about 0.1 meV, which is much less than the 11 meV of energy needed to reach the second bound state in the quantum well.

5.3. Experimental results

These experiments were motivated by the potential for a four-terminal ballistic scattering junction to create a transverse thermovoltage. The geometry of the four-terminal junction measured on in this chapter, called D1, is shown in Fig. 5.4.a, along with a Scanning Electron Micrograph (SEM) of a similar device. D1 was modeled after similar junctions seen in the literature [23, 60]. The results here are focused on proving that the junction does indeed generate a transverse thermovoltage, and that response cannot be attributed to any stray voltage effects. Before delving into the thermoelectric measurements, it is instructive to first cover the transverse electronic response due to a laterally applied voltage.

5.3.1. Transverse electric response to a laterally applied voltage

The quantity of interest for the laterally applied voltage measurements is the transverse voltage response, $V_{34}(V_1, V_2)$, where $V_{ij} = V_i - V_j$. See Fig. 4.8. for the measurement setup. Both the first and second harmonics of $V_{34}(V_1, V_2)$ are shown in Fig. 5.5. For these measurements, terminal 1 was grounded while the driving voltage

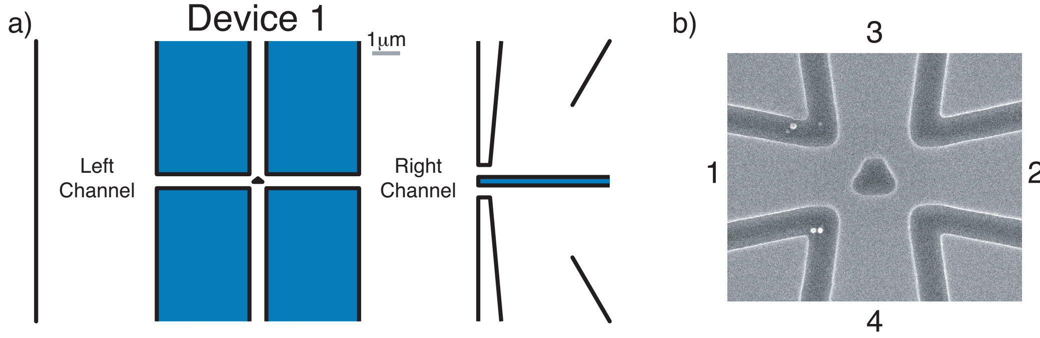

FIGURE 5.4. (a) Schematic of D1, and (b) SEM image of a similar device. At a background temperature of $\theta = 0.75$ K, the mean free path in D1 was $l_e = 3.3\mu$m, which puts the junction in a quasi-ballistic regime.

was applied to terminal 2. Also shown in Fig. 5.5. are low-voltage linear and quadratic fits to the first and second harmonics, respectively. These fits illustrate the linear and parabolic nature of the the two harmonics, and will be used later in analyzing the thermoelectric response.

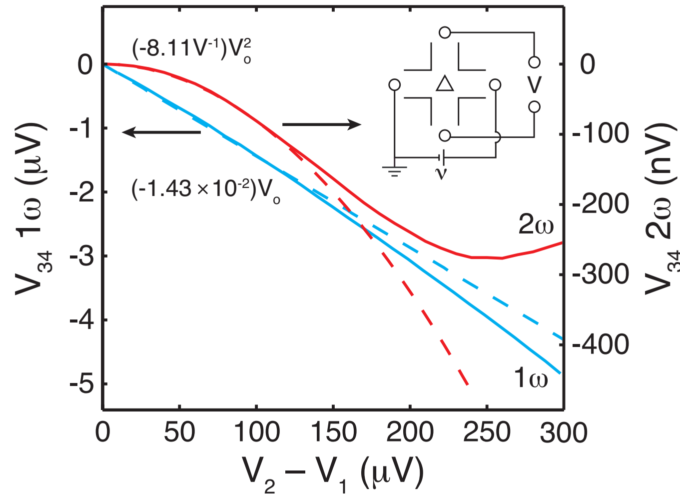

FIGURE 5.5. First and second harmonic of the transverse response to a laterally applied voltage, along with linear and quadratic fits, respectively. The data here is the average of 99 consecutive measurements. Here V_o is defined through $V_{21} = V_o \cos(\omega t)$.

The current understanding of how these devices work [21–24] states that the rectifying effects come from the voltage-dependent transmission functions between the four terminals, $t_{\alpha\beta}(\{V\})$. Since the conductance is dependent on the transmission function, the transverse response can also be described as a voltage-dependent conductance, $G(\{V\})$. In the two-terminal case for example, if the conductance is given by $G = G_o + G'_oV$, then $I = G(V)V = (G_o + G'_oV)V = G_oV + G'_oV^2$. If we qualitatively extended this to the four-terminal case, a similar four-terminal conductance could then easily describe a first harmonic response with a term linear in voltage, and a second harmonic response with a term quadratic in voltage (see Appendix D for details on harmonic generation). The quantitative details of such a multi-terminal theory will be derived later in this chapter.

5.3.2. Transverse electronic response to a laterally applied thermal gradient

In these measurements, the quantity of interest is the transverse thermovoltage as a function of the applied lateral temperatures, $V_{34}(\theta_1, \theta_2)$, where θ_α is the temperature increase in the αth terminal above the background temperature, θ. D1 was intended as a proof of principle experiment, so no direct temperature measurements were made. As such, all measurements here will be given as a function of the AC heating voltage, $V_H = V_h \cos(\omega t)$.

The first four harmonics of $V_{34}(\theta_1 = 0, \theta_2(V_h))$ are shown in Fig. 5.6. Recall from Ch. IV that thermovoltages that are linear in temperature are proportional to the second harmonic of the heating voltage, $V_{th} \propto \Delta T \propto V_H^2 \propto \cos(2\omega t)$. The dominant 2ω response then, is indicative of a linear response to the applied temperature.

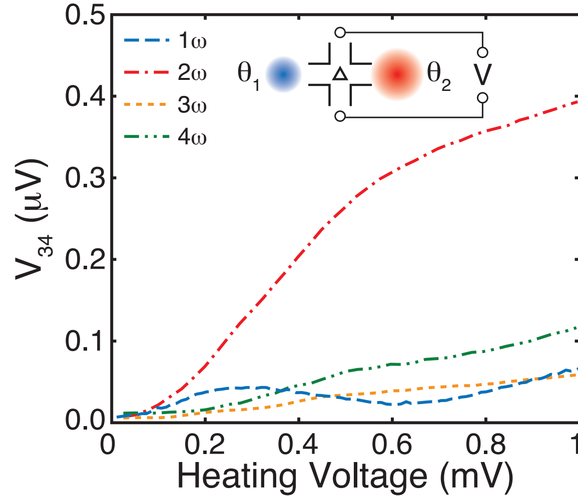

FIGURE 5.6. First four harmonics of the transverse thermovoltage while heating terminal 2. The dominant 2ω response is an indication that the response is linear in the applied temperature, $V_{th} \propto \Delta T \propto V_H^2 \propto \cos(2\omega t)$.

The response to individually heating terminals 1 and 2 are shown in Fig. 5.7. Based on the geometric symmetry of the junction, we would naively expect a lateral mirror symmetry in the transverse response to a thermal gradient, $V_{34}(\theta_1, \theta_2) \approx V_{34}(\theta_2, \theta_1)$. Contrary to this, the junction exhibits a sign reversal upon reversing the lateral thermal gradient, $V_{34}(\theta_1, \theta_2) \approx -V_{34}(\theta_2, \theta_1)$. Similar effects have been seen in the literature for applied voltages [20–24]. In those measurements, sign reversals in V_{34} have been seen to depend on the conditions while cooling down to liquid helium temperatures, the amplitude of the applied voltage, or the gate voltages. In each case these reversals have been attributed to an energy-dependent transmission function in the QPC-like constrictions within the junction.

After considering the electronic rectifying effects of the junction in Fig. 5.5., one may question if the observed response in Fig. 5.7. is not a thermal response, but an electric response due to stray lateral voltages from the applied heating voltages. Such voltages could easily occur if the two out-of-phase heating voltages weren't balanced

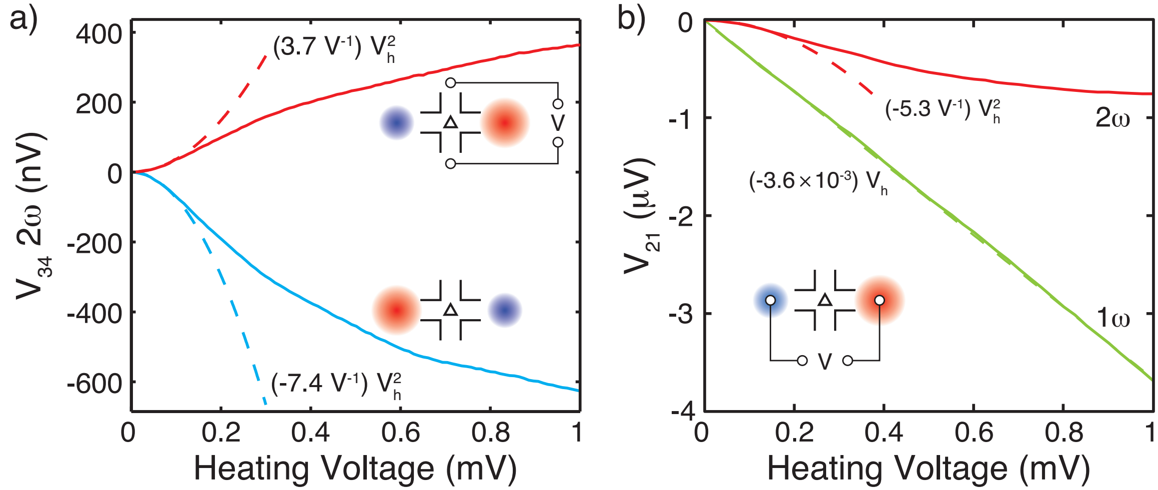

FIGURE 5.7. (a) Transverse response due to a lateral thermal gradient for separately heating terminals 1 and 2. (b) First and second harmonics of the lateral voltage drop while terminal 2 was heated. In both plots, linear and parabolic fits to the first and second harmonics, respectively, are shown at low heating voltages. Also shown are parabolic fits at low heating voltages.

properly (see Chapter IV). The short answer to this is no; the response is thermal in nature. To see this, we must consider the first and second harmonic of the lateral voltage drop across the junction, Fig. 5.7.b. Using the measurements in Fig. 5.5. as a reference, we can then predict what percentage of the thermal response is in fact due to electronic effects.

There are two mechanisms from the applied voltage experiments that we must consider: the linear response, which gives a straight one-to-one frequency conversion between the applied lateral voltage and the transverse voltage, $V_{34}^{(1\omega)} = f(V_1, V_2)^{(1\omega)}$; and the quadratic response, which gives a frequency-doubling conversion, $V_{34}^{(2\omega)} = f(V_1, V_2)^{(2\omega)}$. These functions, $f^{(1\omega)}$ and $f^{(2\omega)}$, can be taken from the linear and quadratic fits, respectively, in Fig. 5.5.: $f^{(1\omega)} = V_{34}^{(1\omega)} = (-1.43 \times 10^{-2})V_{21}$, and $f^{(2\omega)} = V_{34}^{(2\omega)} = (-8.11 \text{ V}^{-1})V_{21}^2$. Using these relations, I can estimate the electronic

TABLE 5.1. Estimated contributions to the transverse electronic response due to lateral voltages while terminal 2 was heated. The lateral voltages, $V_{21}(1\omega)$ and $V_{21}(2\omega)$, are calculated from the linear and quadratic fits in Fig. 5.7.b. The conversions to the transverse harmonics are calculated from the linear and quadratic fits in Fig. 5.5. Voltages are evaluated at a heating voltage of 0.1 mV: $V_{34}(1\omega) = 14$ nV and $V_{34}(2\omega) = 37$ nV.

Lateral Voltages	Contribution to V_{34} (1ω)	Contribution to V_{34} (2ω)
V_{21} (1ω) = 360 nV	5 nV (37%)	1 pV (0.01%)
V_{21} (2ω) = 53 nV	-	0.8 nV (2%)

contributions to the first and second harmonic responses in Fig. 5.6. These estimates are shown in Table 5.1.

As can be seen from the estimated voltages in Table 5.1., the net 1ω and 2ω electronic contributions to the thermoelectric response are 5 nV and 0.8 nV, respectively. This amounts to about 2 % of the total 2ω response, which leads me to conclude that the transverse response is due to the increased temperature in terminal 2. Understanding the origin of this transverse thermoelectric response is the motivation behind the scattering theory derived in the next section.

5.4. Multi-terminal scattering theory for a non-linear ballistic junction

The focus of this section is to derive a quantitative theory for a multi-terminal ballistic junction that is capable of describing both the non-linear voltage response, as well as the linear thermal response. To accomplish this I will combine two theoretical foundations that have already been laid out in the literature.

The foundation to form a quantitative theory explaining the non-linear voltage response has been laid out by Christen and Büttiker [25]. Additionally, the linear response in voltage and temperature for a multi-terminal junction has also previously

been derived by Butcher [26, 47]. By combining these two theories, I will show that the linear thermoelectric response and non-linear voltage response both depend on the same quantity, namely the derivative of the transmission function with respect to energy, $\partial t/\partial E$. In the end, the theory I derive here will allow the dependence of the thermal response on the transmission function to be obtained through non-linear voltage measurements.

5.4.1. Derivation of the current through the ballistic junction

I now derive the current through a multi-terminal junction using a thermoelectric scattering approach [26, 47] extended in the applied voltage to the weakly non-linear regime [25]. Starting with the multi-terminal scattering approach, the current through the αth terminal is given by,

$$I_\alpha = \frac{2e}{h} \sum_\beta \int_0^\infty dE \left(f\left(E - \mu_\alpha, T_\alpha\right) - f\left(E - \mu_\beta, T_\beta\right)\right) t_{\alpha\beta}\left(E, \{V_\gamma\}\right), \tag{5.1}$$

where e is the electron charge, h is Plank's constant, $f(E - \mu, T)$ is the Fermi-Dirac distribution, $t_{\alpha\beta}(E, \{V_\gamma\})$ is the transmission function between the αth and β^{th} terminals, and γ varies over all of the terminals. The Fermi-Dirac distribution describes the probability, f, of a fermionic state with energy E being occupied in thermal equilibrium at temperature T:

$$f(E - \mu, T) = \left(1 + \exp\left(\chi\right)\right)^{-1}, \tag{5.2}$$

where k_{B} is Boltzmann's constant, μ is the electrochemical potential, and $\chi \equiv (E - \mu)/k_B T$.

For this derivation, I will assume that $t_{\alpha\beta}(E, \{V_\gamma\})$ and its derivatives vary slowly on scales compared to eV_γ and $k_B T_\gamma$. This allows $f(E-\mu, T)$ and $t_{\alpha\beta}(E, \{V_\gamma\})$ to be expanded about the common electrochemical potential μ, and common temperature θ. The deviations from the common values for each terminal are given by V_α and θ_α.

$$eV_\alpha = \mu_\alpha - \mu \tag{5.3}$$

$$\theta_\alpha = T_\alpha - \theta \tag{5.4}$$

Based on the measurements discussed in previous sections, I_α should be expanded to quadratic order in V_α and linear order in θ_α. An important point to note at this stage is that in the final analysis, the non-linear voltage terms will not be used simultaneously with the linear temperature terms. This allows me to ignore cross terms of the form $V_\alpha \theta_\beta$ for this derivation.

Using a Taylor expansion, the Fermi function can be approximated as

$$f(E-\mu_\alpha, T_\alpha) \approx f(E-\mu, \theta) + \left.\frac{\partial f(E)}{\partial \mu_\alpha}\right|_{\mu,\theta} eV_\alpha + \frac{1}{2} \left.\frac{\partial^2 f(E)}{\partial \mu_\alpha^2}\right|_{\mu,\theta} e^2 V_\alpha^2 + \left.\frac{\partial f(E)}{\partial T_\alpha}\right|_{\mu,\theta} \theta_\alpha\,, \tag{5.5}$$

where the derivatives are calculated from Eq. (5.2).

$$\begin{aligned}
\left.\frac{\partial f(E-\mu_\alpha, T_\alpha)}{\partial \mu_\alpha}\right|_{\mu,\theta} &= \left[\frac{\partial}{\partial \mu_\alpha} \left(1+\exp\left(\chi_\alpha\right)\right)^{-1}\right]_{\mu,\theta} \\
&= \left[\left(1+\exp\left(\chi_\alpha\right)\right)^{-2} \exp\left(\chi_\alpha\right) \frac{1}{k_B T_\alpha}\right]_{\mu,\theta} \\
&= \left(f(E-\mu,\theta)\right)^2 \exp\left(\chi_\mu\right) \frac{1}{k_B \theta}
\end{aligned} \tag{5.6}$$

$$\left.\frac{\partial^2 f(E-\mu_\alpha,T_\alpha)}{\partial\mu_\alpha^2}\right|_{\mu,\theta} = \left[\frac{\partial}{\partial\mu_\alpha}\left(\frac{\partial f}{\partial\mu_\alpha}\right)\right]_{\mu,\theta}$$
$$= \left[\frac{\partial}{\partial\mu_\alpha}\left((f(E-\mu,\theta))^2\exp\left(\chi_\mu\right)\frac{1}{k_B\theta}\right)\right]_{\mu,\theta}$$
$$= \left[\left(2f\exp\left(\chi_\alpha\right)-1\right)\frac{\partial f}{\partial\mu_\alpha}\frac{1}{k_\mathrm{B}T_\alpha}\right]_{\mu,\theta}$$
$$= \left(2f\exp\left(\chi_\mu\right)-1\right)\left.\frac{\partial f}{\partial\mu_\alpha}\right|_{\mu,\theta}\frac{1}{k_\mathrm{B}\theta_\alpha} \tag{5.7}$$

$$\left.\frac{\partial f(E-\mu_\alpha,T_\alpha)}{\partial T_\alpha}\right|_{\mu,\theta} = \left[\frac{\partial}{\partial T_\alpha}\left(1+\exp\left(\chi_\alpha\right)\right)^{-1}\right]_{\mu,\theta}$$
$$= \left[\left(1+\exp\left(\chi_\alpha\right)\right)^{-2}\exp\left(\chi_\alpha\right)\chi_\alpha\frac{1}{T_\alpha}\right]_{\mu,\theta}$$
$$= \left(f(E-\mu,\theta)\right)^2\exp\left(\chi_\mu\right)\chi_\mu\frac{1}{\theta}$$
$$= \left.\frac{\partial f}{\partial\mu}\right|_{\mu,\theta}\frac{E-\mu}{\theta} \tag{5.8}$$

The transmission function is also Taylor expanded about μ, though only to linear order in the energy and terminal voltages.

$$t_{\alpha\beta}(E,\{V_\gamma\}) = t_{\alpha\beta}(\mu) + \left.\frac{\partial t_{\alpha\beta}}{\partial E}\right|_\mu (E-\mu) + \sum_\gamma \left.\frac{\partial t_{\alpha\beta}}{\partial V_\gamma}\right|_\mu V_\gamma \tag{5.9}$$

Inserting Eqs. (5.5) and (5.9) into Eq. (5.1), and only keeping terms up to quadratic order in V_α, gives the approximated current.

$$\begin{aligned} I_\alpha = \frac{2e}{h} \sum_\beta \int_0^\infty dE \Bigg[& \left.\frac{\partial f}{\partial \mu}\right|_{\mu,\theta} e(V_\alpha - V_\beta) t_{\alpha\beta}(\mu) + \left.\frac{\partial f}{\partial \mu}\right|_{\mu,\theta} e(V_\alpha - V_\beta) \sum_\gamma \left.\frac{\partial t_{\alpha\beta}}{\partial V_\gamma}\right|_{\mu} V_\gamma \\ & + \frac{1}{2} \left.\frac{\partial^2 f}{\partial \mu^2}\right|_{\mu,\theta} e^2 (V_\alpha^2 - V_\beta^2) t_{\alpha\beta}(\mu) \\ & + \frac{1}{2} \left.\frac{\partial^2 f}{\partial \mu^2}\right|_{\mu,\theta} (E-\mu) e^2 (V_\alpha^2 - V_\beta^2) \left.\frac{\partial t_{\alpha\beta}}{\partial E}\right|_{\mu} \\ & + \left.\frac{\partial f}{\partial \mu}\right|_{\mu,\theta} \frac{E-\mu}{\theta} (\theta_\alpha - \theta_\beta) t_{\alpha\beta}(\mu) \\ & + \left.\frac{\partial f}{\partial \mu}\right|_{\mu,\theta} \frac{(E-\mu)^2}{\theta} (\theta_\alpha - \theta_\beta) \left.\frac{\partial t_{\alpha\beta}}{\partial E}\right|_{\mu} \Bigg] \end{aligned} \tag{5.10}$$

The integrals in this equation can be immediately evaluated,

$$\begin{aligned} &\textstyle\int_0^\infty dE \left.\frac{\partial f}{\partial \mu}\right|_{\mu,\theta} = 1 \qquad && \textstyle\int_0^\infty dE \left.\frac{\partial f}{\partial \mu}\right|_{\mu,\theta} (E-\mu) = 0 \\ &\textstyle\int_0^\infty dE \left.\frac{\partial^2 f}{\partial \mu^2}\right|_{\mu,\theta} = 0 \qquad && \textstyle\int_0^\infty dE \left.\frac{\partial^2 f}{\partial \mu^2}\right|_{\mu,\theta} (E-\mu) = 1 \\ &\int_0^\infty dE \left.\frac{\partial^2 f}{\partial \mu^2}\right|_{\mu,\theta} (E-\mu) = \frac{\pi^2 k_{\mathrm{B}}^2}{3}, && \end{aligned}$$

which simplifies I_α to

$$I_\alpha = I_\alpha^{(1)} + I_\alpha^{(2)}, \tag{5.11}$$

where

$$I_\alpha^{(1)} = \sum_\beta \left[\frac{2e^2}{h} (V_\alpha - V_\beta) t_{\alpha\beta}(\mu) + \frac{2\pi^2 e k_{\mathrm{B}}^2 \theta}{3h} (\theta_\alpha - \theta_\beta) \left.\frac{\partial t_{\alpha\beta}}{\partial E}\right|_{\mu} \right], \tag{5.12}$$

and

$$I_\alpha^{(2)} = \frac{e^2}{h} \sum_\beta \left[2(V_\alpha - V_\beta) \sum_\gamma \left. \frac{\partial t_{\alpha\beta}}{\partial V_\gamma} \right|_\mu V_\gamma + e(V_\alpha^2 - V_\beta^2) \left. \frac{\partial t_{\alpha\beta}}{\partial E} \right|_\mu \right] . \tag{5.13}$$

It has recently been pointed out by Büttiker et. al [62] that any mesoscopic theory involving voltages must be invariant under a global shift in voltage, $V_\alpha \to V_\alpha + V$. This is known as gauge invariance. At first glance, Eq. (5.13) does not appear to be gauge invariant; however it can be made so by requiring $t_{\alpha\beta}$ to have certain symmetries. Under a constant voltage shift, $I_\alpha^{(2)}$ becomes,

$$\begin{aligned} I_{\alpha,\text{Shift}}^{(2)} = \frac{e^2}{h} \sum_\beta \Bigg[& 2(V_\alpha - V_\beta) \sum_\gamma \left. \frac{\partial t_{\alpha\beta}}{\partial V_\gamma} \right|_\mu (V_\gamma + V) \\ & + e(V_\alpha^2 + 2V_\alpha V - V_\beta^2 - 2V_\beta V) \left. \frac{\partial t_{\alpha\beta}}{\partial E} \right|_\mu \Bigg] . \end{aligned} \tag{5.14}$$

Requiring $I_\alpha^{(2)} = I_{\alpha,\text{Shift}}^{(2)}$ leads to the following symmetry conditions for $t_{\alpha\beta}$:

$$\sum_\gamma \left. \frac{\partial t_{\alpha\beta}}{\partial V_\gamma} \right|_\mu + e \left. \frac{\partial t_{\alpha\beta}}{\partial E} \right|_\mu = 0 \,, \tag{5.15}$$

which are known as the non-linear gauge symmetries for a multi-terminal junction [25].

To force Eq. (5.13) to be gauge invariant, I use Eq. (5.15) to eliminate the $\partial t_{\alpha\beta}/\partial V_\alpha$ term in the summation over γ. Rewriting Eq. (5.15) as

$$\left. \frac{\partial t_{\alpha\beta}}{\partial V_\alpha} \right|_\mu = - \sum_{\gamma \neq \alpha} \left. \frac{\partial t_{\alpha\beta}}{\partial V_\gamma} \right|_\mu - e \left. \frac{\partial t_{\alpha\beta}}{\partial E} \right|_\mu \,, \tag{5.16}$$

and inserting this into Eq. (5.13) gives,

$$
\begin{aligned}
I_\alpha^{(2)} &= \frac{e^2}{h}\sum_\beta \left[2(V_\alpha - V_\beta)\left(\left.\frac{\partial t_{\alpha\beta}}{\partial V_\alpha}\right|_\mu V_\alpha + \sum_{\gamma\neq\alpha} \left.\frac{\partial t_{\alpha\beta}}{\partial V_\gamma}\right|_\mu V_\gamma \right) + e(V_\alpha^2 - V_\beta^2) \left.\frac{\partial t_{\alpha\beta}}{\partial E}\right|_\mu \right] \\
&= \tfrac{e^2}{h}\textstyle\sum_\beta \Big[-2(V_\alpha - V_\beta)\Big(e \left.\tfrac{\partial t_{\alpha\beta}}{\partial E}\right|_\mu V_\alpha + \textstyle\sum_{\gamma\neq\alpha} \left.\tfrac{\partial t_{\alpha\beta}}{\partial V_\gamma}\right|_\mu (V_\alpha - V_\gamma) \Big) \\
&\qquad\qquad + e(V_\alpha^2 - V_\beta^2) \left.\tfrac{\partial t_{\alpha\beta}}{\partial E}\right|_\mu \Big] \\
&= \frac{e^2}{h}\sum_\beta \left[(-V_\alpha^2 - V_\beta^2 + 2V_\alpha V_\beta) e \left.\frac{\partial t_{\alpha\beta}}{\partial E}\right|_\mu - 2(V_\alpha - V_\beta)\sum_{\gamma\neq\alpha} \left.\frac{\partial t_{\alpha\beta}}{\partial V_\gamma}\right|_\mu (V_\alpha - V_\gamma) \right] \\
&= \frac{e^2}{h}\sum_\beta \left[-(V_\alpha - V_\beta)^2 e \left.\frac{\partial t_{\alpha\beta}}{\partial E}\right|_\mu - 2(V_\alpha - V_\beta)\sum_{\gamma} \left.\frac{\partial t_{\alpha\beta}}{\partial V_\gamma}\right|_\mu (V_\alpha - V_\gamma) \right]. \qquad (5.17)
\end{aligned}
$$

In the last line I dropped the $\gamma \neq \alpha$ restriction in the summation since the $\gamma = \alpha$ term goes to zero. The gauge invariance is now clearly apparent, since all voltage terms appear in the form of $V_\alpha - V_\beta$. Writing out I_α in full gives the final theoretical result for this section:

$$
\begin{aligned}
I_\alpha = \sum_\beta \Big[& G_{\alpha\beta}(V_\alpha - V_\beta) + \sum_\gamma (V_\alpha - V_\beta) G_{\alpha\beta\gamma}(V_\alpha - V_\gamma) \\
& + M_{\alpha\beta}(V_\alpha - V_\beta)^2 + L_{\alpha\beta}(\theta_\alpha - \theta_\beta) \Big] \qquad (5.18)
\end{aligned}
$$

where I have defined

$$G_{\alpha\beta} = \frac{2e^2}{h} \left. t_{\alpha\beta}\right|_\mu \qquad (5.19)$$

$$G_{\alpha\beta\gamma} = -\frac{2e^2}{h} \left.\frac{\partial t_{\alpha\beta}}{\partial V_\gamma}\right|_\mu \qquad (5.20)$$

$$M_{\alpha\beta} = -\frac{e^3}{h} \left.\frac{\partial t_{\alpha\beta}}{\partial E}\right|_\mu \qquad (5.21)$$

$$L_{\alpha\beta} = \frac{2\pi^2 e k_{\mathrm{B}}^2 \theta}{3h} \left.\frac{\partial t_{\alpha\beta}}{\partial E}\right|_\mu . \qquad (5.22)$$

$G_{\alpha\beta}$ and $L_{\alpha\beta}$ are the previously derived linear response terms [26]. $G_{\alpha\beta\gamma}$ and $M_{\alpha\beta}$ are the two new terms derived here, and represent the non-linear electronic response of the junction.

I must once again note that although Eq. (5.18) will be very useful in analyzing the four-terminal junction response, ultimately it is incomplete. A proper derivation should include cross terms between the applied voltages and temperatures $V_\alpha\theta_\beta$. This is of little concern here though, since the non-linear voltage terms will never be used simultaneously with the thermal term.

As stated at the outset, I have now shown that the non-linear voltage dependence, Eq. (5.21), and linear temperature dependence, Eq. (5.22), of the current through the junction are dependent on the transmission function in the same way, namely $\partial t_{\alpha\beta}/\partial E$. There is one catch; in order make use of this information, the effects of the two non-linear voltage terms must be separated. This will be addressed in the next section.

In the next section I will use Eq. (5.18) to show that the linear temperature and non-linear voltage terms in the transverse voltage response depend on the transmission function in the same way, $V_{34} \propto F(t_{\alpha\beta}, t'_{\alpha\beta})(aV_\alpha + b\theta_\alpha)$. When applied to the four-terminal junction, this will allow me to use the non-linear voltage measurements in Fig. 5.5. to extract the transverse thermopower from the measurements in Fig. 5.7.

5.5. Multi-terminal scattering theory applied to the four-terminal junction

With the model in hand, the next step is to apply it to the four-terminal junction measurements. The main goal here is to solve for $V_{34}(V_1, V_2, \theta_1, \theta_2)$ and find the coefficient that describes both the non-linear voltage and linear temperature terms.

5.5.1. Solving for the transverse response

As derived, Eqs. (5.18) - (5.22) are general in that any number of terminals can be handled. Including the top gate, which will become important for simplification purposes, our junction has five terminals: $\{V_1, V_2, V_3, V_4, V_g\}$. In order to solve for the transverse response, $V_{34} = V_3 - V_4$, I first assume that no current enters or exits the top gate, $t_{\alpha g} = t_{g\beta} = 0$. I also assume that the transmission functions are independent of the terminal voltages, $\partial t_{\alpha\beta}/\partial V_i = 0$, for $i = 1, 2, 3, 4$. From gauge symmetry, Eq. (5.15), this implies

$$\left.\frac{\partial t_{\alpha\beta}}{\partial V_g}\right|_{\mu} = -e \left.\frac{\partial t_{\alpha\beta}}{\partial E}\right|_{\mu} , \tag{5.23}$$

which allows me to write Eq. (5.18) as

$$\begin{aligned} I_\alpha = \sum_{\beta=1}^{4} \big[& G_{\alpha\beta}(V_\alpha - V_\beta) + (V_\alpha - V_\beta) G_{\alpha\beta g} (V_\alpha - V_g) \\ & + M_{\alpha\beta}(V_\alpha - V_\beta)^2 + L_{\alpha\beta}(\theta_\alpha - \theta_\beta) \big] . \end{aligned} \tag{5.24}$$

For the junctions studied in this dissertation, I know $V_g/V_i \sim 10^3$, which allows one further simplification, $V_i - V_g \approx -V_g$:

$$\begin{aligned} I_\alpha &= \sum_{\beta=1}^{4} \left[\left(G_{\alpha\beta} - G_{\alpha\beta g} V_g\right)(V_\alpha - V_\beta) + M_{\alpha\beta}(V_\alpha - V_\beta)^2 + L_{\alpha\beta}(\theta_\alpha - \theta_\beta) \right] \\ &= \sum_{\beta=1}^{4} \left[\mathcal{G}_{\alpha\beta}(V_\alpha - V_\beta) + M_{\alpha\beta}(V_\alpha - V_\beta)^2 + L_{\alpha\beta}(\theta_\alpha - \theta_\beta) \right] , \end{aligned} \tag{5.25}$$

where I have defined

$$\begin{aligned}\mathcal{G}_{\alpha\beta} &\equiv G_{\alpha\beta} - G_{\alpha\beta g}V_g \\ &\equiv \frac{2e^2}{h}\, t_{\alpha\beta}\big|_{\mu} - \frac{2e^3}{h}\,\frac{\partial t_{\alpha\beta}}{\partial E}\bigg|_{\mu} V_g \\ &\equiv \frac{2e^2}{h}\mathcal{T}_{\alpha\beta}\,. \end{aligned} \tag{5.26}$$

As written, solving the four equations described by Eq. (5.25) for V_{34} is mathematically intractable. To solve for V_{34} then, I first assume that the vertical terminals act as ideal voltage probes, $I_3 = I_4 = 0$. For the junction's response to temperatures, I assume that the vertical terminals remain cold, $\theta_3 = \theta_4 = 0$. Lastly, for the non-linear voltage terms, I assume that terms of the form $V_{1,2,3,4}V_{3,4}$ can be neglected. This assumption is solely based on the observation that $V_{12} > V_{34}$ during the applied voltage measurements, though this does not guarantee the said assumption since the relative voltage between the lateral and vertical terminals is missing. I will revisit this in the discussion. To solve for V_{34}, I only need to write out the equations for I_3 and I_4. With the stated assumptions, these two equations read

$$\begin{aligned} I_3 = 0 = &\,\mathcal{G}_{31}(V_3 - V_1) + \mathcal{G}_{32}(V_3 - V_2) + \mathcal{G}_{34}(V_3 - V_4) \\ &+ M_{31}V_1^2 + M_{32}V_2^2 - L_{31}\theta_1 - L_{32}\theta_2 \end{aligned} \tag{5.27}$$

$$\begin{aligned} I_4 = 0 = &\,\mathcal{G}_{41}(V_4 - V_1) + \mathcal{G}_{42}(V_4 - V_2) + \mathcal{G}_{43}(V_4 - V_3) \\ &+ M_{41}V_1^2 + M_{42}V_2^2 - L_{41}\theta_1 - L_{42}\theta_2\,. \end{aligned} \tag{5.28}$$

The problem has now been reduced to a simple gaussian elimination problem. Solving for V_{34} and simplifying terms yields,

$$V_{34} = A(V_1 - V_2) + \sum_{j=1,2} B_j(g_\theta \theta_j - g_e V_j^2)\,, \tag{5.29}$$

where,

$$A = \frac{\mathcal{T}_{31}\mathcal{T}_{42} - \mathcal{T}_{41}\mathcal{T}_{32}}{D}\,, \tag{5.30}$$

$$B_j = \frac{(\mathcal{T}_{41} + \mathcal{T}_{42})t'_{3j} - (\mathcal{T}_{31} + \mathcal{T}_{32})t'_{4j}}{D}\,, \tag{5.31}$$

$$D = (\mathcal{T}_{31} + \mathcal{T}_{32})(\mathcal{T}_{41} + \mathcal{T}_{42}) + \mathcal{T}_{34}(\mathcal{T}_{41} + \mathcal{T}_{42}) + \mathcal{T}_{43}(\mathcal{T}_{31} + \mathcal{T}_{32})\,, \tag{5.32}$$

and $g_e = e/2$ and $g_\theta = \pi^2 k_B^2 \theta/3e$. Eq. (5.29) is the final theory result of this section. As intended, it shows how the non-linear voltage term and linear temperature term share the same dependence on the transmission function, namely $B_{(1,2)}$. It must be stated once more that in Eq. (5.29), the temperature and non-linear voltage terms can be used individually, but not simultaneously.

Based on the observed sign difference in the applied temperature measurements, Fig. 5.7., Eq. (5.29) is very promising. Depending on the values of B_1 and B_2, the thermal response can be made either positive or negative. The observed symmetry for the junction studied here then implies $B_2 \approx -2B_1$, though this will most likely change if the top gate voltage changes. It is interesting to note that if the intended geometric symmetry of the junction, $t_{i1} = t_{j2}$ for $i = 3, 4$, is applied, Eq. (5.31) gives $B_j = 0$. In the same manner, Eq. (5.29) shows that the non-linear voltage response can be positive, negative or zero, depending on the relative transmission functions. This is exactly what has been seen previously [20, 21, 24].

In the next section, I will extract $\theta_2(V_h)$ and the thermopower of the junction by applying Eq. (5.29) to the experimental data in Figs. 5.5. and 5.7.

5.5.2. Extracting the temperature and thermopower

To extract the temperature and transverse thermopower, I must first determine B_2 through the applied voltage measurements. Knowing B_2 will then allow me to calculate the increase in temperature, and thus the transverse thermopower, in terminal 2 through the applied temperature measurements. It is important to again note that AC voltages were used in all measurements. As such, oscillatory functions must be used to evaluate Eq. (5.29).

The first task then is to determine B_2. The procedure here is to equate the $j = 2$ quadratic term from Eq. (5.29) with the quadratic fit in Fig. 5.5., $V_{34}(2\omega) = (-8.11\ \mathrm{V}^{-1})V_{21}^2$. Taking $V_1 = 0$, $V_2 = V_o \cos(\omega t)$, and only keeping the 2ω terms gives,

$$\begin{aligned}(-8.11V^{-1})V_o^2\cos(2\omega t) &= -g_e B_2\, V_2^2\big|_{(2\omega)} \\ (-8.11V^{-1})V_o^2\cos(2\omega t) &= -\frac{g_e B_2}{2}V_o^2\cos(2\omega t) \\ B_2 &= 2.03\times 10^{20}\ \mathrm{J}^{-1}\,. \end{aligned} \tag{5.33}$$

Since direct temperature measurements were not made, I assume $\theta_2 = aV_H^2$, where $V_H = V_h\cos(\omega t)$, and a is a constant. I calculate the parameter a by equating the $j = 2$ temperature term in Eq. (5.29) with the quadratic fit in Fig. 5.7., $V_{34}^{(2\omega)} =$

$(3.7 \text{ V}^{-1})V_h^2$.

$$
\begin{aligned}
(3.7V^{-1})V_h^2\cos(2\omega t) &= g_\theta B_2 \theta_2 \\
(3.7V^{-1})V_h^2\cos(2\omega t) &= g_\theta B_2 a\, V_H^2\big|_{(2\omega)} \\
(3.7V^{-1})V_h^2\cos(2\omega t) &= \frac{g_\theta B_2 a}{2} V_h^2\cos(2\omega t) \\
a &= 1.2\times 10^7 \text{ KV}^{-2}
\end{aligned}
\tag{5.34}
$$

The parabolic fit to the temperature response breaks down around $V_h \approx 0.1$ mV, at which point $V_{34}(2\omega) \approx 37$ nV. Therefore, at the limit of the quadratic fit, the temperature had increased by $\theta_2 = 63$ mK, which gives a transverse thermopower of $S_{34,12} = V_{34}/\theta_2 = 590$ nV/K.

To make sense of the magnitude of this thermopower, we can conceptually simplify the four constrictions to two—one top and one bottom—and consider what the difference in thermopower would be if those two constrictions were ideal quantum point contacts (QPC). To start, the thermopower of a QPC at the thermopower peak below the Nth occupied mode is,

$$
S_{QPC}(N) = \frac{k_B \ln(2)}{e}\frac{1}{N-0.5}\,. \tag{5.35}
$$

Assuming that the number of modes in our two QPCs only differs by one, I find that two quantum point contacts with mode numbers of 10 and 11 yields a difference in thermopower of 600 nV/K. Based on the lateral resistance measurements of the junction, $R_{12} \approx 1.1$ kΩ, these mode numbers are not unreasonable. Interpreting the junction as a network of QPCs interpretation works well to describe the laterally applied temperature measurements.

5.5.3. Revisiting the omitted voltages

In deriving Eq. (5.29) I assumed that the terms of the form $V_{1,2,3,4}V_{3,4}$ could be neglected. Upon analyzing the measurements in Figs. 5.5.-5.7., this seems to have been a reasonable assumption, but not conclusive. In order to verify its validity, additional measurements must be made that can compare the individual terminal voltages. At the writing of this dissertation, such measurements have been made and conclusively show that the four terminal voltages only differ in magnitude by factors between 1 and 5. To properly apply Eq. (5.18) to a junction then, one must measure all of the terminal voltages.

5.6. Antidot conclusions and outlook

I have conclusively shown that a four-terminal ballistic junction with a central scatterer can generate a transverse thermovoltage when driven by lateral increases in temperature. A scattering-matrix model of a multi-terminal junction was also developed in order to determine if and how the non-linear voltage response was related to the linear temperature response. It was found that these two terms in fact share the same dependence on the transmission function, $t_{\alpha\beta}(E, \{V_\gamma\})$, which allows temperatures and thermopowers to be determined by utilizing information gained from non-linear voltage measurements.

The measurements and theory presented here also demonstrate that the thermopower of a four-terminal ballistic junction is determined by the combined asymmetric energy dependence of the four QPC transmission functions around the central scatterer. This fits in well with the non-linear voltage response measurements, where it is observed that only an asymmetric energy dependence in these transmission functions can account for the electronic rectification [21, 24].

Second generation devices have recently been designed and fabricated, Fig 5.8., and very recently measured on to address the validity of Eqs. (5.25) and (5.29). Initial results hav already shown Eq. (5.29) to be invalid, or at least incomplete. These devices will also allow the primary theory derived here, Eq. (5.18), to be properly checked by taking direct temperature measurements, as well as checking symmetry relations, Eq. (5.15).

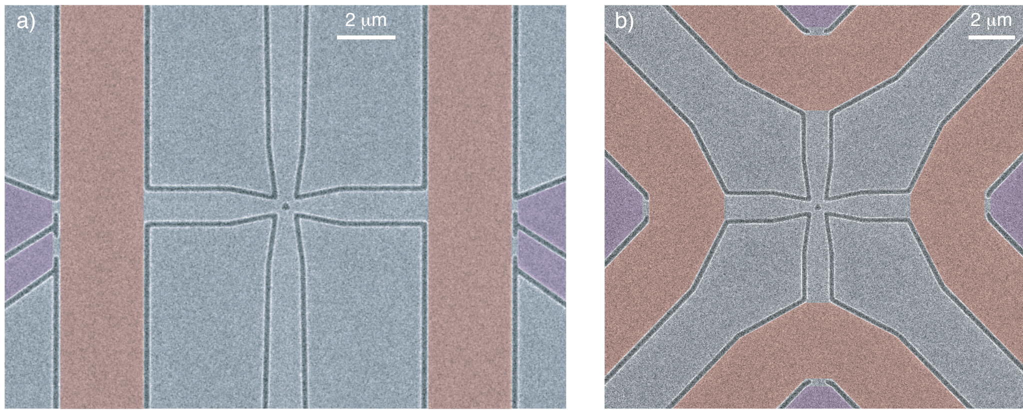

FIGURE 5.8. Second generation devices designed to (a) take direct temperature measurements, and (b) measure the symmetries of the four-terminal junction. Both devices have been designed to confirm the validity of the multi-terminal junction theory derived here. In both figures, red sections represent heating channels and purple sections represent additional voltage probes.

After completing these measurements, the next step in this research is to determine how a 2D-array of such junctions responds to thermal gradients, Fig. 5.9. Experiments have shown such junctions to behave in a similar manner as single junctions [22, 23], which suggests that they too will exhibit transverse thermoelectric effects. Such devices would constitute a novel arena to study functional, mesoscopic, transverse thermoelectric materials.

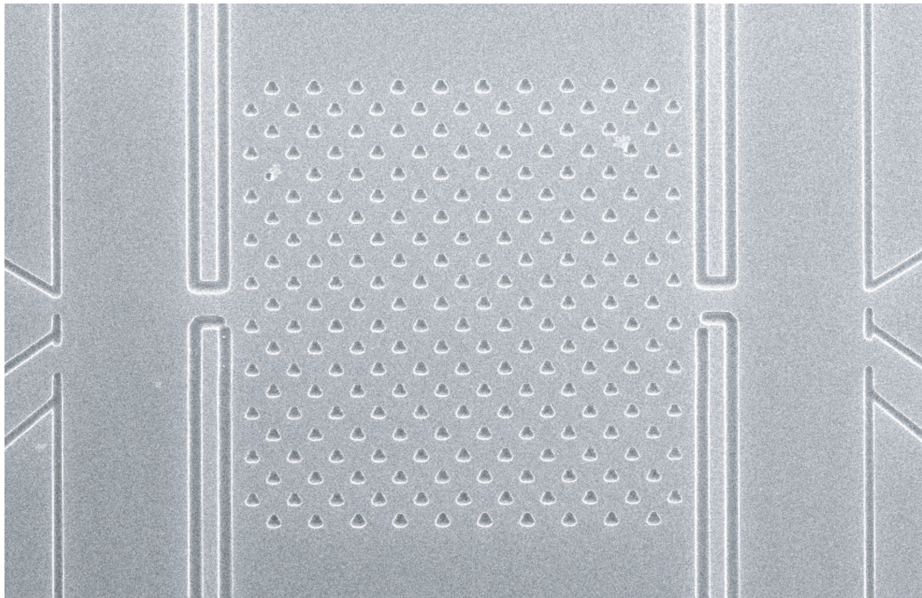

FIGURE 5.9. SEM of a two-dimensional array of triangular scatterers. This device has been fabricated, but not measured on. If confirmed, such a device would constitute the beginnings of functional nano-material.

CHAPTER VI

ANISOTROPIC THERMOELECTRIC MATERIALS

6.1. Introduction to anisotropic thermoelectric materials

It is well-known that both electric and thermal currents will follow the path of least resistance. In isotropic materials, that path lies parallel to the applied electric field or thermal gradient. This must be the case for isotropic materials since by definition all directions are equivalent. In contrast, there exists a class of materials that are categorized as anisotropic, which are defined by their directional dependent transport properties. Due to this directional dependence, the path of least resistance, in general, will not lie along the applied electric field or thermal gradient. The implication for thermoelectrics is that the direction of electric and thermal currents are no longer required to be parallel.

Nearly all commercial thermoelectric modules are made from isotropic homogeneous materials, which, for reasons described in Chapter II, requires them to use two different thermoelectric materials to be of any use. The directional-dependent transport properties of anisotropic materials, on the other hand, allows a single material to be used to create a working thermoelectric module.

In such systems, there are two ways to setup a thermoelectric module: one where the electric current and thermal gradient are parallel, the parallel-flux configuration, and one where they are perpendicular, the perpendicular-flux configuration. For the remainder of the chapter the parallel and perpendicular-flux configurations are defined with respect to the electric current; that is, the direction of the thermal gradient

changes when changing the thermoelectric configuration. Here the electric current will always be along the x-axis. See Fig. 6.1. for schematics on both configurations.

Over the past two centuries, the theory describing isotropic materials has been well established [5]. The amount of research on anisotropic thermoelectric materials, however, has been far less. Though isotropic materials can be used as a template for anisotropics, holes in the theory on anisotropic thermoelectrics remain. Of the sporadic research that has been conducted, some have been concerned with experimentally demonstrating transverse thermoelectric phenomenon through the laser heating of thin films [18, 63–67], measuring Peltier effects [17, 28], or transverse thermopower characterization through single sided heating [7, 68]. Others have concentrated on the theory behind anisotropic thermoelectrics, example of which are: heat flow through an anisotropic material [14], deriving max FOM conditions with starting assumptions [16, 27, 69], and the first full derivation of the efficiency in the parallel flux configuration [19].

While past research does prove the effects of anisotropic thermoelectrics, only half of the theory behind the efficiency of these materials has been derived. In 2009, the FOM for an anisotropic thermoelectric cell operating in the parallel configuration was derived [19]. To date, however, a derivation of the thermoelectric efficiency and FOM for an anisotropic material operating in the perpendicular configuration, the second half of anisotropic thermoelectrics, has not been derived. It is this gap that has motivated the research in this chapter.

With no explicit theory, some researchers, but not all, have used isotropic thermoelectric results, Eq. (2.33), to guess the anisotropic FOM equation in the perpendicular flux configuration. Using the cell depicted in Fig. 6.1.b as a reference, the first two parts of the guess are: (1) the thermopower S should be replaced by the

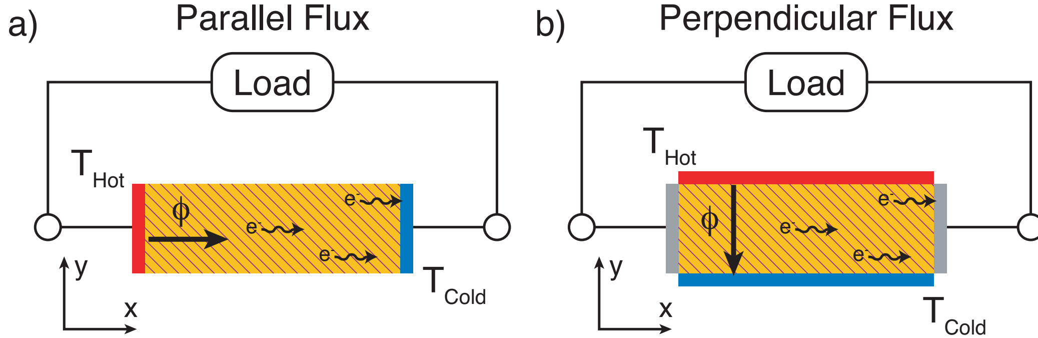

FIGURE 6.1. Schematics of the two methods to create a thermoelectric cell from an anisotropic thermoelectric material. The direction of the heat flux in each cell is given by ϕ, which is along the x-axis for the parallel flux case, and along the y-axis in the perpendicular flux case. The direction of electric current flow is always along the x-axis. The two schematics here are representative of the models I consider later. In (a), I assume the hot and cold baths also act as perfect conductors, meaning $\sigma_{Leads} \gg \sigma_{T.E.}$ and $S = 0$. In (b) the grey vertical bars represent ideal electrical contacts, while the hot and cold baths are connected to the entire top and bottom sides of the cell.

Seebeck matrix component that describes the transverse thermovoltage, S_{xy}, and (2) the thermal conductivity κ should be replaced by the matrix component describing the thermal conductivity parallel to the thermal gradient, κ_{yy}. The difficult part, where researchers differ, comes when we consider the electrical component to the FOM. From Eq. (2.33), we can choose the electrical conductivity, σ_{xx},

$$Z\bar{T}_{\sigma} = \frac{S_{xy}^2 \sigma_{xx}}{\kappa_{yy}} \bar{T}\,, \tag{6.1}$$

or resistivity, ρ_{xx},

$$Z\bar{T}_{\rho} = \frac{S_{xy}^2}{\kappa_{yy} \rho_{xx}} \bar{T}\,, \tag{6.2}$$

where $\bar{T}$ is the average temperature. From here on, these equations will be referred to as the σ- and ρ-FOM, respectively. A derivation of ρ-FOM was given in Ref. [69];

however, this derivation assumes that only the thermopower is anisotropic, and thus neglects the general case. No derivation of the σ-FOM has been made.

It is clear that these two equations are not equal, since in the general case $\rho_{xx} \neq \sigma_{xx}^{-1}$. Surprisingly, however, both equations are used in the literature: Refs. [7, 28] for σ-FOM, and Refs. [16, 17, 27] for ρ-FOM. An interesting aspect here is that for a tilted Si/Al stacked multilayer material, an artificial anisotropic thermoelectric material, the σ-FOM predicts values around 4, while the ρ-FOM equation predicts a value around 10^{-4}. FOM values around 4 would allow thermoelectrics to compete with commercial heat pumps and engines, revolutionizing parts of the energy industry. Here stands the primary question addressed in this chapter, 'Which FOM equation is correct?'

6.1.1. Which FOM equation is correct?

For the remainder of this chapter, I will focus on answering the question of which equation is correct, the ρ-FOM or σ-FOM. To answer this question, I first give an overview of stacked, multi-layered thermoelectric materials. This will lead into the analytical derivation and computational model of the efficiency of the perpendicular flux configuration. Here I will show that the transverse efficiency can be written as

$$Z\bar{T}_{\perp} = \frac{S_{xy}^2 \bar{T}}{\rho_{xx}\kappa_{yy}} \frac{\left(1 - \frac{S_{xx}\kappa_{xy}}{S_{xy}\kappa_{xx}}\right)^2}{\left(1 - \frac{\kappa_{xy}^2}{\kappa_{xx}\kappa_{yy}}\right)\left(1 + \frac{S_{xx}^2 \bar{T}}{\kappa_{xx}\rho_{xx}}\right)} . \tag{6.3}$$

Finally, the advantages of a transverse thermoelectric module will be considered.

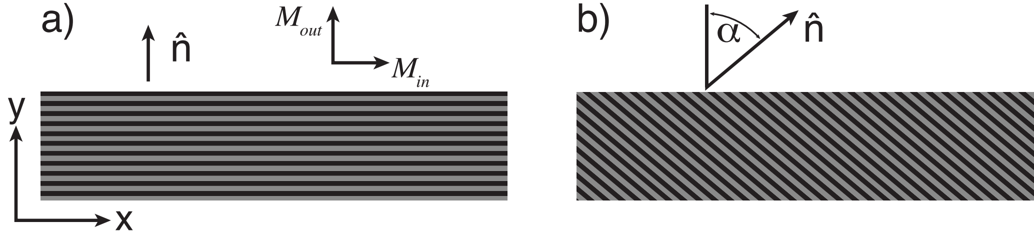

FIGURE 6.2. Schematic of a stacked multilayer (a) before and (b) after tilting and cutting the stack at an angle α to the stacking direction. The black and grey layers represent the two different materials. In (a), the in-plane and out-of-plane material directions are denoted by M_{in} and M_{out}, respectively.

6.2. Artificial anisotropic materials

Many natural materials have asymmetric crystal structures—piezoelectric materials, for instance, that give rise to anisotropic transport properties. In order to begin understanding this class of materials, I must first discuss how these materials are described theoretically. In addition to this, I'm primarily interested in answering the $ZT \approx 4$ question stated in the previous section; therefore the focus here will be on tilted multi-layered structures. The end results will be applicable to all anisotropic materials.

The basic structure of a multi-layered material is shown in Fig. 6.2.a. The transport properties of such a stack depend on the directional axis being considered, $\hat{n}$, and thus cannot be described using scalar quantities as isotropic materials can. These materials must instead be described by matrices,

$$\tilde{M} = \begin{pmatrix} M_{in} & 0 & 0 \\ 0 & M_{out} & 0 \\ 0 & 0 & M_{in} \end{pmatrix}, \tag{6.4}$$

where $\tilde{M}$ represents the electrical conductivity, $\tilde{\sigma}$, thermal conductivity, $\tilde{\kappa}$, or thermopower, $\tilde{S}$, of the stacked material. The subscripts here denote the in-plane and out-of-plane material properties. Since the effective material is isotropic in the plane of the stack, orthogonal to $\hat{n}$, the transport properties in these two directions can be described with the same quantity, M_{in}. The direction perpendicular to the stack however, or out of the plane, must be described by a second quantity, M_{out}.

The three transport matrices of a stacked multilayer can be derived by treating the alternating layers, A and B, as electrical and thermal resistors in series and parallel [16]. For example, the effective in-plane electrical resistance can be calculated by considering two layers of thickness d_A and d_B, and with width and length of w and L, respectively. The total conductance in this case is

$$\begin{aligned} G_{in} &= G_A + G_B \\ \frac{\sigma_{in} w (d_A + d_B)}{L} &= \frac{\sigma_A w d_A}{L} + \frac{\sigma_B w d_B}{L} \\ \sigma_{in}(d_A + d_B) &= \sigma_A d_A + \sigma_B d_B \\ \sigma_{in} &= \frac{\sigma_A + p\sigma_B}{1+p}\,, \end{aligned} \tag{6.5}$$

where $p = d_B/d_A$. Performing the same type of calculations for the remaining properties leads to the components of the effective transport matrices [16]:

$$\begin{aligned} \sigma_{in} &= \tfrac{\sigma_A + p\sigma_B}{1+p} & \sigma_{out} &= \tfrac{\sigma_A \sigma_B (1+p)}{\sigma_B + p\sigma_A} \\ \kappa_{in} &= \tfrac{\kappa_A + p\kappa_B}{1+p}\left(1 + Z_{12}\bar{T}\right) & \kappa_{out} &= \tfrac{\kappa_A \kappa_B (1+p)}{\kappa_B + p\kappa_A} \\ S_{in} &= \tfrac{S_A \sigma_A + p S_B \sigma_B}{\sigma_A + p\sigma_B} & S_{out} &= \tfrac{S_A \kappa_B + p S_B \kappa_A}{\kappa_B + p\kappa_A} \end{aligned} \tag{6.6}$$

where $\bar{T}$ is the average temperature, and Z_{12} is defined as,

$$Z_{12} = \frac{(S_A - S_B)^2}{(\kappa_A + p\kappa_B)\left(\frac{1}{\sigma_A} + \frac{1}{p\sigma_B}\right)}. \tag{6.7}$$

In order for a material to create transverse effects, its transport properties must have non-zero off-diagonal components. As written in Eq. (6.4), the stacked multilayer does not readily appear to be have this quality; however, by applying fields in directions that are neither in the in-plane nor out-of-plane directions, transverse effects will appear. Rather than applying electric or thermal gradients in such a manner, a more useful method is to tilt the stacking direction during fabrication. This can be accomplished by either growing or cutting an angled set of layers like that shown in Fig. 6.2.b [63, 66]. The rotated transport properties can be calculated by rotating the matrices described by Eq. (6.4). A rotation about the z-axis gives,

$$\tilde{M} = \begin{pmatrix} M_{in}\cos^2(\alpha) + M_{out}\sin^2(\alpha) & \frac{1}{2}(M_{in} - M_{out})\sin(2\alpha) & 0 \\ \frac{1}{2}(M_{in} - M_{out})\sin(2\alpha) & M_{in}\sin^2(\alpha) + M_{out}\cos^2(\alpha) & 0 \\ 0 & 0 & M_{in} \end{pmatrix}. \tag{6.8}$$

6.3. Analytic analysis of the anisotropic thermoelectric system

In this section I will derive the thermoelectric efficiency, as defined in Eq. 2.21, of an anisotropic material operating in the perpendicular flux configuration. As stated before, this is the ratio of the electric power delivered to a load resistor to the heat leaving the hot reservoir. The goal here is to write a set of equations for an anisotropic system that resemble the isotropic efficiency derivation in Chapter II. From there, I can utilize much of that derivation to quickly derive the perpendicular flux, anisotropic efficiency. To that end, the anisotropic efficiency derivation starts by writing the

electric and thermal flux equations, Eqs. (2.4) and (2.5), for the anisotropic cell with all scalar quantities, as opposed to matrices and vectors. These equations will then be used to calculate the total amount of heat leaving the hot reservoir, from which the efficiency can be calculated.

6.3.1. Derivation of the effective flux equations

As discussed in the Chapter II, the equations describing a thermoelectric system can be written as,

$$\vec{J} = \tilde{\sigma} \cdot \left(\vec{E} - \tilde{S} \cdot \vec{\nabla} T \right), \tag{6.9}$$

$$\vec{\phi} = T\tilde{S} \cdot \vec{J} - \tilde{\kappa} \cdot \vec{\nabla} T, \tag{6.10}$$

$$\vec{\nabla} \cdot \vec{\phi} = \vec{J} \cdot \vec{E}, \tag{6.11}$$

$$\vec{\nabla} \cdot \vec{J} = 0. \tag{6.12}$$

The goal here is write Eqs. (6.9) and (6.10) as

$$J_x = \sigma_{eff} \left(E_x - S_{eff} \partial_y T \right) \tag{6.13}$$

$$\phi_y = T S_{eff} J_x - \kappa_{eff} \partial_y T \, , \tag{6.14}$$

where σ_{eff}, κ_{eff}, and S_{eff}, are effective scalar transport properties for anisotropic cell in the perpendicular configuration. The specific geometry that I will analyze here is shown in Fig. 6.3., along with its boundary conditions and the average fluxes.

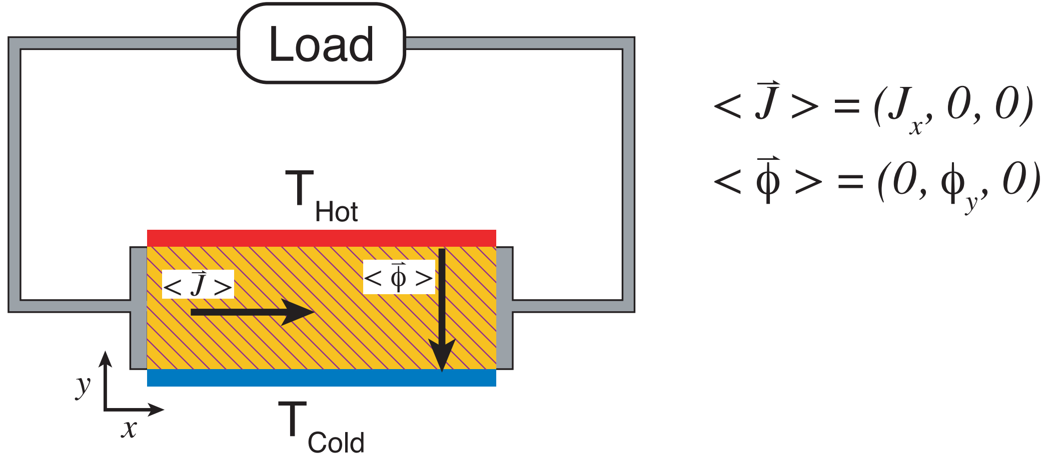

FIGURE 6.3. Anisotropic module for the efficiency derivation. The top and bottom surfaces are used to apply the thermal gradient and are electrically insulating. The left and right surfaces are electrically connected to the load resistor and act as ideal thermal insulators. The average electric current density through the thermoelectric material is along the x-axis, while the average heat flux is along the y-axis.

Following the procedure laid out in Ref. [19], I first write the matrix transport properties, $\tilde{\sigma}$, $\tilde{\kappa}$, or $\tilde{S}$, in the form

$$\tilde{M} = \begin{pmatrix} M_{\parallel} & \vec{M}_{od}^T \\ \vec{M}_{od} & \tilde{M}_{\perp} \end{pmatrix}, \tag{6.15}$$

where

$$\vec{M}_{od} = \begin{pmatrix} M_{yx} \\ M_{zx} \end{pmatrix}, \qquad \tilde{M}_{\perp} = \begin{pmatrix} M_{yy} & M_{yz} \\ M_{zy} & M_{zz} \end{pmatrix}. \tag{6.16}$$

Following this definition, I also define vectors in the system as,

$$\vec{N} = \begin{pmatrix} N_{\parallel} \\ \vec{N}_{\perp} \end{pmatrix}, \tag{6.17}$$

where

$$N_{\|} = N_x \qquad \vec{N}_{\perp} = \begin{pmatrix} N_y \\ N_z \end{pmatrix}. \tag{6.18}$$

The matrices and vectors are written in this way to simplify the mathematics involved in this derivation. In this context, the parallel, $||$ and perpendicular, $\perp$, directions are relative to the average electric current through the cell, which in this case is along the x-axis, Fig. 6.3.

There are two volumed-averaged boundary conditions for the perpendicular-flux system that can be readily identified: zero net heat flux along the parallel axis, $\phi_{\|} = 0$, and zero net electric current along the perpendicular axis, $\vec{J}_{\perp} = 0$. Here volume-averaged means that the said quantity is averaged over the entire volume of the thermoelectric material. For a constant vector field, this will simply return the vector field evaluated at any given point. For a non-zero vector field with a spatial dependence, however, this quantity can be a zero or non-zero vector.

I will first focus on the heat flux through the cell. With the given condition for the heat flux, $\phi_{\|} = 0$, Eq. (6.10) can be written as

$$\begin{aligned} \vec{\phi} &= T\tilde{S} \cdot \vec{J} - \tilde{\kappa} \cdot \vec{\nabla} T \\ \begin{pmatrix} 0 \\ \vec{\phi}_{\perp} \end{pmatrix} &= T \begin{pmatrix} S_{\|} & \vec{S}_{od}^{T} \\ \vec{S}_{od} & \tilde{S}_{\perp} \end{pmatrix} \begin{pmatrix} J_{\|} \\ \vec{J}_{\perp} \end{pmatrix} - \begin{pmatrix} \kappa_{\|} & \vec{\kappa}_{od}^{T} \\ \vec{\kappa}_{od} & \tilde{\kappa}_{\perp} \end{pmatrix} \begin{pmatrix} \nabla_{\|} T \\ \vec{\nabla}_{\perp} T \end{pmatrix} \\ &= \begin{pmatrix} T S_{\|} J_{\|} - \kappa_{\|} \nabla_{\|} T - \vec{\kappa}_{od}^{T} \cdot \vec{\nabla}_{\perp} T \\ T\vec{S}_{od} J_{\|} - \vec{\kappa}_{od} \nabla_{\|} T - \tilde{\kappa}_{\perp} \cdot \vec{\nabla}_{\perp} T \end{pmatrix}. \end{aligned} \tag{6.19}$$

The parallel component of this equation gives an equation for $\nabla_{\|}T$ as a function of $J_{\|}$ and $\vec{\nabla}_{\perp}T$.

$$\begin{aligned} 0 &= TS_{\|}J_{\|} - \kappa_{\|}\nabla_{\|}T - \vec{\kappa}_{od}^{T} \cdot \vec{\nabla}_{\perp}T \\ \nabla_{\|}T &= \kappa_{\|}^{-1}\left(TS_{\|}J_{\|} - \vec{\kappa}_{od}^{T} \cdot \vec{\nabla}_{\perp}T\right) \end{aligned} \tag{6.20}$$

Inserting $\nabla_{\|}T$ into the perpendicular component of Eq. (6.19) gives,

$$\begin{aligned} \vec{\phi}_{\perp} &= T\vec{S}_{od}J_{\|} - \vec{\kappa}_{od}\nabla_{\|}T - \tilde{\kappa}_{\perp} \cdot \vec{\nabla}_{\perp}T \\ &= T\vec{S}_{od}J_{\|} - \vec{\kappa}_{od}\kappa_{\|}^{-1}\left(TS_{\|}J_{\|} - \vec{\kappa}_{od}^{T} \cdot \vec{\nabla}_{\perp}T\right) - \tilde{\kappa}_{\perp} \cdot \vec{\nabla}_{\perp}T \\ &= T\left(\vec{S}_{od} - S_{\|}\kappa_{\|}^{-1}\vec{\kappa}_{od}\right)J_{\|} - \left(\tilde{\kappa}_{\perp} - \kappa_{\|}^{-1}\vec{\kappa}_{od} \otimes \vec{\kappa}_{od}^{T}\right) \cdot \vec{\nabla}_{\perp}T \end{aligned} \tag{6.21}$$

Note that the product $\vec{\kappa}_{od} \otimes \vec{\kappa}_{od}^{T}$ is a 2×2 matrix. Recall that our goal here is to identify equations for an anisotropic system that resemble the equations for an isotropic system. Comparing Eq. (6.21) to Eq. (6.14), I define effective values for the thermal conductivity and thermopower:

$$\vec{S}_{eff} = \vec{S}_{od} - S_{\|}\kappa_{\|}^{-1}\vec{\kappa}_{od}\,, \tag{6.22}$$

$$\tilde{\kappa}_{eff} = \tilde{\kappa}_{\perp} - \kappa_{\|}^{-1}\vec{\kappa}_{od} \otimes \vec{\kappa}_{od}^{T}\,. \tag{6.23}$$

This simplifies $\vec{\phi}_{\perp}$ to

$$\vec{\phi}_{\perp} = T\vec{S}_{eff}J_{\|} - \tilde{\kappa}_{eff} \cdot \vec{\nabla}_{\perp}T\,. \tag{6.24}$$

I leave this equation as is for now, and move on to the electric current density.

I first define the effective electric field vector, $\vec{F}$,

$$\vec{F} = \vec{E} - \tilde{S}\vec{\nabla}T \,. \tag{6.25}$$

With this definition, Eq. (6.9) becomes

$$\vec{J} = \tilde{\sigma} \cdot \vec{F} \,. \tag{6.26}$$

Applying the perpendicular condition for the electric current density, $\vec{J}_\perp = 0$, to Eq. (6.26) yields

$$\begin{aligned} \begin{pmatrix} J_\parallel \\ 0 \end{pmatrix} &= \begin{pmatrix} \sigma_\parallel & \vec{\sigma}_{od}^T \\ \vec{\sigma}_{od} & \tilde{\sigma}_\perp \end{pmatrix} \begin{pmatrix} F_\parallel \\ \vec{F}_\perp \end{pmatrix} \\ &= \begin{pmatrix} \sigma_\parallel F_\parallel + \vec{\sigma}_{od}^T \cdot \vec{F}_\perp \\ \vec{\sigma}_{od} F_\parallel + \tilde{\sigma}_\perp \cdot \vec{F}_\perp \end{pmatrix} . \end{aligned} \tag{6.27}$$

The perpendicular component of this equation can be used to find a relationship between $F_\parallel$ and $\vec{F}_\perp$.

$$\vec{F}_\perp = -\tilde{\sigma}_\perp^{-1} \cdot \vec{\sigma}_{od} F_\parallel \tag{6.28}$$

Inserting Eq. (6.28) back into the parallel term in Eq. (6.27) yields

$$\begin{aligned} J_\parallel &= \sigma_\parallel F_\parallel + \vec{\sigma}_{od}^T \cdot \vec{F}_\perp \\ &= \sigma_\parallel F_\parallel - \vec{\sigma}_{od}^T \cdot \tilde{\sigma}_\perp^{-1} \cdot \vec{\sigma}_{od} F_\parallel \\ &= \left(\sigma_\parallel - \vec{\sigma}_{od}^T \cdot \tilde{\sigma}_\perp^{-1} \cdot \vec{\sigma}_{od}\right) F_\parallel \\ &= \sigma_1 \left(E_\parallel - S_\parallel \nabla_\parallel T - \vec{S}_{od}^T \cdot \vec{\nabla}_\perp T\right) , \end{aligned} \tag{6.29}$$

where in the last line I have used the definition of $F_\parallel$ and defined

$$\sigma_1 = \sigma_\parallel - \vec{\sigma}_{od}^T \cdot \tilde{\sigma}_\perp^{-1} \cdot \vec{\sigma}_{od}. \tag{6.30}$$

Finally, removing $\nabla_\parallel T$ using Eq. (6.20) gives

$$\begin{aligned}
J_\parallel &= \sigma_1 \left(E_\parallel - S_\parallel \nabla_\parallel T - \vec{S}_{od}^T \cdot \vec{\nabla}_\perp T \right) \\
J_\parallel &= \sigma_1 \left(E_\parallel - S_\parallel \kappa_\parallel^{-1} \left(T S_\parallel J_\parallel - \vec{\kappa}_{od}^T \cdot \vec{\nabla}_\perp T \right) - \vec{S}_{od}^T \cdot \vec{\nabla}_\perp T \right) \\
J_\parallel &= \sigma_1 \left(E_\parallel - T \kappa_\parallel^{-1} S_\parallel^2 J_\parallel + S_\parallel \kappa_\parallel^{-1} \vec{\kappa}_{od}^T \cdot \vec{\nabla}_\perp T - \vec{S}_{od}^T \cdot \vec{\nabla}_\perp T \right) \\
\left(1 + \sigma_1 T S_\parallel^2 \kappa_\parallel^{-1} \right) J_\parallel &= \sigma_1 \left(E_\parallel - \left(\vec{S}_{od}^T - S_\parallel \kappa_\parallel^{-1} \vec{\kappa}_{od}^T \right) \cdot \vec{\nabla}_\perp T \right) \\
J_\parallel &= \frac{\sigma_1}{1 + T S_\parallel^2 \sigma_1 \kappa_\parallel^{-1}} \left(E_\parallel - \left(\vec{S}_{od}^T - S_\parallel \kappa_\parallel^{-1} \vec{\kappa}_{od}^T \right) \cdot \vec{\nabla}_\perp T \right) \\
J_\parallel &= \sigma_{eff} \left(E_\parallel - \vec{S}_{eff}^T \cdot \vec{\nabla}_\perp T \right) ,
\end{aligned} \tag{6.31}$$

where I have used the definition of $\vec{S}_{eff}$, Eq. (6.22), and defined the effective electrical conductivity as

$$\sigma_{eff} = \frac{\sigma_1}{1 + T S_\parallel^2 \sigma_1 \kappa_\parallel^{-1}} . \tag{6.32}$$

Though Eqs. (6.24) and (6.31) are not scalar equations as written, they can be reduced to scalar equations by fully writing out the matrix and vector components. To show this, I'll first write out Eqs. (6.22) and (6.23). Using the system shown in Fig. 6.3.b, the transport properties can be written as,

$$\tilde{M} = \begin{pmatrix} M_{xx} & M_{xy} & 0 \\ M_{xy} & M_{yy} & 0 \\ 0 & 0 & M_{zz} \end{pmatrix} . \tag{6.33}$$

Here I have assumed that the transport matrices are symmetric, $M_{jk} = M_{kj}$, as is the case in tilted anisotropic systems. Using this arrangement, the effective thermopower vector is,

$$\vec{S}_{eff} = \begin{pmatrix} S_{eff} \\ 0 \end{pmatrix} \tag{6.34}$$

$$S_{eff} \equiv S_{xy} - S_{xx}\frac{\kappa_{xy}}{\kappa_{xx}}, \tag{6.35}$$

and the effective thermal conductivity matrix is,

$$\tilde{k}_{eff} = \begin{pmatrix} \kappa_{eff} & 0 \\ 0 & \kappa_{zz} \end{pmatrix} \tag{6.36}$$

$$\kappa_{eff} \equiv \kappa_{yy} - \frac{\kappa_{xy}^2}{\kappa_{xx}}. \tag{6.37}$$

For completeness, σ_{eff} can also be written out in terms of the transport matrices' components. To do this, I must first evaluate σ_1.

$$\begin{aligned}
\sigma_1 &= \sigma_{\parallel} - \vec{\sigma}_{od}^T \cdot \tilde{\sigma}_{\perp}^{-1} \cdot \vec{\sigma}_{od} \\
&= \sigma_{xx} - \begin{pmatrix} \sigma_{xy} & 0 \end{pmatrix} \cdot \begin{pmatrix} \frac{1}{\sigma_{yy}} & 0 \\ 0 & \frac{1}{\sigma_{zz}} \end{pmatrix} \cdot \begin{pmatrix} \sigma_{xy} \\ 0 \end{pmatrix} \\
&= \sigma_{xx} - \frac{\sigma_{xy}^2}{\sigma_{yy}} \\
&= \frac{\sigma_{xx}\sigma_{yy} - \sigma_{xy}\sigma_{yx}}{\sigma_{yy}} \\
&= \frac{1}{\rho_{xx}}
\end{aligned} \tag{6.38}$$

The second to last step is simply the inverse of the ρ_{xx} element of the 2-D resistivity matrix.

$$\tilde{\rho} = \begin{pmatrix} \sigma_{xx} & \sigma_{xy} \\ \sigma_{yx} & \sigma_{yy} \end{pmatrix}^{-1} = \frac{1}{\sigma_{xx}\sigma_{yy} - \sigma_{xy}\sigma_{yx}} \begin{pmatrix} \sigma_{yy} & -\sigma_{xy} \\ -\sigma_{yx} & \sigma_{xx} \end{pmatrix} \tag{6.39}$$

From Eq. (6.32), the effective electrical conductivity is,

$$\sigma_{eff} = \frac{\frac{1}{\rho_{xx}}}{1 + \frac{TS_{xx}^2}{\kappa_{xx}\rho_{xx}}}. \tag{6.40}$$

Finally, using Eq. (6.18) to write $\vec{\nabla}_{\perp}T$and $J_{\parallel}$,

$$\vec{\nabla}_{\perp}T = \begin{pmatrix} \partial_y T \\ 0 \end{pmatrix} \tag{6.41}$$

$$J_{\parallel} = J_x\,, \tag{6.42}$$

Eq. (6.24) can be written as

$$\begin{aligned} \vec{\phi}_{\perp} &= T\vec{S}_{eff}J_{\parallel} - \tilde{\kappa}_{eff} \cdot \vec{\nabla}_{\perp}T \\ &= \begin{pmatrix} TS_{eff}J_x \\ 0 \end{pmatrix} - \begin{pmatrix} \kappa_{eff} & 0 \\ 0 & \kappa_{zz} \end{pmatrix} \cdot \begin{pmatrix} \partial_y T \\ 0 \end{pmatrix} \\ &= \begin{pmatrix} TS_{eff}J_x - \kappa_{eff}\partial_y T \\ 0 \end{pmatrix}. \end{aligned} \tag{6.43}$$

The zero heat flux along the z-axis simply reflects the translational symmetry along the z-axis in the cell, Fig. 6.3. Since there is zero heat flux along the z-axis, I can reduce the system to a two-dimensional problem in the xy-plane yielding the final heat

flux equation for an anisotropic thermoelectric in the perpendicular configuration.

$$\phi_y = TS_{eff}J_x - \kappa_{eff}\partial_y T \tag{6.44}$$

Using Eqs. (6.34), (6.41), and (6.42) in Eq. (6.31) yields a similar scalar equation for $J_\parallel$.

$$\begin{aligned}
J_\parallel &= \sigma_{eff}\left(E_\parallel - \vec{S}^T_{eff}\cdot\vec{\nabla}_\perp T\right)\\
J_x &= \sigma_{eff}\left(E_x - \begin{pmatrix} S_{eff} & 0 \end{pmatrix}\cdot\begin{pmatrix} \partial_y T \\ 0 \end{pmatrix}\right)\\
J_x &= \sigma_{eff}\left(E_x - S_{eff}\partial_y T\right)
\end{aligned} \tag{6.45}$$

6.3.2. Derivation of the efficiency in the perpendicular configuration

Though Eqs. (6.44) and (6.45) look similar to the isotropic equations, the analysis to determine the maximum efficiency must be modified slightly due to the electric current density and heat flux being along different axes. In contrast to the parallel configuration, where the electric current density and heat flux have the same cross sectional area, in the perpendicular configuration the electric current density and heat flux can have unique cross sectional areas. This change must be taken into account in order to calculate the efficiency and power output.

The derivation here will start by determining the temperature profile of the cell shown in Fig. 6.3. I will take the thermoelectric material to have sides of lengths L_x, L_y, and L_z. The cross sectional area seen by the electric current density is $A_V = L_y L_z$, while the area seen by the heat flux is $A_T = L_x L_z$. Once the temperature is known, the efficiency can be calculated in the same manner as for the isotropic case.

The temperature profile can be calculated by using the thermoelectric heat equation, Eq. (2.9), by replacing the matrix and vector quantities with the corresponding scalar quantities. As in Chapter II, I assume the medium to be homogeneous and having transport properties that are independent of temperature.

$$-\vec{\nabla} \cdot \left(\tilde{\kappa} \cdot \vec{\nabla} T \right) = \vec{J} \cdot \tilde{\rho} \cdot \vec{J} - T \vec{\nabla} \cdot \left(\tilde{S} \cdot \vec{J} \right)$$

$$-\kappa_{eff} \partial_y^2 T = \rho_{eff} J_x^2 \tag{6.46}$$

Here $\rho_{eff} = \sigma_{eff}^{-1}$. In the open circuit case, the solution to this equation is trivial. In the closed circuit case, the solution is,

$$T(y) = \left[T_h - \Delta T \frac{y}{L_y} \right] + \frac{\rho_{eff} J_x^2}{2\kappa_{eff}} y \left(L_y - y \right). \tag{6.47}$$

The efficiency is calculated from the ratio of the power delivered to a load resistor, $P_{Load} = I^2 R_L$, and the heat leaving the hot reservoir, Q_h. The heat leaving the hot reservoir is given by

$$\begin{aligned} Q_h &= A_T \phi|_{y=0} \\ &= A_T \left(T S_{eff} J_x - \kappa_{eff} \frac{\partial T}{\partial y} \right)_{y=0} \\ &= A_T T_h S_{eff} J_x + A_T \kappa_{eff} \frac{\Delta T}{L_y} - A_T L_y \frac{\rho_{eff} J_x^2}{2} \\ &= T_h S_{eff} \frac{A_T}{A_V} I + \frac{A_T}{L_y} \kappa_{eff} \Delta T - \frac{1}{2} I^2 \rho_{eff} \frac{A_T L_y}{A_V^2} \\ &= T_h S_{eff} \sqrt{\frac{\gamma_T}{\gamma_V}} I + \gamma_T \kappa_{eff} \Delta T - \frac{1}{2} I^2 \frac{\rho_{eff}}{\gamma_V}, \end{aligned} \tag{6.48}$$

where I have defined $\gamma_T = A_T/L_y$ and $\gamma_V = A_V/L_x$. If I further define the quantities

$$K = \gamma_T \kappa_{eff}, \tag{6.49}$$

$$R = \frac{\rho_{eff}}{\gamma_V} \tag{6.50}$$

and

$$S = S_{eff}\sqrt{\frac{\gamma_T}{\gamma_V}}, \tag{6.51}$$

the heat flux out of the hot reservoir becomes

$$Q_h = T_h S I + K\Delta T - \frac{1}{2} I^2 R, \tag{6.52}$$

which is identical to isotropic case, Eq. (2.26). The current can be estimated from the open-circuit thermovoltage and the total circuit resistance.

For the cell considered here, the transverse thermovoltage is,

$$\begin{aligned} V_{Th} &= E_x L_x \\ &= L_x S_{xy} \frac{\Delta T}{L_y} \\ &= S\Delta T, \end{aligned} \tag{6.53}$$

where I have used the definition of γ_T, γ_V, and S. The current through the circuit is then,

$$I = \frac{V_{Th}}{R + R_L} = \frac{S\Delta T}{R + R_L}. \tag{6.54}$$

Since the equations here for Q_h and I are identical to the corresponding equations for the isotropic case, Eqs. (2.26) and (2.30), the rest of the derivation for the

isotropic case can be used to determine the anisotropic efficiency in the perpendicular configuration. Using the definition of Z, Eq. (A.6) from Appendix A,

$$\begin{aligned} Z &= \frac{S^2}{RK} \\ &= \frac{S_{eff}^2 \gamma_T}{\gamma_V} \frac{\gamma_V}{\rho_{eff}} \frac{1}{\gamma_T \kappa_{eff}} \\ &= \frac{S_{eff}^2 \sigma_1}{\kappa_{eff}} \end{aligned} \tag{6.55}$$

the perpendicular-FOM is

$$Z\bar{T}_{\perp} = \frac{S_{eff}^2 \sigma_1}{\kappa_{eff}} \bar{T}. \tag{6.56}$$

Thus like the isotropic case, the perpendicular-FOM only depends on material properties and does not depend on the specific geometry of the cell. This equation can be written in a more experimentally accessible form by inserting the effective transport properties.

$$\begin{aligned} Z\bar{T}_{\perp} &= \frac{S_{eff}^2 \sigma_1}{\kappa_{eff}} \\ &= \frac{\bar{T}\left(S_{xy} - S_{xx}\frac{\kappa_{xy}}{\kappa_{xx}}\right)^2}{\kappa_{yy} - \frac{\kappa_{xy}^2}{\kappa_{xx}}} \frac{\frac{1}{\rho_{xx}}}{1 + \frac{S_{xx}^2 \bar{T}}{\kappa_{xx}\rho_{xx}}} \\ &= \frac{S_{xy}^2 \bar{T}}{\rho_{xx}\kappa_{yy}} \frac{\left(1 - \frac{S_{xx}\kappa_{xy}}{S_{xy}\kappa_{xx}}\right)^2}{\left(1 - \frac{\kappa_{xy}^2}{\kappa_{xx}\kappa_{yy}}\right)\left(1 + \frac{S_{xx}^2 \bar{T}}{\kappa_{xx}\rho_{xx}}\right)} \end{aligned} \tag{6.57}$$

There are two terms to consider here: the first quotient, which happens to be none other than the ρ-FOM, Eq. (6.2); and the second quotient, which is a manifestation of the transverse electrical and thermal properties. For the Al/Si multi-layer studied here, the second term varies between 1 and 1.08, leaving the first term to essentially dominate the FOM's behavior. Therefore, for this material the ρ-FOM equation

will serve as a very good approximation to the actual FOM. However, this does not preclude other thermoelectric materials from deviating from this result.

For comparison, the FOM for the parallel flux configuration depicted in Fig. 6.1.a was derived in Ref. [19], and can be written as,

$$Z\bar{T}_{\parallel} = \frac{S_{xx}^2 \bar{T}}{\rho_{xx}\kappa_{xx}} \frac{\left(1 - \frac{S_{xy}\kappa_{xy}}{S_{xx}\kappa_{yy}}\right)^2}{\left(1 - \frac{\kappa_{xy}^2}{\kappa_{xx}\kappa_{yy}}\right)\left(1 + \frac{S_{xy}^2 \bar{T}}{\kappa_{yy}\rho_{xx}}\right)}, \tag{6.58}$$

which is, not surprisingly, quite similar to $Z\bar{T}_{\perp}$.

The original question I set out to answer was, 'Which FOM equation is more correct, ρ-FOM or σFOM ?' From Eqs. (6.57) and (6.58) we can see that the ρ-FOM is the more correct equation, which prevents us from achieving the $ZT \sim 4$ we were hoping for.

For the material properties chosen here, the second term was of order unity; however, this does not imply that this will be true for all anisotropic materials. In particular, tilted multi-layered materials were studied here. This may not be the optimum method to create an efficient anisotropic thermoelectric material. As such, researchers might be able capitalize on this additional term to enhance either anisotropic FOM. Such a feat would require researchers to manipulate the anisotropy of a cell such that,

$$\frac{\kappa_{xy}^2}{\kappa_{xx}\kappa_{yy}} \rightarrow 1 \tag{6.59}$$

and

$$\frac{S_{xx}\kappa_{xy}}{S_{xy}\kappa_{xx}} \rightarrow 0 \qquad \text{or} \qquad \frac{S_{xx}\kappa_{xy}}{S_{xy}\kappa_{yy}} \rightarrow 0. \tag{6.60}$$

while maintaining an appreciable ρ-FOM. While it is unclear if such manipulations can be realized in a physical system, the route now exists to exploit.

6.4. Modeling the anisotropic thermoelectric systems

In this section I will present the setup and results of COMSOL simulations of a perpendicular flux anisotropic thermoelectric module. Ultimately, I will show that the efficiency predicted by Eqs. (6.57) and (2.31) closely matches that from simulations. I will also show that the σ-FOM predicts efficiencies far from correct.

The simulations here model a simple single-element thermoelectric module using Eqs. (6.9)-(6.12), and the COMSOL Multiphysics software package. The three-dimensional geometry of the model is shown in Fig. 6.4., while the electrical and thermal boundary conditions are the same as those shown in Fig. 6.3. By varying the material properties between isotropic and anisotropic, this model is capable of modeling either type of material in either the parallel or perpendicular flux configuration.

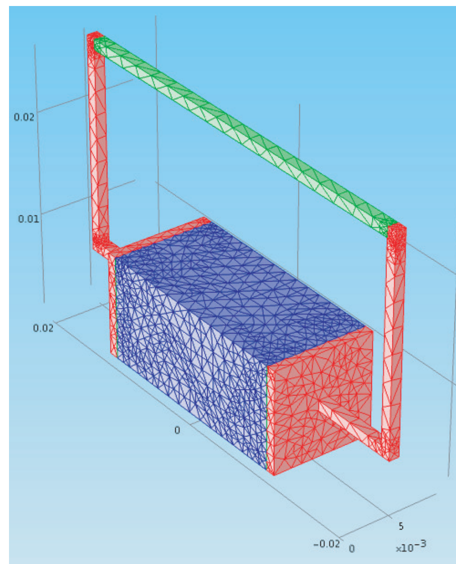

FIGURE 6.4. 3-D geometry used for the thermoelectric COMSOL simulations of the anisotropic material, with the components color coded: the purple section is the thermoelectric material, the green section is the load resistor, and the red sections are ideal metallic leads. Also shown is the tetrahedral mesh for the COMSOL simulations. The boundary conditions for this model were stated in Fig. 6.3.

TABLE 6.1. Bulk transport properties for Al and Si. In the simulations reported here, σ_{Al} was reduced by a factor of 1000, and S_{Si} was reduced by a factor of 10. These reductions were made to make the model computationally solvable.

Material	σ (Ω^{-1}m^{-1})	κ (W/mK)	S (μV/K)
Al	4×10^7	232	-1.66
Si	100	156	1500

Here I will model the efficiency of both configurations for an anisotropic thermoelectric material as a function of the tilt angle, α, and compare the results to the efficiencies predicted from Eqs. (6.57) or (6.58), as well as the corresponding Eqs. (6.2) and (6.1). For both configurations, the material parameters were modeled after a Si/Al stacked multilayer structure with Si layers ten times thicker than the Al layers, $n = 10$. The transport properties for Al and Si are shown in Table 6.1. Due to the large difference in transport properties between Si and Al, COMSOL had difficulties finding acceptable solutions. To get around this difficulty, I reduced the thermopower of the silicon by a factor of 10, and reduced the electrical conductivity of the aluminum by a factor of 1000. These modifications create a system similar to the original Si/Al multilayer structure, while still being solvable by the COMSOL software. This modification is acceptable since I'm only interested in the comparing the efficiencies, and not to a physical system.

For both simulations, the resistivity of the load resistor was matched to the thermoelectric cell resistance, R, through the maximum efficiency condition, Eq. (A.8). Eqs. (6.57) and (6.58) were used to calculate $Z\bar{T}$ in these equations.

6.4.1. Anisotropic simulation results

The simulation results of the anisotropic cell in both flux configurations are shown in Fig. 6.5. The simulation efficiencies were calculated by dividing the power delivered to the load resistor by the heat leaving the hot reservoir. Extracting these quantities is a standard feature in COMSOL. The theoretical efficiencies, η_{The}, η_{ρ}, and η_{σ}, were calculated by inserting their respective ZT values into Eq. (2.31). For both flux configurations the thermoelectric efficiency predicted by the ρ-FOM closely matches the simulated efficiencies when compared to the σ-FOM, and nearly identical to the actual FOM predicted from Eq. (6.57).

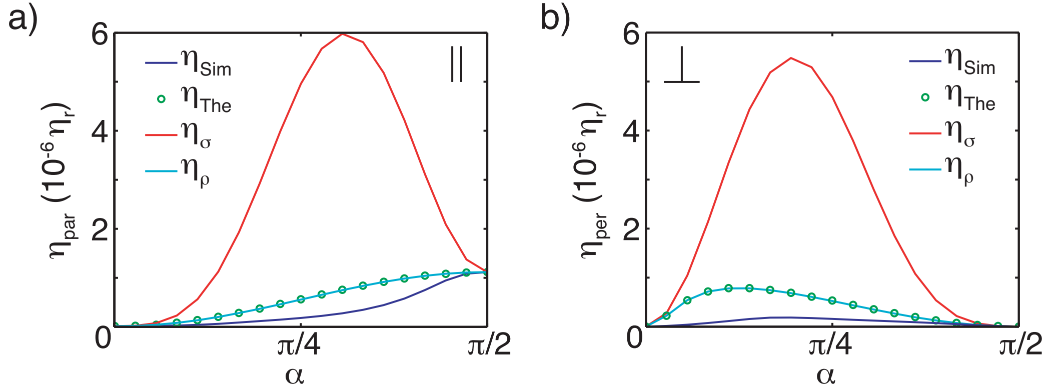

FIGURE 6.5. Efficiency of an anisotropic thermoelectric cell operating in the (a) parallel and (b) perpendicular flux configurations. The absolute magnitudes of the efficiencies shown here are not important since the goal is to compare the theory predictions to the simulations. What is important is the difference between the various efficiencies for each configuration; note that the η_{ρ} predictions are much closer to the simulated efficiencies than the η_{σ} predictions.

6.4.2. Deviations between simulations and theory

In the previous section I noted that the theoretical efficiency derived here is close but not a match to the simulated efficiencies. These differences can be attributed to

assumptions in the analytic derivation, and to the simulated geometry. In deriving the analytic results, it was assumed that the current through the cell could be calculated using the open-circuit voltage and the total resistance. This is clearly an incorrect way to calculate the electric current, since for open-circuit conditions the current is by definition zero. Allowing current to flow requires the driving thermovoltage to decrease, and thus leads to less current flowing through the device than assumed.

A second source of deviation comes from the fact that the COMSOL model simulates current and heat flow through the entire volume of the system. The analytic results, on the other hand, assume average gradients throughout each component's volume. To see what is happening, the electric field and current density at the center of a simulated cell, under open-circuit conditions, were simulated, and are shown in Figure 6.6.a. Also shown are the theory values for the x- and y-components for the electric field; the z-component and all of the current density components are predicted to be zero. There are two notable effects here between $\alpha = 0$ and $\alpha \approx \pi/4$. The first is the large difference in the simulated and theory values for E_y. The second is the fact that the current density is not zero even though this is an open-circuit simulation. Both of these effects stem from the fact that the metallic contacts on the sides of the thermoelectric material electrically short the sides. The net effect of these electrical shorts is to partially cancel out the thermoelectric field near the side electrodes, Fig. 6.6.b. As a consequence, in combination with the thermal gradient, the non-uniform electric field creates two current vortices in the cell. These results suggest that by decreasing the size and changing the position of the electrodes, one could increase the thermoelectric efficiency of the simulated cell.

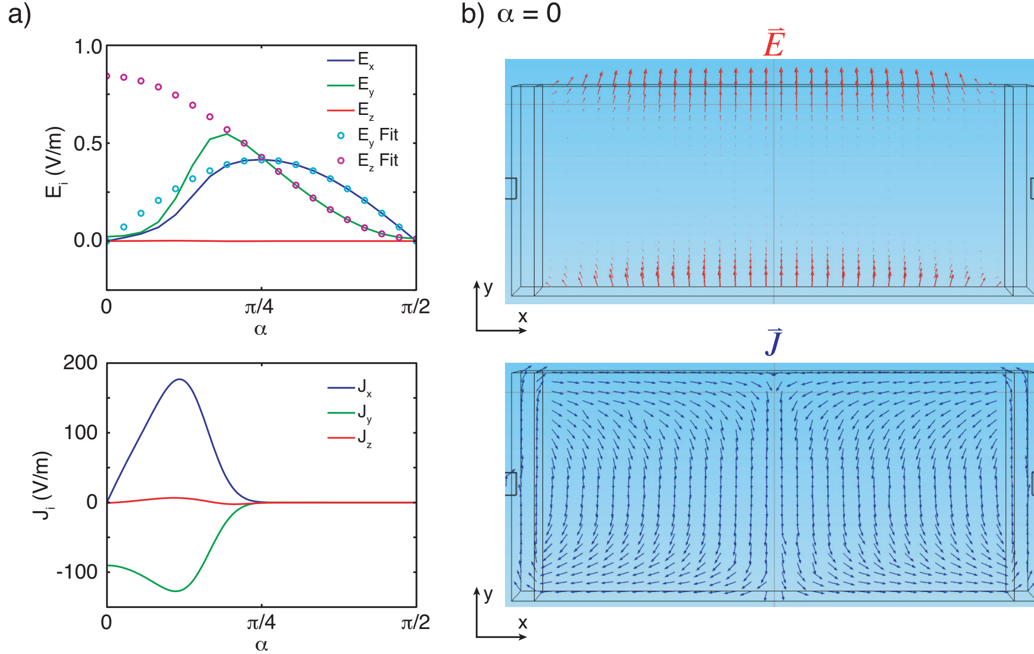

FIGURE 6.6. Effects in the COMSOL simulations due to the side electrode placement. The electric field and current density in (a) are evaluated at the center of the thermoelectric material. The difference between predictions and simulations for $\alpha < \pi/4$ are attributed to the side electrodes. The normalized vector fields in (b) show how the electrodes short the sides of the thermoelectric material, causing reduced electric fields in these regions, and current vortices within the cell.

6.5. Advantages of anisotropic thermoelectric materials

When using isotropic thermoelectric materials, the optimum load resistance, R_L, and output power, P_L, are determined by the transport properties and dimensions of the thermoelectric cell.

$$\begin{aligned} R_L^{op.} &= wR \\ &= \sqrt{1+Z\bar{T}}\left(\frac{\rho L}{A}\right) \end{aligned} \tag{6.61}$$

$$
\begin{aligned}
P_L &= I^2 R_L^{op.} \\
&= \left(\frac{S\Delta T}{R+R_L}\right)^2 R_L^{op.} \\
&= \left(\frac{S\Delta T}{1+w}\right)^2 \frac{w}{R} \\
&= \left(\frac{S\Delta T}{1+w}\right)^2 \frac{wA}{\rho L}
\end{aligned} \tag{6.62}
$$

Here L is the length between the hot and cold reservoirs, and A is the cross sectional area along the direction of heat flow. Both Eqs. (6.61) and (6.62) depend on material properties and the geometric ratio A/L. Once the material for and geometry of a thermoelectric cell have been chosen, both $R_L^{op.}$ and P_L are fixed. For example, if one desired to increase the output power of an isotropic thermoelectric cell by only changing the cell geometry, the optimum load resistance would have to change accordingly.

In contrast, anisotropic materials operating in the perpendicular configuration can independently select the output power and optimum load resistance. To see this, the optimum load resistance of a perpendicular-anisotropic cell is

$$
\begin{aligned}
R_L^{op.} &= wR \\
&= \frac{\rho_{eff}}{\gamma_V} \\
&= \frac{w\rho_{eff} L_x}{L_y L_z} \\
&= w\rho_{eff} \frac{l}{L_z},
\end{aligned} \tag{6.63}
$$

where $l = L_x/L_y$, while the output power is

$$\begin{aligned} P_L &= I^2 R_L^{op.} \\ &= \left(\frac{S\Delta T}{R + R_L^{op.}}\right)^2 R_L^{op.} \\ &= \left(\frac{S\Delta T}{1+w}\right)^2 \frac{w}{R} \\ &= \left(\frac{S_{eff}\Delta T}{1+w}\right)^2 \frac{\gamma_T}{\gamma_V}\frac{w}{\rho_{eff}}\gamma_V \\ &= \left(\frac{S_{eff}\Delta T}{1+w}\right)^2 \frac{w}{\rho_{eff}}\gamma_T \\ &= \left(\frac{S_{eff}\Delta T}{1+w}\right)^2 \frac{w}{\rho_{eff}}\frac{L_x L_z}{L_y} \\ &= \left(\frac{S_{eff}\Delta T}{1+w}\right)^2 \frac{w}{\rho_{eff}} l L_z \,. \end{aligned} \tag{6.64}$$

For this case, $R_L^{op.}$ and P_L depend on the two independent, geometric parameters, l and L_z, in different ways. This difference comes from the fact that the thermal gradient and electric current have different cross sectional areas, A_T and A_V. The differing dependence on l and L_z allows $R_L^{op.}$ and P_L to be chosen independently of each other. Isotropic thermoelectric cells can and are constructed to have this same ability by placing cells in series as well as parallel. There, the heat flux is along the y-axis, while the electric current is extracted along the x-axis. Construction of these modules, however, requires numerous electrical connections to be made, all of which must work for the cell to operate correctly. Comparing this to an anisotropic material's two electrical connections highlights the fabrication-induced complexity of isotropic thermoelectric cells.

6.6. Conclusion

Here I derived the efficiency for an anisotropic thermoelectric material operating with the electric current orthogonal to the applied thermal gradient.

$$Z\bar{T}_{\perp} = \frac{S_{xy}^2 \bar{T}}{\rho_{xx}\kappa_{yy}} \frac{\left(1 - \frac{S_{xx}\kappa_{xy}}{S_{xy}\kappa_{xx}}\right)^2}{\left(1 - \frac{\kappa_{xy}^2}{\kappa_{xx}\kappa_{yy}}\right)\left(1 + \frac{S_{xx}^2 \bar{T}}{\kappa_{xx}\rho_{xx}}\right)} \tag{6.65}$$

In combination with the efficiency already derived for an anisotropic thermoelectric material operating with the electric current parallel to the applied thermal gradient [19], this completes the theory on the efficiency of anisotropic thermoelectric materials. Both equations prove that of the two FOMs quoted in the literature, the ρ-FOM is in fact a better approximation to the actual FOM.

The transverse FOM derived here also highlights a new route to pursue towards higher thermoelectric efficiencies. Namely, if the anisotropy of a material can be manipulated according to Eqs. (6.59) and (6.60) larger FOMs may be possible. Whether such manipulations are possible in a physical system is unclear from the equations given here.

Lastly, I've shown that one advantage anisotropic materials have is the ability to separately choose the optimum load resistance and output power. Such a choice is not possible with conventional isotropic thermoelectric materials without additional electronics. Since thermoelectric energy harvesting is currently limited to niche applications, this added versatility may be beneficial to expanding the use of thermoelectric energy harvesters and sensors.

CHAPTER VII

HEAT FLOW IN INDIUM ARSENIDE NANOWIRES

The experimental data presented in this chapter was gathered by Eric Hoffmann and Stefano Roddaro. Eric Hoffmann took the temperature measurements for the heterostructure nanowire shown in Figs. 7.1. and 7.2., and Stefano Roddaro took the temperature measurements for the nanowire with superconducting leads shown in Fig. G.1. I performed all of the analytic and computational calculations presented in this chapter, as well as all of the writing.

In this chapter, a method to probe the thermal transport properties of InAs nanowires by combining experimental temperature measurements with computational models will be discussed. The main interest here is electron-phonon (e-ph) interaction in InAs nanowires, a quantity that has yet to be fully determined. The following sections discuss the temperature measurements on an InAs heterostructure nanowire system as well as a pure InAs nanowire system. Due to a large amount of overlap between the two systems, the bulk of the description on the pure InAs nanowire system is relegated to the Appendix G. Before diving into the results, an analytic analysis of an e-ph coupled diffusive heat flow model, and COMSOL models of the HNW system is given. The final section will go over the simulation results, where I will show that an interplay between e-ph interaction and diffusive heat flow is an important component in understanding thermal flow at the nanoscale.

7.1. Heterostructure nanowire experiments

Recent temperature measurements on an InAs heterostructure nanowire system have shown an increased temperatures that cannot be explained by electronic heat

diffusion alone. The implication of this is the presence of at least one additional heat flow. It is believed that e-ph coupling plays a prominent role in this unidentified heat flow.

The heterostructure nanowire (HNW) system is comprised of an InAs nanowire with two 5 nm InP barriers separated by roughly 15 nm of InAs. The center InAs section defines a quantum dot within the nanowire and acts as a low-transmission barrier to any traversing electrons. The electrical contacts are comprised of 25 nm Ni / 75 nm Au evaporated film, and the nanowire and contacts rest upon a 100 nm silicon oxide layer on the surface of a doped silicon wafer.

As demonstrated in Ref. [59], the setup in Fig. 7.1. can be used to measure the temperatures of the electrons traversing the QD, known as quantum-dot thermometry. The method uses the thermocurrent and differential conductance of a QD to probe its transmission function, and then uses that knowledge to determine the electron temperatures. By varying the direction of electron flow via a bias voltage, the electron temperature on either side of the dot can be determined. Using this thermometry technique, the source, ΔT_{S}, and drain, ΔT_{D}, electron temperatures near the QD were measured at base temperatures of 1.228, 2.2, 2.94, and 4.25 K by Eric Hoffmann. The results of these measurements are shown in Fig. 7.2.

Attempts to explain the temperatures in Fig. 7.2. using a purely diffusive electron heating model ultimately fail. The typical electrical conductance of the whole nanowire during measurements is on the order of 0.004 $2e^2/h$ [59], while the conductance of pure InAs nanowires of similar size, also grown at Lund University, are on the order of 100 times this [70]. This implies that the measured electrical conductance is primarily controlled by the conductance of the QD. Assuming the Wiedemann-Franz law holds for nanowires, this also implies that the electron thermal

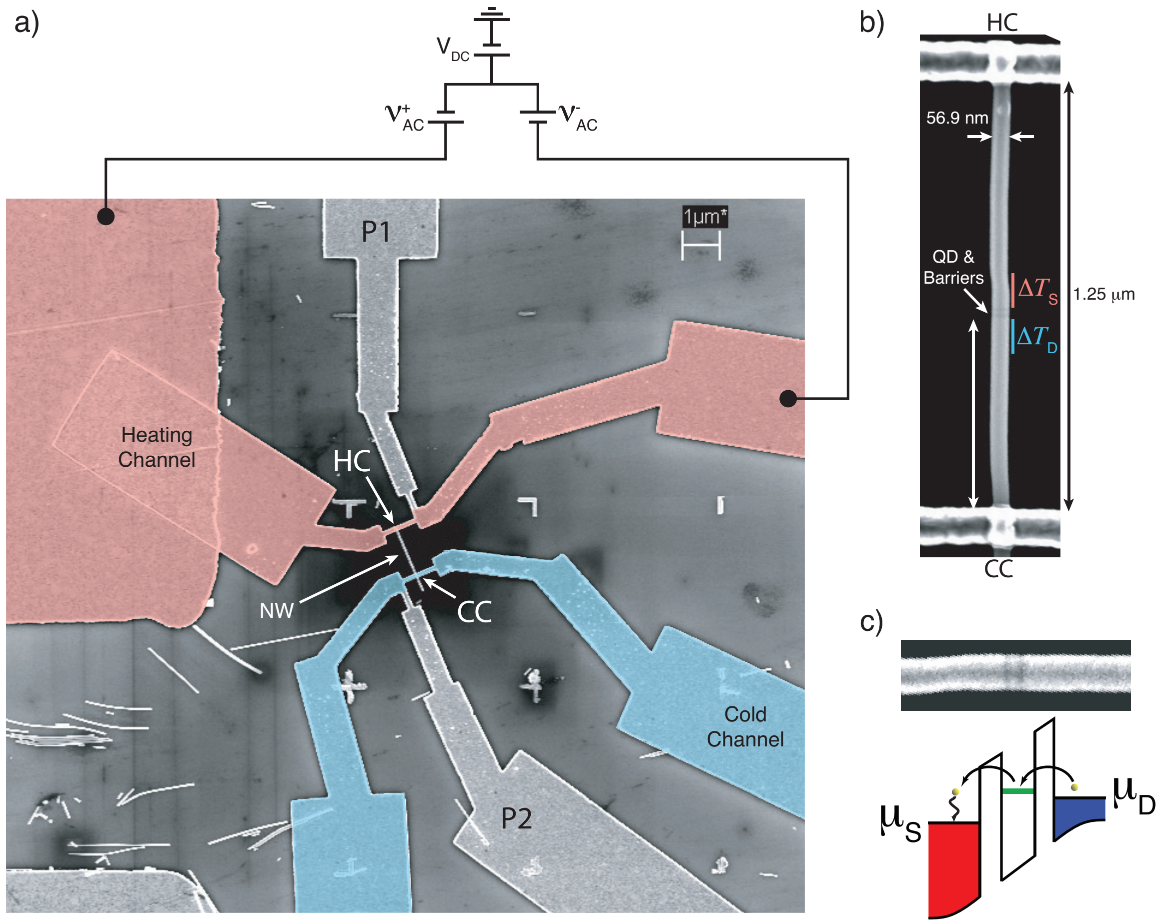

FIGURE 7.1. SEM picture and schematic of the HNW and the connecting leads. The heating contact and cold contact are labeled HC and CC respectively. In (a), a circuit diagram of the applied heating voltages connected to the heating channel are shown. The two AC heating voltages, $\nu^{\pm}_{AC}$, are 180° out of phase with each other. The amplitude of the two heating voltages are adjusted so that the 1ω voltage at the nanowire, as measured by probe P1, is as close to zero as possible. Any DC shift measured at P1 is canceled out by a DC shift, V_{DC}, applied to the heating voltages. (b) A magnified view of the nanowire showing its size, the location of the two InP barriers, and the two temperature measurement regions. The source and drain measurement regions, ΔT_{S} and ΔT_{D}, are labeled by red and blue bars respectively. In (c), the InP barriers are the dark bands within the nanowire. The region between the two InP barriers defines the quantum dot in the nanowire. The energy diagram shows the electron motion during a drain electron temperature measurement.

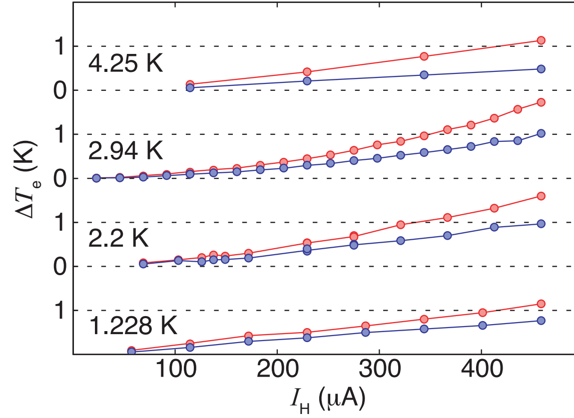

FIGURE 7.2. Measured source (red) and drain (blue) electron temperatures for base temperatures of 1.228, 2.2, 2.94, and 4.25 K.

conductance of the dot, $K_{Dot} \approx 10^{-14}$ W, is on the order of 100 times smaller than the rest of the nanowire, $K_{InAs} \approx 10^{-12}$ W. Physically this can by explained by the far fewer number of electron energies allowed in the QD compared to the nanowire. With such a large difference between thermal conductances, the full temperature drop applied to the nanowire from the metallic contacts would fall across the QD. This would imply $\Delta T_{\rm S} = \Delta T_{\rm SC}$ and $\Delta T_{\rm D} = 0$. Since measurements show $\alpha \Delta T_{\rm D} \approx \Delta T_{\rm S}$, where $\alpha \approx 2$, the diffusive model fails to explain the measured rise in temperature. The goal in later sections of this chapter will be to find a heating mechanism– that is, some method of delivering heat– capable of explaininf the drain electron temperature rise. Throughout this chapter, the term 'heating mechanism' will be used to describe any means of heating the drain electron reservoir. It can be said now, however, that phonon-mediated heat flow through the QD via e-ph coupling will play a dominant role in explaining $\Delta T_{\rm D}$. Utilizing this will ultimately allow the e-ph coupling strength to be studied.

This unexpectedly high drain electron temperature motivated this research to find a heating mechanism capable of explaining the measurements. To that end, I

will use a pair of coupled, diffusive heat equations to simulate the nanowire system. These simulations will then be used to replicate the experimental temperatures by varying the unknown material properties. Before applying such equations to the HNW system, however, it is instructive to first understand the dynamics of heat flow under this model. while discussing the governing equations, I will show that there are two specific coefficients, later called λ and δ, that control how a system is coupled. It is the dynamics controlled by these coefficients that will ultimately allow my simulations to be matched with measurements.

7.2. Governing equations for a coupled electron-phonon system

In this section I will go over the diffusive equations that describe heat flow through a coupled electron-phonon system. These equations are valid for systems with sizes, L, longer than the mean free path (MFP), l, of either the electrons and phonons, $l_e, l_{ph} \ll L$.

7.2.1. Electron-phonon coupling equations

The electron and phonon temperatures in the two systems are approximated by two diffusive coupled heat equations and charge conservation.

$$-\vec{\nabla} \cdot \left(\kappa_e \vec{\nabla} T_e \right) = Q_{\text{J.H.}} - \Gamma \left(T_e^n - T_p^n \right) \tag{7.1}$$

$$-\vec{\nabla} \cdot \left(\kappa_p \vec{\nabla} T_p \right) = \Gamma \left(T_e^n - T_p^n \right) \tag{7.2}$$

$$\vec{\nabla} \cdot \vec{J} = 0 \tag{7.3}$$

Here $T_{(e,p)}$ and $\kappa_{(e,p)}$ are the electron and phonon temperatures and thermal conductivities, respectively, $Q_{\text{J.H.}} = \vec{J} \cdot \vec{E}$ represents Joule heat in the system, Γ and

n are constants that characterize the e-ph interaction, and $\vec{J}$ is the electric current density. The symmetric power law form for the e-ph interaction term, $\Gamma(T_e^n - T_p^n)$, is based on common experimental and theoretical accounts for e-ph interaction, [71–73]. Both parameters characterizing the e-ph interaction, Γ and n, are dependent on the dimensionality of the system, as well as the electron and phonon transport properties. For example, $n = 5$ for screened piezoelectric scattering, while for screened, deformation potential scattering $n = 7$ [72]. Recall that it is e-ph interaction that will be of interest here. As such, the goal of this chapter will be to determine Γ and n.

To more accurately approximate the electron and phonon systems, I include the temperature dependencies of their thermal conductivities. For the nanowire, the phonon thermal conductivity is modeled using a simple power law formula following that of the Debye model,

$$\kappa_p = C_p T_p^{n_p} \tag{7.4}$$

where C_p and n_p are constants. The electronic thermal conductivity or conductance, κ_e or K_e, for all materials is modeled using the Wiedemann-Franz law, [42, 44],

$$\begin{aligned} \kappa_e &= L_o \sigma T_e \qquad && d \geq 2 \\ K_e &= L_o G_e T_e \qquad && d = 1 \end{aligned} \tag{7.5}$$

where

$$L_o = \frac{\pi^2}{3}\left(\frac{k_B}{e}\right)^2 = 2.44 \times 10^{-8}\ \mathrm{W\Omega K^{-2}}\,, \tag{7.6}$$

d is the dimensionality of the electrons, and σ and G_e are the electrical conductivity and conductance, respectively, both of which can be temperature dependent.

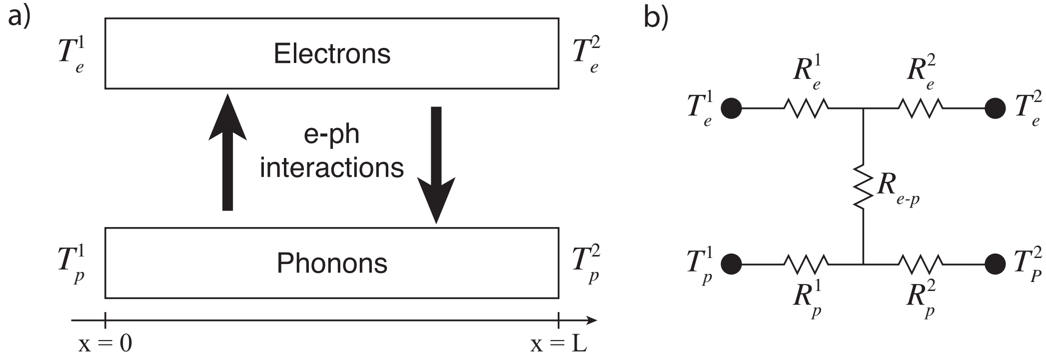

FIGURE 7.3. Two schematics of the heat flow through a rod connected to two thermal reservoirs. In the reservoirs, the temperatures of the electrons and phonon need not be the same. (a) A schematic of the rod viewed as two separate systems, one electron and one phonon. Throughout the rod's length, the electrons and phonon can exchange heat through collisions. (b) An equivalent thermal circuit diagram of the rod showing the paths heat can take between the reservoirs. The magnitude of the various thermal resistances, $R_{(e,p)}^{(1,2)}$ and R_{e-p}, dictate how heat will flow through the system.

7.2.2. High level analysis of the electron-phonon coupling equations

Recall that our goal with analyzing the coupled equation analytically is to derive the controlling coefficients λ and δ. As I will show here, λ controls the equilibrium temperature that the electron and phonon temperatures tend towards as they become coupled.

There are two regimes in Eqs. (7.1) and (7.2) where we can solve the system exactly, a fully decoupled system where $\Gamma \to 0$, and a fully coupled system where $\Gamma \to \infty$. The term 'coupled' here refers to how independent the electron and phonon temperatures are. In the decoupled case the two temperatures are completely independent, whereas in the coupled case they are equal. To begin analyzing the coupled equations, I will first consider a 1D rod, and assume that $Q_{J.H.} = 0$; the derived results can easily be generalized. A diagram of the modeled system and its boundary conditions, along with an equivalent thermal circuit, are shown in Fig. 7.3.

For the decoupled case, setting $\Gamma = 0$ yields two standard diffusive heat equations, one equation each for electron and phonon systems. The solutions in this case are trivial, and easily solved using standard methods for ordinary differential equations.

For cases where $\Gamma \neq 0$, Eqs. 7.1 and 7.2 represent two coupled non-linear partial differential equations. The general solution to this pair of equations is not analytically tractable, and must be solved numerically. In the fully coupled case, however, the system simplifies to a point where an analytic solution is at least possible. To that end, I first rewrite Eqs. (7.1) and (7.2) in terms of the thermal heat fluxes of the electron and phonon systems:

$$\vec{\nabla} \cdot \vec{\phi}_e = -\Gamma \left(T_e^n - T_p^n \right)$$
$$\vec{\nabla} \cdot \vec{\phi}_p = \Gamma \left(T_e^n - T_p^n \right) ,$$

where the heat flux is defined as,

$$\vec{\phi}_{(e,p)} \equiv -\kappa_{(e,p)} \vec{\nabla} T_{(e,p)} . \tag{7.7}$$

Adding these equations together gives

$$\vec{\nabla} \cdot \vec{\phi}_{eff} = 0 , \tag{7.8}$$

where

$$\begin{aligned} \vec{\phi}_{eff} &= \vec{\phi}_e + \vec{\phi}_p , \\ &= -\kappa_{eff} \vec{\nabla} T_{eff} . \end{aligned} \tag{7.9}$$

Here $T_{eff} = T_e = T_p$ is the effective temperature, and $\kappa_{eff} = \kappa_e + \kappa_p$ is the effective thermal conductivity. Eq. (7.8) shows, as we would expect, that heat exchange between the electron and phonon systems does not modify the net heat flow in the system as a whole; instead, it merely redistributes the available heat between the electron and phonon systems. Furthermore, Eq. (7.8) holds for any value of Γ. Using this fact, I can derive the effective temperature difference of the system in the fully coupled regime by evaluating the total heat flux, Eq. (7.9), as,

$$\vec{\phi}_{eff}\left(\Gamma \to \infty\right) = \vec{\phi}_e\left(\Gamma \to 0\right) + \vec{\phi}_p\left(\Gamma \to 0\right). \tag{7.10}$$

Inserting Eqs. (7.7) and (7.9) into this, and solving for the effective temperature difference across the bar gives

$$\begin{aligned} \kappa_{eff}\frac{\Delta T_{eff}}{L} &= \kappa_e\frac{\Delta T_e}{L} + \kappa_p\frac{\Delta T_p}{L} \\ \Delta T_{eff} &= \frac{T_e^2 + \lambda T_p^2}{1+\lambda} - \frac{T_e^1 + \lambda T_p^1}{1+\lambda} \\ \Delta T_{eff} &= T_{eff}^2 - T_{eff}^1\,, \end{aligned} \tag{7.11}$$

where I have defined the ratio

$$\lambda = \frac{\kappa_p}{\kappa_e}\,, \tag{7.12}$$

and the individual effective boundary temperatures, $i = \{1, 2\}$, as

$$T_{eff}^i = \frac{T_e^i + \lambda T_p^i}{1+\lambda}\,. \tag{7.13}$$

We see then that the effective boundary temperatures will tend towards the system with the higher thermal conductivity. In a material with $\lambda \ll 1$, for example,

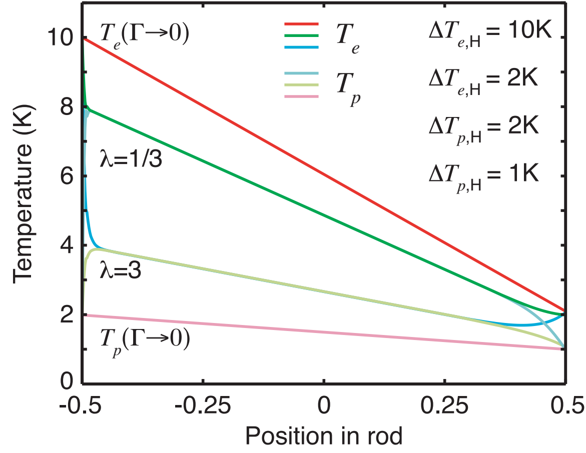

FIGURE 7.4. Simulated temperature profiles across a rod for two different λ values in the fully coupling regime. For $\lambda \ll 1$ the coupled temperature tends toward the decoupled electron temperature, $T_e(\Gamma \to 0)$, while in the opposite case, $\lambda \gg 1$, it tends toward the decoupled phonon temperature, $T_e(\Gamma \to 0)$.

ΔT_{eff} of a fully coupled system would essentially be ΔT_e. In the opposite case, $\lambda \gg 1$, ΔT_{eff} would tend toward ΔT_p. The problem of solving for the fully-coupled temperature has now been reduced to a single ordinary differential equation, Eq. (7.8), that can be solved using standard methods.

To further demonstrate the effect λ has on T_{eff}, I used COMSOL Multiphysics to model a simple 1D rod for two values of λ in the fully coupled regime. For simplicity, I assume that the thermal conductivities are independent of temperature. Figure 7.4. shows the simulation results, along with the decoupled case for comparison. As can be seen, depending on the value of λ the coupled temperature profile will lie closer to the system, electron or phonon, with the higher thermal conductivity.

To conclude this analysis, I've shown that λ strongly controls the position of the fully coupled temperature, so much so that the electron temperature at a particular point, x_o can be tuned to any value between $T_e(x_o, \Gamma = 0)$ and $T_p(x_o, \Gamma = 0)$. Due to

this control, λ will play a large role in demonstrating that the simulations can indeed be matched with experiments.

7.2.3. Analytic solution to the linearized coupled electron-phonon equations

The second parameter that I need to derive is δ. While λ controls the fully coupled temperature, δ controls whether the system is coupled or not. In combination, these to coefficients will demonstrate how the simulations can be matched to the experimental measurements.

I derive δ by solving the linearized version of Eqs. (7.1) and (7.2), that is, under the condition that $\Delta_e/T_o \ll 1$ and $\Delta_p/T_o \ll 1$. The solution to the linearized equations is given by

$$\Delta_e = A_0 + A_1 x + A_2 x^2 + A_3 \sinh(\gamma x) + A_4 \cosh(\gamma x) \tag{7.14}$$

$$\Delta_p = B_0 + B_1 x + B_2 x^2 + B_3 \sinh(\gamma x) + B_4 \cosh(\gamma x) \tag{7.15}$$

where the A_i and B_i are constants, and

$$\kappa_e(T_e) = L_0 C_e T_e^{n_e} \tag{7.16}$$

$$\kappa_p(T_p) = C_p T_p^{n_p} \tag{7.17}$$

$$\gamma = \sqrt{\Gamma n T_o^{n-1}\left(\frac{1}{L_0 C_e T_o^{n_e}} + \frac{1}{C_p T_o^{n_p}}\right)}. \tag{7.18}$$

See Appendix E for the full derivation of the linearized solution. The argument in the hyperbolic terms, γx, controls whether the system is in the coupled or decoupled regime. If I take $x = L$ to be a characteristic length along the direction of the thermal

gradient, then the argument in the hyperbolic terms,

$$\begin{aligned}\delta &= \gamma L \\ &= \sqrt{\Gamma n T_o^{n-1} L^2 \left(\frac{1}{L_0 C_e T_o^{n_e}} + \frac{1}{C_p T_o^{n_p}} \right)},\end{aligned} \tag{7.19}$$

can be considered a measure of degree of coupling. If $\delta \ll 1$ then the system is in the decoupled regime; while if $\delta \gg 1$ the system is in the coupled regime. Once the material properties have been set in Eq. (7.19), there are two parameters that can be experimentally controlled to vary the degree of coupling: the background temperature, and the size of the system.

In general, the ability of the temperature to control δ is not universal; it depends on the temperature dependence of e-ph interaction, n, and the two thermal conductivities, n_e and n_p. If $n - 1 > n_e$ or $n - 1 > n_p$, then as the temperature is increased, the system becomes more coupled. On the other hand, if $n - 1 < n_e$ and $n - 1 < n_p$, the degree of coupling will decrease with increasing temperature. Based on known power laws, the former case predominantly holds. Based on typical material constants, simulations show that electrons and phonons are essentially fully coupled at temperatures greater than $10 - 20$ K.

The second method to control the degree of coupling for a system is to change its size. Ultimately, this can be viewed as changing the system size with respect to what I define as the mean distance between electron-phonon collisions, l_{e-p}, also known as the e-ph mean free path. If I define l_{e-p} as $\delta(L = l_{e-p}) = 1$, then l_{e-p} can be written as,

$$l_{e-p} = \left(\Gamma n T_o^{n-1} \left(\frac{1}{L_0 C_e T_o^{n_e}} + \frac{1}{C_p T_o^{n_p}} \right) \right)^{-\frac{1}{2}} . \tag{7.20}$$

When the system size is much longer l_{e-p}, multiple e-ph collisions occur between the boundaries and the system approaches the coupled regime. In the opposite case, where the system size is much smaller than l_{e-p}, little to no e-ph collisions occur between when electrons and phonons enter and exit the system boundaries.

A physical way to interpret Eq. (7.19) is to consider the heat exchange rate between the electron and phonon systems, P_{e-p}, and the thermal diffusion rates of the electron and phonon systems, $P_{e-Diff.}$ and $P_{p-Diff.}$, respectively. Qualitatively, these rates can be defined as,

$$\begin{aligned} P_{e-p} &= \Gamma n T_o^{n-1} \\ P_{e-Diff} &= \frac{L_0 C_e T_o^{n_e}}{L^2} \\ P_{p-Diff} &= \frac{C_p T_o^{n_p}}{L^2}. \end{aligned}$$

Rewriting δ in terms of these pseudo heat-flow rates gives,

$$\delta^2 = P_{e-p}\left(\frac{1}{P_{e-Diff}} + \frac{1}{P_{p-Diff}}\right). \quad (7.21)$$

From here we can see that the degree of coupling is controlled by whether or not the the electron and phonon systems can diffuse heat away in their respective systems faster than the rate at which they exchange heat with each other. For the system to be considered decoupled, it is not sufficient for either the electron or phonon diffusion rate to be faster than the exchange rate; rather both must be faster. For example, if $P_{e-Diff} \ll P_{e-p}$, then the electrons and phonons will quickly exchange heat until $T_e = T_p$. At this point the system is fully coupled. Furthermore, if $P_{e-p} \ll P_{p-Diff}$, the phonon system will be able to dissipate or absorb heat from the surrounding medium to compensate for heat exchanged with the electron system,

ultimately leaving the phonon temperature remaining unchanged from the decoupled case.

This concludes the derivation of λ and δ. I have shown that, in theory, by varying these two coefficients the electron temperature at any point in a simple 1D rod can be made to have any value that lies between the decoupled electron and phonon temperatures, Fig. 7.4. As will be seen later, when applied to the HNW these same two controls will allow the electronic temperature drop across the QD to be matched to the two experimentally measured electron temperatures, ΔT_S and ΔT_D.

7.3. Heterostructure nanowire system model and heat flow mechanisms

We now finally turn our attention to the task of simulating the HNW using finite element analysis to replicate the experimentally measured temperatures. In this section I will lay out the COMSOL models used to simulate the electron and phonon temperatures in the HNW system. Due to the varying size scales in the modeled system, the HNW simulations are split into two separate simulations: the substrate simulations and nanowire simulations. The substrate simulations cover the metal leads and silicon substrate, and will provide the temperature boundary conditions for the nanowire simulations. The nanowire simulations cover the actual heterostructure nanowire. After introducing these two sub-models I'll discuss the simulations assumptions.

This section introduces the fine details of the COMSOL models themselves, however the task of listing all the parameters used in the models has been relegated to Appendix F.

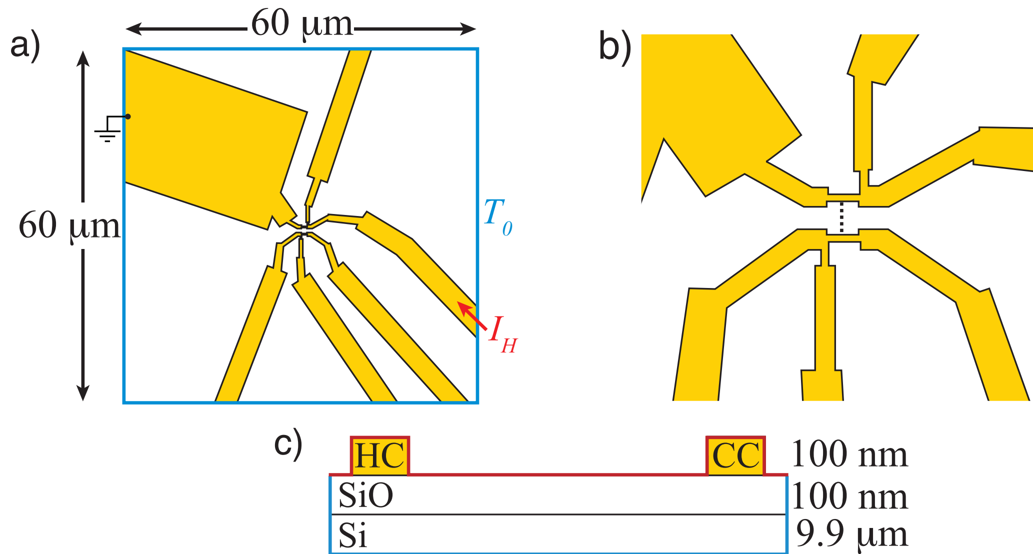

FIGURE 7.5. Schematic of the geometry created for the HNW substrate simulations. A top down view of the geometry is shown in (a). Not included in this simulation is the actual nanowire, but its location is depicted in (b) by the dashed line. The gold regions are the Au/Ni leads used to electrically connect and heat the nanowire. The heating current applied to the heating contact (HC) is applied as a DC inward current flux into the lead shown with the red arrow. The opposite side of HC is grounded. The smallest point of this channel, located in the center of (a), is the central zone where heating occurs. The cold contact (CC) is left grounded with no applied heating current. A schematic side view of the area representing the central region where the nanowire is connected is shown in (c). In both (a) and (c), blue edges represent the applied boundary temperature, T_0, and the dark red edges in (c) represent ideal insulating surfaces.

7.3.1. Model geometry of the HNW-system leads and substrate

The modeled geometry of the substrate simulations, shown in Fig. 7.5. along with the boundary conditions, were made to resemble the actual device geometry measured on by using a larger version of the SEM picture shown in Fig. 7.1. as a template. In order to properly model the temperature in the substrate and leads surrounding the nanowire, the boundary temperatures must be applied sufficiently far from the central heating zone, the center of the geometry in Fig. 7.5.a, to not adversely affect

the relevant temperature profiles and heat fluxes. The minimum required distance is the distance where the central temperature no longer changes when the distance to the boundaries increases. For the HNW substrate system, a distance of 30 μm out along the surface of the wafer, and 10 μm into the substrate were chosen based on numerous simulations.

Temperature dependent material properties are used to accurately simulate the physical system; see Appendix F for specific material values. The electronic thermal conductivity of the gold leads is found using the Wiedemann-Franz law, Eq. (7.5),

$$\kappa_e = L_0 \sigma_{Au} T_e \,,$$

while the lattice thermal conductivity is taken from a low temperature Debye model [42].

$$\kappa_{ph} = \frac{4\pi^4}{5} \nu_{\text{sound}} l_{\text{m.f.p.}} k_{\text{B}} n_A \left(\frac{T_p}{T_{Debye}} \right)^3 \tag{7.22}$$

Here T_p is the phonon temperature, ν_{sound} is the average sound velocity, $l_{\text{m.f.p.}}$ is the phonon mean free path, and n_A is the atomic density of the lattice.

The last component put into the substrate simulations is an e-ph interaction term in the gold leads.

$$Q_{\text{e-ph}} = \Gamma_{\text{Au}} \left(T_{\text{e}}^{n_{\text{Au}}} - T_{\text{p}}^{n_{\text{Au}}} \right)$$

7.3.2. Model geometry of the HNW-system nanowire

The actual and modeled geometry of the InAs heterostructure nanowire is schematically depicted in Fig. 7.6. Since the energy level spacing in the QD, $\Delta E \approx 25$ meV [59], is much greater than the thermal energy $k_B T \approx 0.1$ meV, it is expected that electrons traversing the QD do so elastically at a single QD resonant energy;

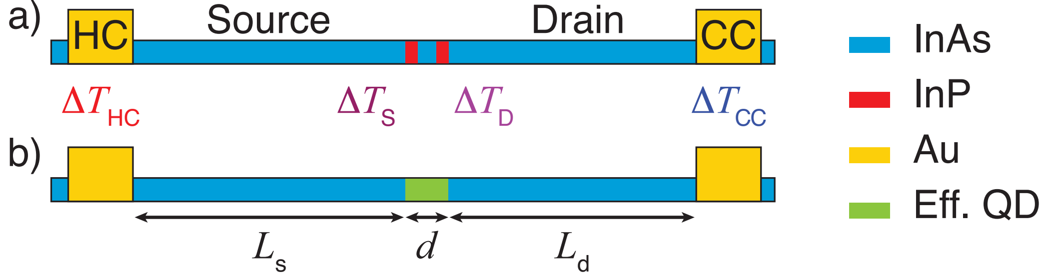

FIGURE 7.6. Schematic of the HNW (a) nanowire geometry and (b) geometry used to simulate the nanowire. In (a) actual heterostructure nanowire with the two InP barriers is depicted. In the nanowire simulations, the QD structure is modeled as a single material, with effective transport properties. The increased electron temperatures above the background temperature, T_0, are shown as four key points: in the hot and cold contacts, ΔT_{HC} and ΔT_{CC} respectively; and in the source and drain regions on either side of the QD, ΔT_S and ΔT_S respectively. The source and drain electron reservoirs are defined with respect to the applied thermal gradient. The length of the effective QD is $d = 25$ nm. The length of the source and drain sections are $L_{\mathrm{s}} = 669$ nm and $L_{\mathrm{d}} = 558.5$ nm respectively.

neither Joule heating nor e-ph interaction occurs inside the QD. The InAs nanowires grown in Lund are known to have a wurtzite crystal structure and a hexagonal cross section [13, 74]. Since the exact rotational orientation of the hexagonal nanowire, with respect to the wafer surface, is unknown, the nanowire geometry is approximated as a cylinder with a diameter of 56.9 nm and length of 1.25 μm.

The QD is really a quantum mechanical object; however, since a diffussive model is considered here, the QD structure is approximated as one effective material, Fig. 7.6.b. The electrical conductivity of the effective QD, σ_{QD} can be estimated from the measured electrical conductance of the heterostructure nanowire, G_{HNW}, and the electrical conductance of the two InAs sections, G_{InAs}.

$$\begin{aligned}\frac{1}{G_{\mathrm{HNW}}} &= \frac{1}{G_{\mathrm{InAs}}} + \frac{1}{G_{\mathrm{QD}}} \\ &= \frac{L_{\mathrm{s}} + L_{\mathrm{d}}}{\sigma_{\mathrm{InAs}} A} + \frac{d}{\sigma_{\mathrm{QD}} A} \\ \sigma_{\mathrm{QD}} &= d \left(\frac{A}{G_{\mathrm{HNW}}} - \frac{L_{\mathrm{s}} + L_{\mathrm{d}}}{\sigma_{\mathrm{InAs}}} \right)^{-1} \end{aligned} \tag{7.23}$$

Here σ_{InAs} is the electrical conductivity of the InAs portions of the nanowire, A is the nanowire cross sectional area, L_{s} and L_{d} are the lengths of the source and drain InAs sections, and d is the length of the effective QD. This calculation assumes that the active electron area covers the entire cross sectional area of the nanowire. In truth, the active electron area may be smaller than the physical size of the nanowire due to edge depletion effects. All parameters in Eq. (7.23) are known except σ_{InAs}, which is left as an input parameter for the simulations. Conductance measurements put the total conductance of the nanowire around $G_{\mathrm{HNW}} = 0.004\ (2e^2/h)$ [13], while the dimensions of the nanowire are taken from SEM pictures, Fig. 7.1.: $d = 25$ nm, $L_{\mathrm{s}} = 669$ nm, $L_{\mathrm{d}} = 558.5$ nm, and $A = \pi(28.5\ \mathrm{nm})^2 = 2.54 \times 10^{-15}\ \mathrm{m}^2$.

At this point I should note that since the QD and nanowire are low-dimensional structures, they should really be described by conductances instead of conductivities. The COMSOL simulations I use here, however, require conductivities to be entered.

Similarly, we need to also think about the effective phonon thermal conductivity. Since the majority of the QD is InAs, and InAs and InP have fairly similar lattice properties, its effective phonon thermal conductivity should be very similar to that of a pure InAs section of the same dimensions. There are two unknowns in calculating this quantity: the phononic thermal conductivity of both the InAs and InP. I can eliminate one of these parameters by assuming that the ratio, $\kappa_{\mathrm{InAs}}/\kappa_{\mathrm{InP}}$, for the nanowire is the same as for bulk. Using Eq. (7.22) to calculate the bulk ratio gives

$\kappa_{\text{InAs}}/\kappa_{\text{InP}} \approx 1.44$. Note that I have assumed here that the phonon mean free path in the two materials are essentially equivalent. To estimate the effective phonon thermal conductance of the QD, G_{Dot}, then, the structure is treated as three thermal resistors in series with each other: 5 nm InP / 15 nm InAs / 5 nm InP.

$$\begin{aligned}\frac{1}{G^{\text{p}}_{\text{Dot}}} &= \frac{1}{G^{\text{p}}_{\text{InAs}}} + \frac{1}{G^{\text{p}}_{\text{InP}}} \\ &= \frac{1}{A}\left(\frac{L_{\text{InAs}}}{\kappa_{\text{InAs}}} + \frac{L_{\text{InP}}}{\kappa_{\text{InP}}}\right) \\ &= \frac{L_{\text{Dot}}}{A\kappa_{\text{InAs}}}\left(\frac{L_{\text{InAs}}}{L_{\text{Dot}}} + \frac{L_{\text{InP}}\kappa_{\text{InAs}}}{L_{\text{Dot}}\kappa_{\text{InP}}}\right) \\ &= \frac{1}{G^{\text{Pure InAs}}_{\text{Dot}}}\left(\frac{L_{\text{InAs}}}{L_{\text{Dot}}} + \frac{L_{\text{InP}}\kappa_{\text{InAs}}}{L_{\text{Dot}}\kappa_{\text{InP}}}\right) \qquad (7.24)\end{aligned}$$

Evaluating the term in parentheses is straightforward. The lengths of the three sections are known, giving $L_{\text{InAs}} = 15$nm and $L_{\text{InP}} = 10$ nm, while the ratio of thermal conductivities was calculated above. Putting this all together gives

$$G_{\text{Dot}} \approx 0.85 G^{\text{Pure InAs}}_{\text{Dot}}. \qquad (7.25)$$

In the nanowire simulations, I assume that the phononic thermal conductance of the effective QD follows Eq. (7.25), and use κ_{InAs} as an input parameter. Physically, the effect of the QD structure for the effective QD is to have a phonon thermal conductance 15% below that of a pure InAs section of nanowire. I should also note that this approximation neglects phonon reflections at the InAs / InP interfaces.

7.3.3. Assumptions in the HNW model

7.3.3.1. Diffusive electronic heat flow

The diffusive heat equation applies to systems that are fully in the diffusive regime, that is, where the size of the material considered is much larger than the mean free path of the energy carriers, electrons and phonons. The elastic electron mean free path in InAs nanowires is around $l_e = 100$ nm [75]. Since the electron reservoirs on the side of the QD are 4 - 6 times this length, the nanowire electron system can be described reasonably well by a diffusive model over the length of the nanowire.

7.3.3.2. Diffusive phononic heat flow

For the phonons, the mean free path is dominated by surface scattering, and is therefore on the order of the smallest dimension in the material [76–78]. Here I assume that the phonon mean free path in the gold leads is equal to the film thickness, $l_{ph} \approx 100$ nm, and the nanowire diameter of 56.9 nm in the nanowire. The lengths of the systems are around 1 μm or more, which over their entirety puts them in the diffusive regime.

7.3.3.3. Neglected heat flow between the NW system, and the He^3 bath and substrate

The heat flow between the leads, substrate, and nanowire to the He^3 bath, and between the nanowire and substrate, are neglected in this model for the following reason. The majority of the nanowire is in contact with the He^3 bath. Since the He^3 bath is colder than the measured electron temperatures, it could act as significant

phononic heat sink directly to the background temperature. If this thermal sink were present and significant compared to heat diffusion through the leads, $\dot{Q}^{ph}_{Diff} \approx 100$ pW, simulations predict that the drain electron reservoir would always remain cold, which goes against measurements. The fact that the drain electron reservoir heats up implies then that the thermal boundary resistances at this interface must be large compared to the internal thermal resistances in the nanowire and leads. Note that this argument does not say that there is no heat transfer at these interfaces, only that any heat transfer is small compared to the heat fluxes through leads and nanowire. A similar argument can be made for the substrate; however, in addition to this, recent measurements show that there is indeed a significant thermal resistance between a nanowire and the substrate it rests on [79]. Ultimately these heat flows are assumed to be negligible.

7.3.3.4. Internal boundary resistances

Internal thermal boundary resistances are neglected in these simulations. It is known that making electrical contact to InAs nanowires can be touchy, and can often lead to large contact resistances [59, 75]. At this point in this chapter it is unclear whether such resistances would drastically change the heat flow dynamics of the system. In the discussion of this chapter I will revisit internal boundary resistance and consider their possible implications.

7.3.3.5. Radiative heat and thermoelectric effects

Simulation estimates of the nanowire system put the electron and phonon diffusive energy rates, as well as the e-ph heat exchange rate, in the nanowire around 10 to 100's of pW. At the temperatures measured at, a few Kelvin, the radiative heat

flux is around 10^{-26} W, so it can be neglected. With nanowire currents around tenths of a nA, Peltier effects are around few tenths of a pW, so they can be neglected as well. Lastly, the thermocurrent contribution to the electric current is irrelevant since the electric current was measured.

7.4. Heating mechanisms

I now test three hypothesized heating mechanisms capable of delivering heat to the drain side of the HNW: (i) electron diffusion through the nanowire, (ii) phonon diffusion through the substrate, and (iii) phonon mediated heat flow through the nanowire. The simulation results will show that of these three, mechanism (iii) is the only one capable of delivering enough heat to the drain electron reservoir to explain the experimental data.

7.4.1. HNW heating mechanism (i): electron diffusion through the nanowire

This heating mechanism hypothesizes the drain electrons being heated by Joule heat and electronic heat diffusion, essentially what was considered at the beginning of the chapter. In addition to typical Joule heat, this mechanism will consider the thermalization of higher energy electrons traversing the QD. This additional heating, described in more detail below, would come from an energy discrepancy between the electrons that exit the QD into the source reservoir and those electrons already in the source reservoir.

During a measurement of the drain electron temperature, electrons are driven from the drain to source. For a source electron temperature measurement, electrons are driven in the opposite direction, from source to drain [13, 59, 80]. Since the

energy levels of the QD are fixed, and are separated by intervals much larger than either $k_{\rm B}T$ or $eV_{\rm Dot}$, electrons enter and exit the QD at the same energy they entered with. For a drain measurement, each electron that exits the QD into the source reservoir will have an excess amount of energy given by $\mu_{Dot} - \mu_S$, see Fig. 7.7. inset. This excess energy will then be distributed throughout the source side of the nanowire by random collisions with either electrons or phonons. Since this is a stochastic process, the excess distributed energy can be described by a decaying exponential function directed away from the QD, with a characteristic length given by the inelastic electron mean free path. As an approximation to this exponential, I will instead assume that all of the energy is evenly distributed within the first mean free path, and that $\mu_{Dot} - \mu_S = eV_{Dot}$. The result of this will be to overestimate this effect, leading to an upper limit for the simulated ΔT_D.

The magnitude of this mechanism can determined by simulating the nanowire system with e-ph interaction turned off, $\Gamma = 0$; these results are shown in Fig. 7.7. The simulations show that almost all of the heat deposited on the source side of the nanowire will exit the nanowire through the hot contact, and a negligible amount will reach the drain electron reservoir. The reason for this is that the electronic thermal resistance towards the HC, $R^{Th}_{e,HC} = 10^4$ W^{-1}, is many orders of magnitude less than thermal resistance of the QD, $R^{Th}_{e,Dot} = 10^{13}$ W^{-1}. The small amount of heating in the drain electron reservoir is primarily due to normal Joule heating. Therefore, Ii conclude that Joule heat and electronic heat diffusion cannot deliver enough heat to the drain electron reservoir to account for the measured temperatures.

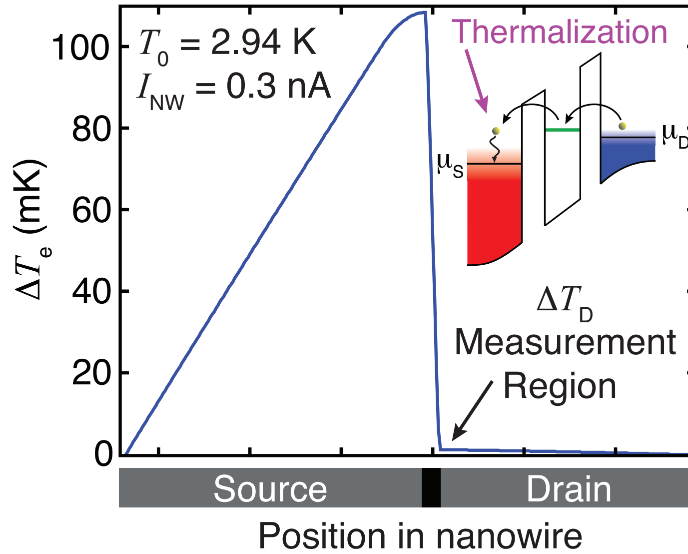

FIGURE 7.7. (Main figure) Simulated electron temperature profile along the nanowire axis due to electron diffusion and Joule heating during a measurement of the drain electron temperature. To isolate the electron diffusion effects, the boundary temperatures were set to the background temperature, and e-ph coupling was turned off. (inset) Schematic of an electron elastically traversing one of the QD's resonance energy levels. In this picture, a drain electron temperature measurement is depicted, which requires electrons to flow from drain to source by an applied voltage.

7.4.2. HNW heating mechanism (ii): phonon diffusion through the substrate

The second hypothesized heating mechanism to heat the drain electron reservoir is by phonon diffusion through the substrate between the hot and cold contacts. The flow of heat for this mechanism would start with the Joule heating of the electrons in the HC. Through e-ph interaction, a portion of this heat is given to the HC phonons. The HC phonons would then diffuse their heat to the CC through the substrate. As heat is delivered to the phonons in the cold contact, the electrons in the cold contact would also be heated through e-ph interaction, see Fig.7.8. inset. The magnitude of the cold-contact electron heating can be determined through the

substrate simulations. Recall that this simulation does not include the nanowire, so any heating in the cold contact is solely due to phonon diffusion through the substrate.

The electron temperature in the cold contact is shown in Fig. 7.8. as a function of the hot contact heating current. Though there is a small amount of electron heating in the cold contact, the magnitude is two orders of magnitude smaller than the measured drain electron measurements, and I conclude that this heating mechanism cannot explain the observed temperatures.

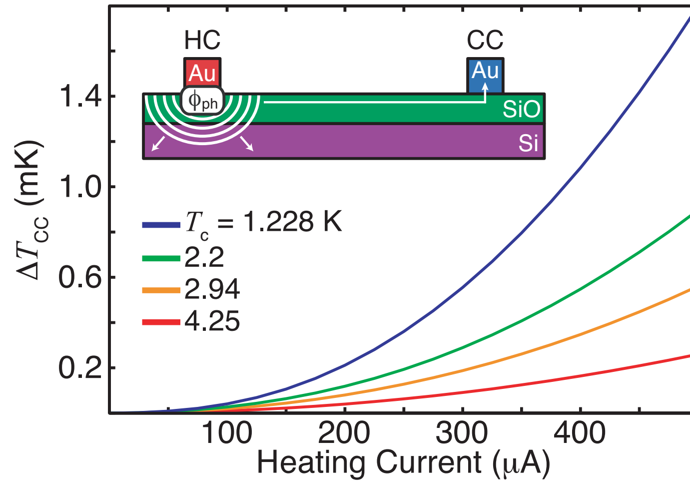

FIGURE 7.8. (Main figure) Electron heating in the cold contact due to phonon heat diffusion through the substrate. (Inset) Schematic of phonon heat diffusion through the substrate for the HNW system.

It is worth discussing this technique in the context of other researchers' methods. The mechanism here is actually a common mesoscopic heating technique used to heat electronic systems while electrically isolating them from the heating element [81]. This technique requires that the size of the device be comparable to or greater than the phonon mean free path to generate a significant electronic thermal gradient in the electronic device being studied.

In order to properly use the isolated heating technique, the Joule heat evolved in the heating contact must be much greater than that used in the HNW experiments. In addition to this, the oxide layer must be sufficiently thick so as to not lose heat to the more thermally conductive bulk silicon. In the HNW system, the maximum amount of Joule heating in the HC is around 0.6 μW. For comparison, one example of the isolated heating technique [81] generates around 100 μW, two to three orders of magnitude higher that in the HNW system. In addition to this, the thickness of the oxide layer in the HNW system is 100 nm compared to the example system's 1 μm. Both of these conditions lead to the cold contact electrons remaining cold in the HNW system. As a check to the simulation methods, I modeled a similar system to that in Ref. [81], and found simulated temperatures similar to values reported there.

7.4.3. HNW heating mechanism (iii): phonon mediated heat flow through the nanowire

We now come to the heating mechanism capable of heating the drain electrons by amounts similar to those seen in experiments. This heating mechanism focuses on the heat flow through the nanowire due the combined electron and phonon systems. The electron diffusion simulations above show that the large insulation of the QD prevents any electronic diffusion of heat between the source and drain electron reservoirs. However, Eq. (7.25) says that the QD offers little additional thermal resistance to the flow of phonons. By coupling the electron and phonon systems through e-ph interaction then, heat in the source electron reservoir can reach the drain electron reservoir by using the phonon system as a means of transportation, Fig. 7.9.

Though the e-ph coupling strength for an InAs nanowire is unknown, the qualitative effects of this heating mechanism can be still be determined by varying the

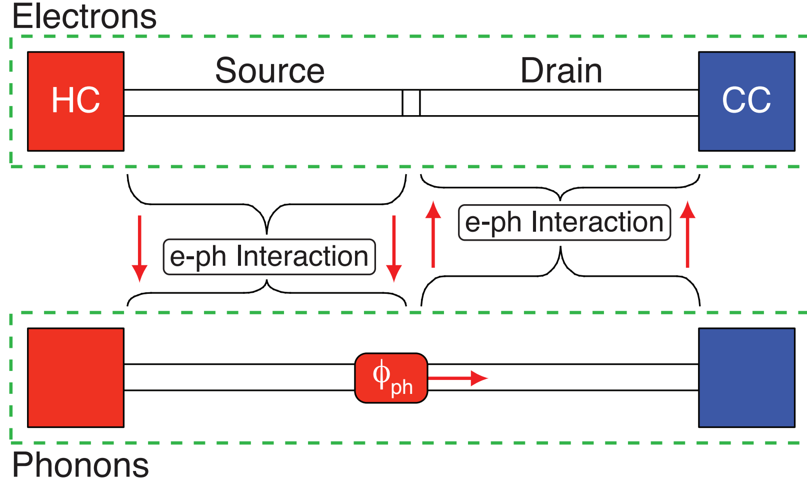

FIGURE 7.9. Flow chart showing how heat in the source electron reservoir can heat the drain electron reservoir without traversing the through the electronic system of the QD. The source electron reservoir heats up from either hot electrons in the hot contact (HC) or through Joule heating. A portion of this heat is distributed to the source phonons via e-ph collisions, which can also be heated by hot phonons from the HC. With little thermal resistance between the source and drain phonon reservoirs, the source phonons easily heat the drain phonons. The now warm drain phonons heat the colder drain electrons by a reversed e-ph interaction.

coupling strength, Γ, shown in Fig. 7.10. The simulations here include the previous two heating mechanisms: mechanism (i) can be seen as the slight increase in the source electron temperature near the QD for the decoupled case, and mechanism (ii) is inserted through the applied boundary conditions. Though there are six parameters describing the differential equations for the e-ph system, $\{C_{\mathrm{e}}, n_{\mathrm{e}}, C_{\mathrm{p}}, n_{\mathrm{p}}, \Gamma_{\mathrm{InAs}}, n_{\mathrm{InAs}}\}$, there are only two combinations of these parameters that really determine ΔT_{S} and ΔT_{D}, namely λ and δ from Eqs. (7.12) and (7.19).

$$\lambda = \frac{\kappa_p\left(T_p\right)}{\kappa_e\left(T_e\right)} = \frac{C_p T_p^{n_p}}{L_0 C_e T_e^{n_e}}$$

$$\delta = \sqrt{\Gamma n T_o^{n-1} L^2 \left(\frac{1}{L_0 C_e T_o^{n_e}} + \frac{1}{C_p T_o^{n_p}}\right)}$$

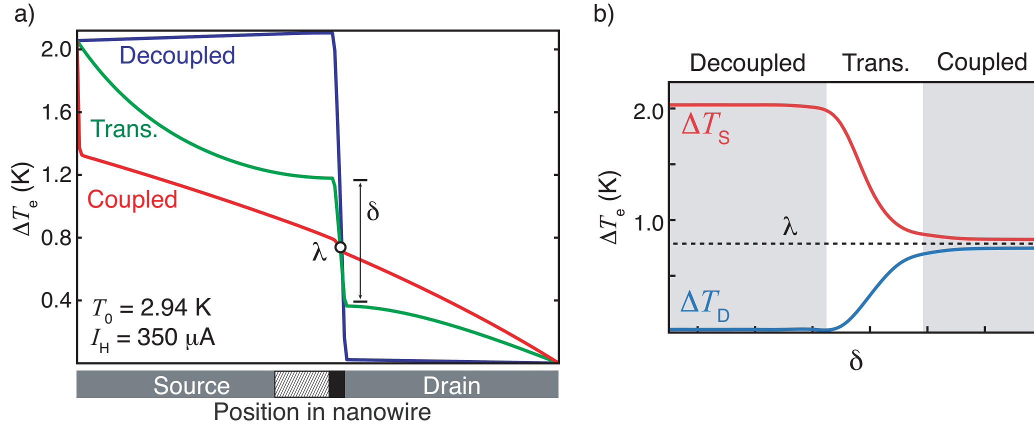

FIGURE 7.10. (a) Electron temperature profile along the nanowire axis for three coupling strengths. The degree of coupling is determined by the parameter δ, Eq. (7.19), while the fully coupled convergence point, denoted by the center circle, is determined by λ, Eq. (7.12). In the nanowire position diagram at the bottom, gray regions are the InAs sections, the hashed region is where heating mechanism (i) occurs, and the black region is the effective QD. (b) Source and drain electron temperatures near the QD as a function of coupling strength. If the system falls into either the coupled or decoupled regimes, changes in the coupling strength do little to the temperature profile. The convergence point here is denoted by the horizontal dashed line. Not shown in (a) nor (b) are the phonon temperatures for any of the coupling strengths.

As previously discussed, the value of λ determines whether the fully coupled temperature profile will lie closer to the decoupled electron or phonon temperatures, while the value of δ controls whether the system is in the decoupled or coupled regime.

At this point it is useful to define the convergence point for the HNW system. This point is the temperature that ΔT_S and ΔT_D converge towards as the coupling level, δ, is increased. In Fig. 7.10. this point is depicted at the center circle in (a) and the dashed line in (b).

The convergence point in Fig. 7.10. is for a given set of parameters such that $\lambda \approx 1$. By varying λ between $\ll 1$ and $\gg 1$, however, this point can be varied between $(\Delta T_{e,S}(\Gamma = 0) + \Delta T_{e,D}(\Gamma = 0))/2$ and $(\Delta T_{p,S}(\Gamma = 0) + \Delta T_{p,D}(\Gamma = 0))/2$, respectively.

Once the convergence point has been set by λ, the value of δ effectively controls the electron temperature drop, $\Delta T_{e,Dot} = \Delta T_{\mathrm{S}} - \Delta T_{\mathrm{D}}$, across the QD, Fig. 7.10.b. We can see now that these two parameters determine whether the drain electrons are heated or remain cold.

7.5. Preliminary fitting to experiments

At this point, the model for the HNW has been created, the material parameters needed to simulate the system are known, and λ and δ should allow flexibility to match the simulations to the experimental data. Since I an interested in determining the material parameters that describe the nanowire, one important point to cover is whether the model is even sensitive to those parameters. It could be the case that the experimental system is too near the decoupled or coupled cases depicted in Fig. 7.10.b to extract any useful information. For example, say the simulations could be matched to experiments for any $\delta > \delta_o$. In this case, trying to pick out meaningful material parameters is futile. Therefore, it is important to check that the model is in the sensitive transition region between decoupled and coupled.

Using the analysis of the three heating mechanisms, I can infer that that both λ and δ must be on the order of unity for the HNW system. If this were not the case either the drain electrons would remain cold or the electron temperature drop across the QD would be small, neither of which are seen in experiments. The logic table leading to this conclusion is shown in Fig. 7.11. This region of parameter space for λ and δ is sensitive to changes in all six input parameters, which is exactly what is desired. With this in hand, I now turn to the task of fitting the experimental data by varying the six input parameters.

λ \ δ	<<1	~1	>>1
<<1	No electron-diffusion through QD: $\Delta T_D \approx 0$	No electron-diffusion through QD: $\Delta T_D \approx 0$	No electron-diffusion through QD: $\Delta T_D \approx 0$
~1	No electron-diffusion through QD: $\Delta T_D \approx 0$		$\Delta T^{sim}_{e,Dot} = \Delta T^{sim}_{p,Dot}$ and $\Delta T^{sim}_{p,Dot} < \Delta T^{exp}_{e,Dot}$
>>1	No electron-diffusion through QD: $\Delta T_D \approx 0$	* $\Delta T^{sim}_{D} \leq \Delta T^{sim}_{p,HC}$ and $\Delta T^{sim}_{p,HC} < \Delta T^{exp}_{D}$	$\Delta T^{sim}_{e,Dot} = \Delta T^{sim}_{p,Dot}$ and $\Delta T^{sim}_{p,Dot} < \Delta T^{exp}_{e,Dot}$

* The relationship between $\Delta T^{sim}_{p,HC}$ and ΔT^{exp}_{D} is assumed to be correct

FIGURE 7.11. Logic table for the nine possibilities for λ and δ showing where the HNW system cannot be. Here $\Delta T_{Dot} = \Delta T_S - \Delta T_D$ represents the temperature drop across the QD, for either electrons or phonons. Since heat must reach the drain electrons, the insulating QD requires that the system be not be in the decoupled case, nor $\lambda \ll 1$. A fully coupled system would have small temperature drops across the QD due to the phonons thermally shorting the two QD sides, therefore the system cannot be fully coupled. Lastly, in the case of $\lambda \gg 1$ and $\delta \sim 1$, the drain electron temperature will never exceed the HC phonon temperature. As long as $\Delta T^{\text{sim}}_{\text{p,HC}} < \Delta T^{\text{exp}}_{\text{D}}$ holds true, the drain electron temperature in simulations will always be smaller than the measured drain electron temperatures.

Preliminary simulations show that by varying λ and δ through the input parameters, $\{C_{\text{e}}, n_{\text{e}}, C_{\text{p}}, n_{\text{p}}, \Gamma_{\text{InAs}}, n_{\text{InAs}}\}$, the simulated ΔT_{S} and ΔT_{D} can be matched to any single HNW experimental data point, $\Delta T^{\text{exp.}}_{\text{S}}(T_0, I_{\text{H}})$ or $\Delta T^{\text{exp.}}_{\text{D}}(T_0, I_{\text{H}})$. The larger challenge, however, is to find a single set of parameters that can reproduce the entire experimental data set for all background temperatures and heating currents, $\{\Delta T^{\text{exp.}}_{\text{S}}(T_0, I_{\text{H}}),\ \Delta T^{\text{exp.}}_{\text{D}}(T_0, I_{\text{H}})\}$. Note that having six free parameters does not amount to a 5th degree polynomial fit since it is λ and δ that ultimately control ΔT_{S} and ΔT_{D}, both of which have limiting behaviors controlled by the differential equations, Eq. (7.1) and (7.2).

7.6. Electron-phonon simulation results

In this section I will now bring in the results for the SNW system. Up to this point, a discussion about the SNW nanowire system would have been repetitive in combination with the HNW material. The key differences are that the SNW is a pure InAs nanowire, and is electrically connected to four superconducting Al leads. The measurements on this device were performed by Stefano Roddaro at the National Enterprise for nanoScience and nanotechnology, in Italy.

In tandem, I will present the results of fitting the HNW and SNW simulations to the experimental data sets. The fitting procedures will be presented first, followed by their results. Unfortunately, due to the number of free parameters, a single, complete, optimized parameter set for each system cannot be found by the method described here. What can be found, though, is relationships between pairs of parameters, as well as probable, single values for Γ and n.

7.6.1. Parameter sets

The optimization method used here is known as the Nelder-Mead algorithm, and is described in detail in Appendix H. The following details the components of the fitting procedure external to the Nelder-Mead algorithm.

The HNW parameter set is comprised of six unknown parameters: $\{C_{\mathrm{e}}$, n_{e}, C_{p}, n_{p}, Γ_{InAs}, $n_{\mathrm{InAs}}\}$. The SNW, on the other hand, has four unknowns, $\{C_{\mathrm{p}}$, n_{p}, Γ_{InAs}, $n_{\mathrm{InAs}}\}$, since two were experimentally measured, $C_{\mathrm{e}} = 8.7 \times 10^{4}\ \Omega^{-1}\ m^{-1}$ and $n_{\mathrm{e}} = 1$. This C_{e} value cannot be applied to the HNW since nanowires grown in the same batch have been known to posses different electrical conductances. Power laws, however, are commonly universal, and $n_{\mathrm{e}} = 1$ will be applied to the HNW after the optimization procedure.

For each system, one of the four background temperatures is first chosen: $T_i^{HNW} = \{1.228,\ 2.2,\ 2.94,\ 4.25\}$ K, and $T_i^{SNW} = \{0.37,\ 0.549,\ 0.6,\ 0.705\}$ K. The optimization algorithm then attempts to find a parameter set that minimizes the error between the simulated electron temperatures and the experimental temperatures for all of the experimental heating currents, $\{I_H\}$, or input powers, $\{Q_{in}\}$. For each system this entails matching the following sets:

$$\begin{aligned} \text{HNW}: \quad & \{\Delta T_{\mathrm{S}}^{\mathrm{sim.}}(T_0 = T_i, I_{\mathrm{H}}), \Delta T_{\mathrm{D}}^{\mathrm{sim.}}(T_0 = T_i, I_{\mathrm{H}})\} \text{ to} \\ & \{\Delta T_{\mathrm{S}}^{\mathrm{exp.}}(T_0 = T_i, I_{\mathrm{H}}), \Delta T_{\mathrm{D}}^{\mathrm{exp.}}(T_0 = T_i, I_{\mathrm{H}})\} \\ \text{SNW}: \quad & \{T_{\mathrm{e}}^{\mathrm{sim.}}(T_0 = T_i, Q_{\mathrm{in}})\} \text{ to } \{T_{\mathrm{e}}^{\mathrm{exp.}}(T_0 = T_i, Q_{\mathrm{in}})\} \end{aligned}$$

Each time the algorithm is run, a single parameter set is produced for the given background temperature. The error for each T_i is given by the standard deviation, $\sigma_{S.D.}(T_i)$, between simulated and experimental temperatures,

$$\sigma_{S.D.}(T_i) = \sqrt{\frac{1}{N} \sum_{I_{\mathrm{H}} \text{ or } Q_{\mathrm{in}}}^{N} (\Delta T_{error} - < \Delta T_{error} >)^2}\,, \tag{7.26}$$

where $\Delta T_{error} = T_{\mathrm{sim.}} - T_{\mathrm{exp.}}$ is an array of values corresponding to each heating current or input power, for the chosen background temperature. Upon finding an error below a set threshold, which I set to 10 mK, the algorithm returns the optimized parameter set. If this accuracy is not met, a parameter set is still returned if its error is below 0.1 K. Each optimized parameter set is then represented by a single data point in results, Figs. 7.12. and 7.13.

7.6.2. Fitting results

Though the optimization algorithm does not give unique parameter sets for either nanowire, clear relationships are seen between C_e and C_p for the HNW nanowire, and between Γ_InAs and n_InAs for both nanowires. These results are shown in Figs. 7.12. and 7.13., respectively.

7.6.2.1. Thermal conductivity coefficients

The first relationship is between C_e and C_p for the HNW system. When C_e and C_p were defined in Eqs. (7.16) and (7.17), they were assumed to be independent of temperature. In order to maintain this assumption and produce the roughly linear plot in Fig. 7.12., the two conductivity power laws must follow the equation $n_\mathrm{e} - n_\mathrm{p} = 2.3$. Noting that many power laws are universal between individual samples, using the SNW measurement of $n_\mathrm{e} = 1$ predicts a unique value for the phonon power law, $n_\mathrm{p} = -1.3$. This power law is in contrast with the positive valued power laws commonly found, in both experiments and theory, at low temperatures. We saw in Chapter III that the unit of thermal conductance is linear in temperature. When combined with the fact that the number of phonons increases with temperature, this can lead to power laws ranging from linear to cubic [82–84]. Recently, however, molecular dynamics simulations of atomically smooth nano-ribbons have predicted negative power laws in a limited range [85]. This highlights what has been said repeatedly in the literature, namely that the role of surface roughness and dimensionality are crucial in the dynamics of nanoscale phonon transport, Ref. [35, 83, 86–91].

The nanowires studied here are known to have very thin oxide surface layers, < 0.4 nm, Ref. [13, 92]. Assuming that the thin oxide layer is not uniform,

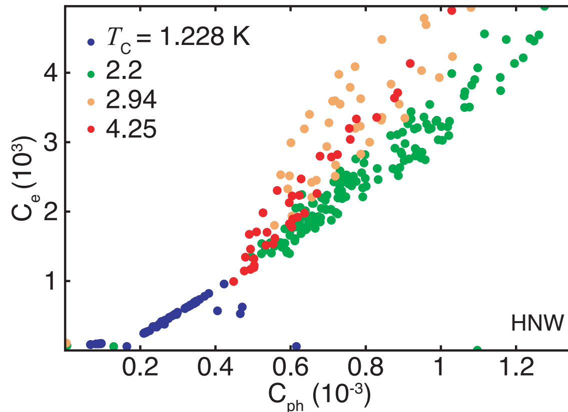

FIGURE 7.12. Relationship between C_e and C_p from the optimized HNW parameter sets. The data here predicts a λ value of about 2.2, which falls nicely into the $\lambda \sim 1$ regime predicted in Fig. 7.11.

the nanowires likely have a combination of smooth and rough surface properties. Ultimately, interpreting the $n_p = -1.3$ result here requires more information on the state of the nanowires than is currently known.

7.6.2.2. Electron-phonon coupling parameters

From the outset, the goal here was to see if these simulations could determine unique values for n_{InAs} and Γ_{InAs}. The relationships between n_{InAs} and Γ_{InAs} for each system are shown in Fig. 7.13.

Based on the fact that both nanowires are made of InAs, one would naively expect greater agreement in the two graphs in Fig. 7.13. There are two notable differences, one small and one large, between the two nanowires, other than the heterostructure. The small difference is the nanowire diameters, $D_{\mathrm{HNW}}/D_{\mathrm{SNW}} = 0.75$. There is experimental evidence on ZnO nanowires demonstrating that e-ph coupling strength decreases with decreasing nano-crystal size [93], which fits with the data trend presented here.

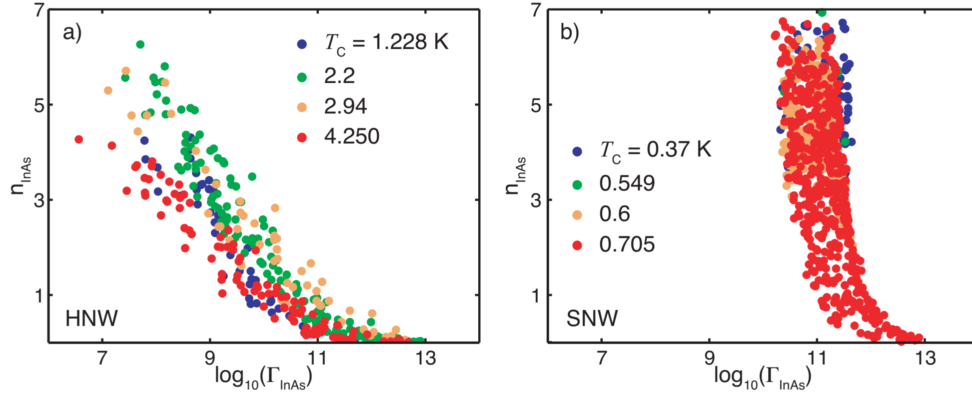

FIGURE 7.13. Relationship between n_{InAs} and Γ_{InAs} from the optimized (a) HNW and (b) SNW parameter sets.

The much larger difference lies in the charge carrier concentrations of the two systems: $n_{\mathrm{SNW}} = 1.8 \times 10^{19}$ cm^{-3}, and $n_{\mathrm{HNW}} = 2.4 \times 10^{17}$ cm^{-3}. This factor of 75 difference comes from the SNW being intentionally doped with selenium, while the HNW was not intentionally doped at all, and is remarkably close to the difference between the two data sets in Fig 7.13. Following this, we can normalize the e-ph coupling constant with the carrier density, $\Gamma_{\mathrm{InAs}}/n_{Carrier}$, and plot the two data sets together, Fig. 7.14.

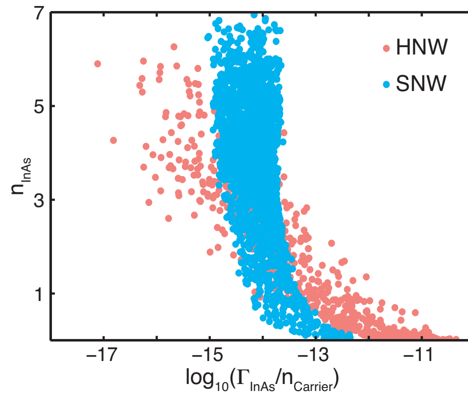

FIGURE 7.14. Relationship between n_{InAs} and carrier density normalized Γ_{InAs} for the two parameter sets.

The resulting graph is very suggestive of the different carrier concentrations being the origin of the difference between the HNW and SNW parameters sets in Fig. 7.13. If we take this at face value, it appears that an e-ph power law of $n_{\mathrm{InAs}} \approx 3$ and a carrier density dependent coupling strength of $\Gamma_{\mathrm{InAs}} \approx (10^{-14}\ \mathrm{W/carrier}) \cdot n_{Carrier}$ would explain the experimental data. To really conclude that this is the case however, a theoretical model of e-ph interaction in nanowires that predicts large coupling strengths linearly dependent on $n_{Carrier}$ is needed. At this time, we have no such model.

7.7. Revisiting the assumptions

In making the model for the HNW simulations, I assumed that the internal thermal boundary resistances of the leads and nanowire systems were negligible. Here I will discuss these resistances and comment on how they might change the system temperatures. The effects these changes would have on the system could be countered by changes in C_e, C_p, or Γ_{InAs}. Writing all of these down would become repetitive, and since it is Γ_{InAs} that I am most interested in anyway, I will only focus the changes Γ_{InAs} could accomplish. The interfaces not mentioned here were discussed in the assumptions section for HNW, page 125. For these discussions, recall that the target heat flow is into the drain electron reservoir.

7.7.1. Gold-nanowire interfaces

The first consequence of this resistance would be to decrease the amount of heat delivered to the nanowire system from the heating contact. Since the difficulty for the system lies in heating the drain electron reservoir, any removal of heat will likely lessen the amount that the drain electrons can be heated. However, there are two

thermal boundary resistances here: one electronic and one phononic. If the electronic resistance is small while the phononic resistance is large, then it is conceivable that the phonons in the nanowire would be able to deliver more of the heat gained from the source electrons to the drain electron reservoir. This effect would require smaller values for Γ_{InAs}.

7.7.2. Gold-substrate interfaces

A phonon interface resistance between the gold leads and the substrate would tend to increase the electron and phonon temperatures in the gold heating contact. Higher temperatures here would mean more heat to be distribute throughout the system, effectively increasing the temperature everywhere in the gold leads and nanowire. In regards to heating the drain electron reservoir, this would require smaller values for Γ_{InAs} to explain the measurement results. However, this resistance would also require the source electrons and phonon to shed more heat than before. In matching the measured source temperatures, this could lead to an increasing need to dissipate heat through the phonon system, which would require larger values for Γ_{InAs}.

7.7.3. InAs-InP QD interfaces

This interface resistance would block the heat in the source phonon system from reaching the drain electron reservoir. In order to maintain the same temperature increase in the drain electron reservoir then, more heat would need to be injected into the source phonon system, requiring an increased coupling strength.

7.8. Conclusion

Temperature measurements from two unique experimental systems suggested that e-ph coupling was playing a dominant role in the distribution of electronic heat. The analytic and computational results discussed here were developed in an attempt to probe e-ph coupling in InAs nanowires using these experiments as input data. In the end, these results support a phonon-mediated heat flow through the HNW system to explain the experimental data sets. Upon completion, however, it was found that too many unknowns prevented a complete parameter set from being uniquely determined. One parameter extracted was the phononic thermal conductivity power law, $n_{ph} = -1.3$, however, such a power law lacks a clear theoretical explanation, as it is counter to the more common $n_{ph} > 0$.

One curious aspect of the two parameter sets is the common factor of ~ 75 difference between the two Γ-n plots as well as the two carrier densities. Using this difference to normalize the e-ph coupling data sets leads to an approximate pair of unique coupling parameters: $n \approx 3$, and $\Gamma \approx (10^{-14}$ W/carrier$) \cdot n_{Carrier}$. Both of these results highlight the need to increase our understanding of the unknown, dominant variables controlling nanoscale heat flow.

CHAPTER VIII

CONCLUSION

8.1. Research summary

Thermoelectric research primarily strives to achieve an efficiency that would allow thermoelectric heat engines to compete with conventional mechanical technologies. Mesoscale engineering aims to achieve this goal through the tailoring of device properties, which has added renewed enthusiasm to the field. More specifically, mesoscale engineering offers greater control over the three material properties that control thermoelectric efficiency: thermopower, electrical conductivity, and thermal conductivity.

In other thermoelectric research, anisotropic materials are studied with the goal of decoupling dependencies of conflicting thermoelectric properties [15]. One such coupling is well demonstrated by the Wiedemann-Franz law, which states that the electronic thermal conductivity is proportional to the electrical conductivity. The theoretical efficiency of thermoelectric materials, Eqs. (2.31)-(2.33), however, tells us to maximize the electrical conductivity and minimize the thermal conductivity. Anisotropic thermoelectric materials offer a potential way to circumvent this dilemma by decoupling the directional dependence of the electric current from the thermal gradient. The idea would then be to create a material with high electrical conductivity along one axis, while having a low thermal conductivity along an orthogonal axis.

The first part of this dissertation focused on utilizing mesoscale engineering methods to study anisotropic thermoelectric effects. This research was conducted by experimentally confirming that a four-terminal ballistic rectifying junction can

generate transverse thermovoltages. It was shown that these junctions exhibit a transverse thermopower that is similar to the difference between two quantum point contact (QPC) thermopowers, suggesting that the junction be interpreted as a network of QPCs. This QPC network interpretation fits well with previous electronic measurements.

Through the use of a multi-terminal scattering approach, a quantitative theory was derived that details both the non-linear voltage and linear thermoelectric response of multi-terminal ballistic junctions. By applying this theory to the four-terminal junction, it was found that both the thermoelectric and non-linear voltage properties are related to energy derivative of the transmission functions within the junction. This relationship lead to the ability to extract the junction's transverse thermopower even though direct temperature measurements were not made. That said, this theory must be validated by taking direct temperature measurements for comparison. Measurements on second generation devices have been made to do just this.

Anisotropic materials were also studied in a general context. Specifically, the theoretical efficiency of an anisotropic thermoelectric material operating with the electric current orthogonal to the thermal gradient was derived. The derived efficiency shows that the transverse thermoelectric figure of merit depends on the electrical resistivity instead of the electrical conductivity. This efficiency also demonstrates that there exists the potential to enhance the transverse FOM through engineering the anisotropic transport properties of a material.

The last part of this dissertation focused on electron-phonon interaction in InAs nanowires. Nanowires constitute one nano-engineered technology studied for thermoelectric applications; however, some fundamental physics at these scales are not yet fully understood. The strength of electron-phonon interaction is one such

aspect that needs further research. Based on a diffusive transport model, the research conducted here suggests that e-ph coupling strength in InAs nanowires is linearly dependent on the carrier density. It was also found that e-ph interaction in these nanowires seems to be much stronger that theory would suggest. Finding alignment between theory and these results is actively being pursued.

8.2. Research outlook

With their highly controllable, quantum-point-contact-like characteristics, multi-terminal ballistic rectifiers represent a novel arena for the study of anisotropic thermoelectric effects. Creating a macroscopic functional 2D array of these junctions, Fig. 5.9., or possibly a 3D array, would be the ultimate extension of these devices. The primary challenge at that point would lie in their fabrication, since in order for either type of device to operate at room temperature, the individual junction size would need to be near the ballistic realm of transport. Electrically driven measurements on single junctions have already demonstrated transverse operation at room temperature [60], as well as 2D arrays at low-temperature [61]. Whether these results will translate to a transverse thermoelectric response from an array at room temperature is still unproven. In conjunction with the derived transverse thermoelectric efficiency, Eq. (6.57), these types of devices should offer ample research opportunities in nano-engineered, anisotropic thermoelectric materials.

The non-linear multi-terminal scattering theory derived here, if true, offers an interesting method to explore thermoelectric phenomena without actually applying thermal gradients. Since electrical measurements are typically much easier to perform than thermal measurements, this theory may help researchers better understand thermoelectric effects in their systems. It would also be interesting to see what a

version of the theory extended to higher orders in both voltage and thermoelectric response would lead to. Such an extension may reveal higher-order electrical responses that could be used to probe and interpret non-linear thermoelectric phenomena.

APPENDIX A

DERIVATION OF THE FIGURE OF MERIT

In this appendix I cover the mathematics behind the derivation of the thermoelectric efficiency. The derivation here starts from Eqs. (2.25) - (2.30) on page 19.

From Eqs. (2.21) and (2.25), we can write down the thermoelectric efficiency as,

$$\eta = \frac{I^2 R_L}{T_h S I + K\Delta T - \frac{1}{2} I^2 R}\,. \tag{A.1}$$

To calculate the maximum efficiency, we first define $w = R_L/R$ and insert the current I, Eq. (2.30), into Eq. (A.1). The efficiency can then be written as

$$\eta = \frac{\frac{\Delta T}{T_h} w}{1 + w - \frac{\Delta T}{2T_h} + (1+w)^2 \frac{RK}{S^2 T_h}}. \tag{A.2}$$

The last term in the denominator contains the product RK. In order to maximize η, this product needs to be minimized. From Eqs. (2.28) and (2.29), RK can be written as,

$$RK = \kappa_p \rho_p + \kappa_p \rho_n \frac{\gamma_p}{\gamma_n} + \kappa_n \rho_p \frac{\gamma_n}{\gamma_p} + \kappa_n \rho_n \tag{A.3}$$

The ratio of γ_p/γ_n, and its inverse, can also be written as the ratio of the elements' cross sectional areas A_p/A_n. Therefore by varying the cross sectional areas, we can minimize RK of any real cell through geometric means. To calculate the optimum

value, we set the derivative of RK with respect to γ_p/γ_n to zero and solve for γ_p/γ_n.

$$\frac{\partial(RK)}{\partial(\gamma_p/\gamma_n)} = 0 = \kappa_p\rho_n - \kappa_n\rho_p(\gamma_p/\gamma_n)^{-2}$$
$$\gamma_p/\gamma_n = \left(\frac{\kappa_n\rho_p}{\kappa_p\rho_n}\right)^{1/2} \tag{A.4}$$

Substituting this back into Eq. (A.3) gives the minimized RK value.

$$\begin{aligned} RK_{min} &= \kappa_p\rho_p + \kappa_p\rho_n\left(\frac{\kappa_n\rho_p}{\kappa_p\rho_n}\right)^{1/2} + \kappa_n\rho_p\left(\frac{\kappa_p\rho_n}{\kappa_n\rho_p}\right)^{1/2} + \kappa_n\rho_n \\ &= \kappa_p\rho_p + 2\left(\kappa_p\rho_p\kappa_n\rho_n\right)^{1/2} + \kappa_n\rho_n \\ &= \left(\left(\kappa_p\rho_p\right)^{1/2} + \left(\kappa_n\rho_n\right)^{1/2}\right)^2 \end{aligned} \tag{A.5}$$

Defining

$$Z = S^2/RK_{min}\,, \tag{A.6}$$

η can be written as

$$\eta = \frac{\frac{\Delta T}{T_h}w}{1 + w - \frac{\Delta T}{2T_h} + (1+w)^2/(ZT_h)}. \tag{A.7}$$

The last available experimental control is the resistance of the load resistor, which is expressed in η through $w = R_L/R$. Therefore maximizing η with respect to the load resistor amounts to maximizing it with respect to w.

$$\frac{\partial\eta}{\partial w} = 0 = \frac{\frac{\Delta T}{T_h}}{1 + w - \frac{\Delta T}{2T_h} + (1+w)^2/(ZT_h)} - \frac{\frac{\Delta T}{T_h}w\left(1 + 2(1+w)/(ZT_h)\right)}{\left(1 + w - \frac{\Delta T}{2T_h} + (1+w)^2/(ZT_h)\right)^2}$$

$$
\begin{aligned}
\frac{\Delta T}{T_h} w \left(1 + \frac{2(1+w)}{ZT_h}\right) &= \frac{\Delta T}{T_h}\left(1 + w - \frac{\Delta T}{2T_h} + \frac{(1+w)^2}{ZT_h}\right) \\
\frac{\Delta T}{T_h} w + 2\frac{\Delta T}{T_h}\frac{w(1+w)}{ZT_h} &= \frac{\Delta T}{T_h} + \frac{\Delta T}{T_h} w - \frac{1}{2}\left(\frac{\Delta T}{T_h}\right)^2 + \frac{\Delta T}{T_h}\frac{(1+w)^2}{ZT_h} \\
2\frac{\Delta T}{T_h}\frac{w(1+w)}{ZT_h} &= \frac{\Delta T}{T_h} - \frac{1}{2}\left(\frac{\Delta T}{T_h}\right)^2 + \frac{\Delta T}{T_h}\frac{(1+w)^2}{ZT_h} \\
1 - \frac{1}{2}\frac{\Delta T}{T_h} &= \frac{2w(1+w) - (1+w)^2}{ZT_h} \\
2w + 2w^2 - 1 - 2w - w^2 &= Z\left(T_h - \frac{1}{2}(T_h - T_c)\right) \\
w^2 &= 1 + Z\frac{T_h + T_c}{2} \\
w = \frac{R_L}{R} &= \sqrt{1 + Z\bar{T}} \qquad \text{(A.8)}
\end{aligned}
$$

Here $\bar{T}$ is the average temperature, and the product $Z\bar{T}$ is referred to as the thermoelectric figure of merit. The final equation for the optimum thermoelectric efficiency is obtained by replacing Z in Eq. (A.7) with w.

$$
\begin{aligned}
\eta_{max} &= \frac{\Delta T}{T_h}\frac{w}{1 + w - \frac{\Delta T}{2T_h} + (1+w)^2\bar{T}/((w^2-1)T_h)} \\
&= \frac{\Delta T}{T_h}\frac{w}{1 + w - \frac{\Delta T}{2T_h} + (1+w)^2\bar{T}/((w^2-1)T_h)}\frac{1 - 1/w}{1 - 1/w} \\
&= \frac{\Delta T}{T_h}\frac{w - 1}{w - 1/w - \frac{\Delta T}{2T_h}(1 - 1/w) + (1 + 1/w)\frac{\bar{T}}{T_h}} \\
&= \frac{\Delta T}{T_h}\frac{w - 1}{w - 1/w - \frac{\Delta T}{2T_h}(1 - 1/w) + \frac{1}{2}(1 + 1/w)\left(1 + \frac{T_c}{T_h}\right)} \\
\eta_{max} &= \eta_C\frac{\sqrt{1 + Z\bar{T}} - 1}{\sqrt{1 + Z\bar{T}} + \frac{T_c}{T_h}} \qquad \text{(A.9)}
\end{aligned}
$$

On the last line, I have identified the Carnot efficiency as $\eta_C = \Delta T/T_h$, and substituted in Eq. (A.8) for w. Written out, the figure of merit reads,

$$Z\bar{T} = \frac{S^2\bar{T}}{\left((\kappa_p\rho_p)^{1/2} + (\kappa_n\rho_n)^{1/2}\right)^2}\,. \tag{A.10}$$

APPENDIX B

FABRICATION METHODS

The devices measured on in the Antidot experiments were fabricated on layered InGaAs/InP wafers using electron beam lithography (EBL) and chemical etching, metalization, and rapid thermal annealing. These wafers contain a two-dimensional electron gas located in the InGaAs layer of the wafer, Fig B.1.a. Here I will go over the processing steps, depicted in Fig. B.1., needed to fabricate a device on this type of wafer.

The following sections describe the procedures to fabricate a structure on an InP/$Ga_{23}In_{77}As$ wafer. All of these procedures were developed at Lund University

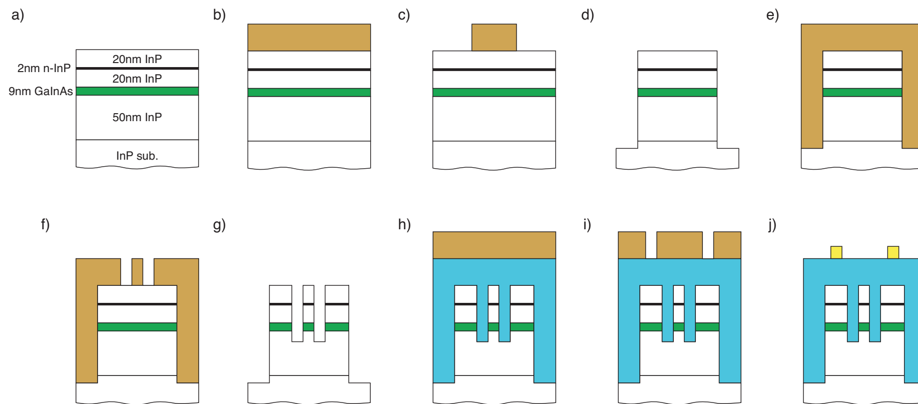

FIGURE B.1. Steps to fabricate a 2DEG device starting with a heterostructure wafer (a). The steps are as follows: (b) deposit resist layer; (c) expose and develop hall bar pattern in the resist using EBL; (d) define the hall bar by chemical etching and remove resist; (e) deposit a second resist layer; (f) expose and develop fine structures in the resist using EBL; (g) define the fine structures by chemical etching and remove resist; (h) deposit and cross-link an insulating layer of resist, after which deposit a resist layer for exposure; (i) expose and develop top gate patterns into in resist using EBL; and (j) deposit metallic film and remove resist. Not depicted here is the fabrication of contact pads, which is done between steps (d) and (e). The steps for the contact pads are identical to (h-j) without the insulating layer, and with the added step of thermal annealing.

by various graduate students and cleanroom staff. In order, the steps to creating a device are: (1) obtain a clean wafer, (2) etch out the the Hall bar, (3) create the contact pads, (4) etch the fine structures, and if needed (5) create an insulating top gate.

B.1. Wafer cleaning

1. Clean the sample in Remover 1165 for 2 - 3 minutes using ultra sonic treatment.

2. Rinse in acetone for 1 minute.

3. Rinse in IPA (isopropanol) for 1 minute.

4. Blow dry with N_2 gas.

5. Look at the wafer in an optical microscope. If the sample is still dirty redo the cleaning procedure.

B.2. Defining the Hall bar

1. Spin two layers of ZEP 520 A7 resist at a speed of 6000 RPM for 30 seconds. Bake at 160 °C for 15 minutes after each spin-on.

2. Expose in EBL.

3. Develop for 5 minutes in oxylene.

4. Rinse in IPA for 10 seconds.

5. Post bake for 5 min at 120 °C on a hotplate.

6. Etch for 2 minutes with standard etch: 5 ml HBr, 5 ml HNO_3 300 μl saturated bromic water (SBW) and 40 ml DI water.

7. Strip the resist in Remover 1165, 85 °C for 5-10 minutes. Rinse in acetone for 1 minute. Rinse in IPA for 1 minute.

B.3. Creating the contact pads

1. Spin a single layer of PMMA 950 A6 resist at 6000 RPM for 30 seconds. Bake at 160 °C for 15 minutes.
2. Expose in EBL.
3. Develop for 90 seconds in MIBK/IPA. Then rinse in IPA for 30 seconds.
4. Evaporate 400 Å Au / 200 Å Ge / 1600 Å Au onto the sample. Note: always use a fresh Ge boat to ensure good Ohmic contacts.
5. Perform lift-off in acetone for a few hours. Then use low power ultra sonic treatment for a few minutes if necessary.
6. Rinse in IPA for 1 minute.
7. Perform rapid thermal annealing: 200 °C for 60 seconds and then 390 °C for 120 seconds in H2/N2 gas.

B.4. Fine structure EBL procedure for InGaAs/InP

- Clean the sample (optional)
- Deposit resist
    1. Place the sample on a spinner and put a droplet of the positive resist ZEP 520 A7 on the surface. Make sure the drop covers the entire surface without any liquid or gas interface.

2. Spin the sample for 60 seconds at 9000 rpm.
3. Soft bake the sample on a hot plate for 10 minutes at 160 °C in a closed environment.

- EBL exposure

1. Use the exposure parameters for 'Fine Structures' in Table B.1.

- Development the pattern

1. Place the sample in oxylene for 5 minutes.
2. Rinse the sample in IPA for 10 seconds.
3. Blow dry with N_2 gas.

- Optical inspection

1. Inspect the sample with an optical microscope. If the structure looks okay then continue with the post development baking, otherwise remove the resist and start over from the beginning.

- Post development baking

1. Bake the sample on a hotplate for 2 minutes at 120 °C in a closed environment.

- Wet etching

1. Mix 60 ml DI water with 1 ml HBr, 1 ml HNO_3, and 120 μl SBW (saturated bromic water).
2. Etch the sample for 15 seconds at room temperature using plastic tweezers.
3. Rinse in DI water, bath 1, for 10 seconds.

4. Rinse under DI water, bath 2, for 10 seconds.
5. Blow dry with N_2 gas.

- Resist stripping

1. Place the sample in warm Remover 1165 heated to 80 °C using a hot plate for 5 - 10 minutes.
2. Rinse in acetone for 1 minute.
3. Rinse in IPA for 1 minute.
4. Blow dry with N_2 gas.

- Optical inspection

1. Inspect the sample in an optical microscope. If resist is still present on the surface put the sample in Remover 1165 and redo the last step.

B.5. Procedure for cross linked PMMA isolated top gate for InGaAs/InP

- Clean the sample (optional)
- Resist deposition

1. Place the sample on a spinner and put a droplet of the positive resist PMMA 950 A6 on the surface.
2. Spin the sample for 30 seconds at 6000 rpm.
3. Soft bake the sample on a hot plate for 10 minutes at 160 °C.

- EBL exposure for insulating cross-linked PMMA

1. Use the exposure parameters for 'Insulating Top Gates' in Table B.1.

- Development of insulating PMMA

  1. Place the sample in acetone for 2 minutes.
  2. Rinse in IPA for 20 seconds.
  3. Blow dry with N_2 gas.

- Optical inspection

  1. Inspect the sample with an optical microscope. If the structure looks okay, then continue with the post development baking. Otherwise, restart the fabrication procedure with a clean wafer.

- Post development baking

  1. Bake the sample on a hot plate for 15 minutes at 180 °C.

- Cleaning of sample (optional)

  1. Clean the sample in Remover 1165 for 2-3 minutes with ultra sonic treatment.
  2. Rinse the sample in acetone for 1 minute.
  3. Rinse the sample in IPA (isopropanol) for 1 minute.
  4. Blow dry with N_2 gas.

- Lift-off resist deposition

  1. Place the sample on a spinner and put a droplet of the positive resist PMMA 950 A5 or A6.

2. Spin the sample for 30 seconds at 6000 rpm.
3. Soft bake the sample on a hot plate for 10 minutes at 160 °C.

– EBL exposure of lift-off resist

1. Use the exposure parameters for 'Top Gates' in Table B.1.

– Development

1. Place the sample in MIKB/IPA for 90 seconds.
2. Rinse in IPA for 30 seconds.
3. Blow dry with N_2 gas.

– Optical inspection

1. Inspect the sample with an optical microscope. If the structure looks okay, then continue with the evaporation; otherwise remove the resist and go back to the lift-off resist deposition.

– Evaporation

1. Evaporate 50 Å Ti / 1000 Å Au on the sample.

– Lift-off

1. Place the sample in Acetone for 1-2 hours.
2. Use low power ultra sonic treatment for a few minutes if necessary.

– Optical inspection

1. Inspect the sample in an optical microscope and redo the lift-off if necessary.

B.6. Electron beam lithography parameters

TABLE B.1. Shown here are the electron beam lithography parameters used in fabricating a device on an InGaAs/InP.

Process	Resist	Aperature (μm)	Area step size (μm)	Area dose (μC/cm^2)	Line step size (μm)	Line Dose (pC/cm)
Mesa Etch	ZEP	30	0.050	90	-	-
Contact Pads	PMMA	60	0.050	300	-	-
Fine Structures	ZEP	7.5	0.010	30	0.002	150
Insulating Top Gate	PMMA	120	0.010	20,000	-	-
Top Gates	PMMA	60	0.010	250	0.002	1000

APPENDIX C

INSTRUMENTS USED

This appendix details the instruments and relevant functions used to perform the experimental measurements of this dissertation. All measurements and instruments were controlled through a LabView interface.

C.1. Stanford SRS830 dual-phase digital lock-in amplifier

A lock-in (LI) amplifier is an instrument capable of measuring the magnitude and phase of a selected frequency of an AC signal. The instrument also has the capability to out a sine wave as a driving signal. Typically, the frequency to be measured is a harmonic of the driving signal. See the operating manual for specific details on how these measurements are carried out. The following are brief descriptions of the LI functions used as described by the LI operating manual.

- **Reference signal** – The output sine wave of the LI has the following characteristics: an RMS amplitude range of 4 mV to 5V at 2 mV steps with an accuracy of 1%; a frequency range of 1 mHz to 102 kHz with a 4 1/2 digit resolution; and any phase at 0.01° steps. The phase here is relative to an internal oscillator in the LI.

- **Input configuration {A, A-B, I(10^6),I(10^8)}**– Each LI has two inputs, A and B, that can be in for four different measurement configurations: {A, A-B, I(10^6),I(10^8)}. The 'A' setting measures the signal at input A. The 'A-B' setting instructs the LI to measure the voltage difference between the two inputs. In these voltage configurations the two input channels have an input impedance of

10 MΩ. The final two settings, I(10^6) and I(10^8), set the A input to a virtual ground through a 1 kΩ resistor. The voltage drop across the 1 kΩ then gives the current through the circuit.

– **Magnitude and phase measurement**$\{X, Y, R, \theta\}$– For all measurement configurations, the LI determines both the X and Y component, and thus the magnitude and phase, of the input signal. The phase is measured relative to the reference signal.

– **Sensitivity**– The sensitivity setting sets the full scale sensitivity of the output measurement. Any measured signal with a magnitude above the sensitivity value is treated as an overload, and the output is pinned to the sensitivity value. It is important to make sure that the magnitude of the output signal does not exceed the sensitivity over the entire range of a measurement.

– **HARM**– Instructs the LI to measure the nth harmonic of the reference signal, as long as that harmonic is below 102 kHz.

– **Time constant**– The reported measurement from the LI is a running average over some length of time. That time is the set by the time constant. Note that when a setting is changed in the circuit being measured, the moment that change is made the LI still contains averaging information from the time before the change. This results in a slewing time between the change and an accurate measurement. The time to wait between the change and readout, is a function of the time constant, and slope of the notch filters (see Slope/Oct). For the output signal to slew to 99% of its final value, one must wait 5 to 10 times that time constant.

- **Slope/Oct**– At the end of the internal circuitry of the LI, the measurement relies on the measurement of a DC signal. To decrease the noise in this signal, a low-pass filter is applied just before the output. The Slope/Oct setting determines the effective slope of that low-pass filter.

- **Ref In and TTL Out**– When using multiple LIs to measure the same frequency and harmonics of that frequency, the LIs must be frequency and phase locked to each other. This is accomplished by setting the frequency of one LI and using that LI's TTL output as a reference signal all other LIs. Each LI then uses this reference signal, instead of its own internal one, to conduct its measurement. If phase measurements are to be made, it is not sufficient to set the various LIs to the desired frequency, since each LI will have its own time varying phase.

C.2. DC sources and multimeters

For the measurements performed in this dissertation, two DC sources and one digital multimeter were used to apply and measure all DC voltages. To apply DC voltages a Yokogawa 7651 Programmable DC source was used. The Yokogawa is capable of outputting a DC voltage from ±12.0000 mV to ±32.000 V. The last digit here represents the resolution. To measure DC voltages a Keithely model 2000 multimeter was used. This multimeter has three averaging settings: fast, medium, and slow. This setting controls the time spent averaging the input signal before reporting the result. For the measurements made in this dissertation the slow setting was used, which corresponds to an averaging time of roughly 167 ms.

APPENDIX D

HARMONICS IN AN AC DRIVEN NON-LINEAR DEVICE

The common resistor in electrical circuits typically follows Ohm's law, $V = IR$, where V is the voltage drop across the resistor, I is the current running through the resistor, and R is the resistance of the resistor. A circuit element following Ohm's law can be described by a single value for all voltages and currents. In reality, however, the perfect Ohmic resistor does not exist. Causes for deviations from the linear relationship are many, two examples of which are: temperature-dependent resistivities; or that the element may be made of multiple materials that interact electrically, such as a diode. A good example is the exponential current-voltage (IV) dependence of a diode [94].

$$I = I_o \left(\exp \left(eV/k_{\mathrm{B}}T \right) - 1 \right).$$

Here, I_o is a constant, e is the electron charge, k_{B} is Boltzmann's constant, and T is the temperature. In the general case, the IV relationship can be written as,

$$I = \sum_{n=1}^{\infty} G_n V^n, \tag{D.1}$$

where the G_n are constant coefficients.

When an AC voltage of frequency f and amplitude V_o is applied to an Ohmic circuit element, the frequency of the current is also f.

$$\begin{aligned} I &= G_1 V_{\mathrm{AC}} \\ &= G_1 V_o \cos(2\pi f t) \end{aligned} \tag{D.2}$$

For the general case, however, the current will have a DC component and frequencies at every harmonic interval of f.

$$\begin{aligned} I &= G_1 V_{\mathrm{AC}} + G_2 V_{\mathrm{AC}}^2 + \cdots \\ &= G_1 V_o \cos(2\pi f t) + G_2 V_o^2 \left(\cos(2\pi f t)\right)^2 + \cdots \\ &= G_1 V_o \cos(2\pi f t) + \frac{1}{2} G_2 V_o^2 \left(1 + \cos(4\pi f t)\right) + \cdots \\ &= \frac{1}{2} G_2 V_o^2 + G_1 V_o \cos(2\pi f t) + \frac{1}{2} G_2 V_o^2 \cos(4\pi f t) + \cdots \end{aligned} \tag{D.3}$$

APPENDIX E

LINEARIZED SOLUTION TO THE COUPLED DIFFUSIVE EQUATIONS

Here I go through the full derivation of the linearized solution to the coupled diffusive heat equations in Chapter 7. The solution derived here will provide a clear picture of the conditions governing whether an electron-phonon system is coupled or decoupled. The coupled diffusive equations were given in Eqs. (7.1) and (7.2), and restated here.

$$-\vec{\nabla} \cdot \left(\kappa_e \vec{\nabla} T_e \right) = Q_{J.H.} - \Gamma \left(T_e^n - T_p^n \right) \tag{E.1}$$

$$-\vec{\nabla} \cdot \left(\kappa_p \vec{\nabla} T_p \right) = \Gamma \left(T_e^n - T_p^n \right) \tag{E.2}$$

I first assume that the Joule heat generated in the system, $Q_{J.H.}$, is a constant independent of location and temperature. I also assume that the thermal conductivity of each system can be described by power laws.

$$\kappa_e(T_e) = L_0 C_e T_e^{n_e} \tag{E.3}$$

$$\kappa_p(T_p) = C_p T_p^{n_p} \tag{E.4}$$

The constant coefficients, C_e and C_p, and power laws, n_e and n_p, characterize the two thermal conductivities. Assuming the Wiedemann-Franz law holds, that is if $n_\mathrm{e} = 1$, then C_e would represent a temperature-independent electrical conductivity.

My intent here is to linearize Eqs. (7.1) and (7.2) to make them analytically tractable. I start by inserting the electron thermal conductivity equation into

Eq. (7.1).

$$
\begin{aligned}
-\vec{\nabla} \cdot \left(L_0 C_e T_e^{n_e} \vec{\nabla} T_e \right) &= Q_{J.H.} - \Gamma \left(T_e^n - T_p^n \right) \\
-\vec{\nabla} \cdot \left(\frac{L_0 C_e}{n_e + 1} \vec{\nabla} \left(T_e^{n_e+1} \right) \right) &= Q_{J.H.} - \Gamma \left(T_e^n - T_p^n \right)
\end{aligned} \tag{E.5}
$$

Similarly for the phonon equation, Eq. (7.2),

$$
\begin{aligned}
-\vec{\nabla} \cdot \left(C_p T_p^{n_p} \vec{\nabla} T_p \right) &= \Gamma \left(T_e^n - T_p^n \right) \\
-\vec{\nabla} \cdot \left(\frac{C_p}{n_p + 1} \vec{\nabla} \left(T_p^{n_p+1} \right) \right) &= \Gamma \left(T_e^n - T_p^n \right) .
\end{aligned} \tag{E.6}
$$

To linearize the two equations, the temperatures are expanded about a background temperature, T_o. Making the change of variables

$$
T_{(e,p)} = T_o + \Delta_{(e,p)},
$$

where $\Delta_{(e,p)}$ are the temperature rises above the background temperature, and expanding all power laws to linear order,

$$
\begin{aligned}
T_{(e,p)}^m &= \left(T_o + \Delta_{(e,p)} \right)^m \\
&= T_o^m \left(1 + \frac{\Delta_{(e,p)}}{T_o} \right)^m \\
&\approx T_o^m \left(1 + m \frac{\Delta_{(e,p)}}{T_o} \right) \\
&\approx T_o^m + m T_o^{m-1} \Delta_{(e,p)}
\end{aligned}
$$

leads to two linearized heat equations.

$$
\begin{aligned}
-\vec{\nabla} \cdot \left(\frac{L_0 C_e}{n_e + 1} \vec{\nabla} \left(T_e^{n_e+1} \right) \right) &= Q_{J.H.} - \Gamma \left(T_e^n - T_p^n \right) \\
\frac{L_0 C_e}{n_e + 1} \nabla^2 \left(T_o^{n_e+1} + (n_e + 1) T_o^{n_e} \Delta_e \right) &= Q_{J.H.} - \Gamma \left(T_o^n + n T_o^{n-1} \Delta_e \right. \\
&\quad \left. - T_o^n - n T_o^{n-1} \Delta_p \right) \\
L_0 C_e T_o^{n_e} \nabla^2 \Delta_e &= Q_{J.H.} - \Gamma n T_o^{n-1} \left(\Delta_e - \Delta_p \right) \\
A_e \nabla^2 \Delta_e &= Q_{J.H.} - F \left(\Delta_e - \Delta_p \right) \qquad \text{(E.7)}
\end{aligned}
$$

Similarly, the same expansion for the the phonon system gives,

$$
A_p \nabla^2 \Delta_p = F \left(\Delta_e - \Delta_p \right) . \qquad \text{(E.8)}
$$

Here I have defined the effective heat conductivities

$$
\begin{aligned}
A_{\mathrm{e}} &= L_0 C_{\mathrm{e}} T_o^{n_{\mathrm{e}}} , \\
A_{\mathrm{p}} &= C_{\mathrm{p}} T_o^{n_{\mathrm{p}}} ,
\end{aligned}
$$

and the effective coupling constant

$$
F = \Gamma n T_o^{n-1} , \qquad \text{(E.9)}
$$

all of which are constants independent of temperature. Around a few Kelvin, these equations will hold for temperature rises no more than roughly 5% of the background temperature, $\Delta_e / T_o < 0.05$.

To solve Eqs. (E.7) and (E.8) I assume a power law series for $\Delta_{(e,p)}$ and solve for the constant coefficients, a_m and b_m.

$$\Delta_e = \sum_{m=0} a_m x^m$$

$$\Delta_p = \sum_{m=0} b_m x^m$$

Inserting the power series into Eqs. (E.7) and (E.8) yields the following recursion relations for a_m and b_m.

$$a_2 = \frac{1}{2A_e}\left[F\left(a_0 - b_0\right) - Q_{J.H.}\right] \tag{E.10}$$

$$b_2 = -\frac{1}{2A_p}F\left(a_0 - b_0\right) \tag{E.11}$$

$$a_{m+2} = \frac{F}{A_e(m+2)(m+1)}\left(a_m + b_m\right) \quad m \geq 1 \tag{E.12}$$

$$b_{m+2} = -\frac{A_e}{A_p}a_{m+2} \quad m \geq 1 \tag{E.13}$$

The solution for the a_m to these relations are,

$$a_m = \begin{cases} \frac{1}{m!}\left(1+\frac{A_e}{A_p}\right)^{\frac{1}{2}(m-3)}\left(\frac{F}{A_e}\right)^{\frac{1}{2}(m-1)}\left(a_1 - b_1\right) & m = \text{odd} \geq 3 \\ \left.\begin{array}{c} \frac{1}{m!}\left(1+\frac{A_e}{A_p}\right)^{\frac{m}{2}-1}\left(\frac{F}{A_e}\right)^{\frac{m}{2}}\left(a_0 - b_0\right) - \\ \frac{1}{m!}\left(1+\frac{A_e}{A_p}\right)^{\frac{m}{2}-2}\left(\frac{F}{A_e}\right)^{\frac{m}{2}-1}\frac{Q_{J.H.}}{A_e} \end{array}\right\} & m = \text{even} \geq 4 \end{cases} \tag{E.14}$$

Putting a_m into the power series for Δ_e and simplifying gives the electron temperature solution to the linearized coupled heat equation.

$$\Delta_e = A_0 + A_1 x + A_2 x^2 + A_3 \sinh(\gamma x) + A_4 \cosh(\gamma x) \tag{E.15}$$

$$\gamma = \sqrt{F\left(\frac{1}{A_e} + \frac{1}{A_p}\right)} \tag{E.16}$$

$$A_0 = a_0 - (a_0 - b_0)\left(1 + \frac{A_e}{A_p}\right)^{-1} + \frac{Q_{J.H.}}{A_e}\left(1 + \frac{A_e}{A_p}\right)^{-1}\gamma^{-2} \tag{E.17}$$

$$A_1 = a_1 - (a_1 - b_1)\left(1 + \frac{A_e}{A_p}\right)^{-1} \tag{E.18}$$

$$A_2 = -\frac{Q_{J.H.}}{2A_e}\left[1 - \left(1 + \frac{A_e}{A_p}\right)^{-1}\right] \tag{E.19}$$

$$A_3 = (a_1 - b_1)\left(1 + \frac{A_e}{A_p}\right)^{-1}\gamma^{-1} \tag{E.20}$$

$$A_4 = \left(1 + \frac{A_e}{A_p}\right)^{-1}\left[a_0 - b_0 - \frac{Q_{J.H.}}{A_e}\gamma^{-2}\right] \tag{E.21}$$

Similarly, using Eq. (E.13) to calculate the b_m, the solution for the phonon temperature, Δ_p, is,

$$\Delta_p = B_0 + B_1 x + B_2 x^2 + B_3 \sinh(\gamma x) + B_4 \cosh(\gamma x) \tag{E.22}$$

$$B_0 = b_0 + (a_0 - b_0)\left(1 + \frac{A_p}{A_e}\right)^{-1} - \frac{Q_{J.H.}}{A_e}\left(1 + \frac{A_p}{A_e}\right)^{-1}\gamma^{-2} \tag{E.23}$$

$$B_1 = b_1 + (a_1 - b_1)\left(1 + \frac{A_p}{A_e}\right)^{-1} \tag{E.24}$$

$$B_2 = -\frac{Q_{J.H.}}{2A_e}\left(1 + \frac{A_p}{A_e}\right)^{-1} \tag{E.25}$$

$$B_3 = -(a_1 - b_1)\left(1 + \frac{A_p}{A_e}\right)^{-1}\gamma^{-1} \tag{E.26}$$

$$B_4 = -\left(1 + \frac{A_p}{A_e}\right)^{-1}\left[a_0 - b_0 - \frac{Q_{J.H.}}{A_e}\gamma^{-2}\right] . \tag{E.27}$$

This leaves four unknown constants, $\{a_0, a_1, b_0, b_1\}$, which can be found by applying the boundary conditions, four in total, for the electron and phonon systems.

APPENDIX F

TABULATED THERMAL PROPERTIES

F.1. Silicon and silicon oxide

In this section, the tabulated thermal properties of crystalline silicon, crystalline silicon oxide, and amorphous silicon oxide at low temperatures are given. In Tables F.1. and Table F.2. the lattice thermal conductivities of silicon and silicon oxide are given.

TABLE F.1. Thermal conductivity as a function of phonon temperature, T_p, for crystalline silicon. Data taken from Ref. [95].

T_p (K)	κ (Wm^{-1}K^{-1})	T_p (K)	κ (Wm^{-1}K^{-1})
0	0	5	527
1	6.93	6	823
2	45.4	7	1170
3	138	8	1550
4	297	9	1950

TABLE F.2. Thermal conductivity for crystalline, $\kappa^{crys.}$, and amorphous, $\kappa^{amorph.}$, silicon oxide as a function of phonon temperature, T_p. The crystalline data here is the weighted average of the c-perpendicular and c-parallel thermal conductivities, $\kappa_{eff}^{crys.} = (1/3)\kappa_{c-perp} + (2/3)\kappa_{c-para}$, taken from Ref. [95]. The amorphous data is from Ref. [86].

T_p (K)	$\kappa^{crys.}$ (Wm^{-1}K^{-1})		T_p (K)	$\kappa^{amorph.}$ (Wm^{-1}K^{-1})
0	0		0.2	1.1×10^{-3}
1	4.067		0.5	6.1×10^{-3}
5	333		1	2.0×10^{-2}
7	740		2	5.7×10^{-2}
8	977		5	1.2×10^{-2}
9	1167		10	1.4×10^{-1}

F.2. Gold

F.2.1. Electronic thermal conductivity

The effective electrical conductivity of the Au leads for the HNW simulations was measured on a separate four-terminal structure and found to be $\sigma_{Au} = 4.05 \times 10^7$ $\Omega^{-1}\text{m}^{-1}$ and independent of temperature below 10 K.

F.2.2. Phononic thermal conductivity

For the lattice thermal conductivity of gold the relevant parameters are: $\nu_{\text{sound}} =$ 1949 m/s and $n_A = 5.959 \times 10^{28}$ atoms/m^3 are taken from Ref. [96], and $T_{Debye}(T_e)$ is taken from Ref. [97]. See Table F.3. for the tabulated values of $T_{Debye}(T_e)$.

TABLE F.3. Debye temperature of gold as a function of phonon temperature, T_p. Data taken from Ref. [97].

T_p (K)	T_{Debye} (K)	T_p (K)	T_{Debye} (K)
0	161.8	5	165.9
0.2	161.82	6	166.4
1	162.1	7	166.7
2	162.9	8	166.7
3	163.9	9	166.5
4	165.1		

F.2.3. Electron-phonon coupling parameters

The e-ph coupling parameters used for gold are averaged from Refs. [98] and [99]: $\Gamma_{\text{Au}} = 1.8 \times 10^9$ Wm^{-3}K^{-5}, and $n_{\text{Au}} = 5$.

F.3. InAs and InP lattice parameters

TABLE F.4. Lattice properties of InAs and InP: ν_{sound} is the sound velocity, n_A is the atomic density, and T_{Debye} is the Debye temperature. All values here were taken from Ref [100], except the Debye temperature for InP, which was taken from Ref [101].

	InAs	InP
ν_{sound} (m/s)	2934	3683
n_A (atoms/m^3)	1.8×10^{28}	1.98×10^{28}
$T_{\text{Debye}}(T_p$=0) (K)	255	321

APPENDIX G

INAS NANOWIRE SYSTEM WITH SUPERCONDUCTING LEADS

The experimental system described here uses a nanowire that is completely made of single-crystal InAs. The nanowire is connected to four superconducting Al leads, and as such will be referred to as the nanowire with superconducting leads (SNW). This nanowire is used in Chapter 7 in conjunction with the HNW to probe electron-phonon coupling in InAs nanowires.

G.1. Experiments on InAs Nanowire with superconducting leads

In the SNW system, the 2.8 μm nanowire is made solely of InAs, and has a diameter of roughly 80 nm. The nanowire rests on an undoped silicon substrate with a 500 nm thick silicon oxide layer. The superconducting leads are comprised of 10 nm Ti / 90 nm Al. An SEM and schematic of the SNW system is shown in Fig. G.1. (a) and (b).

Joule heat is generated in the nanowire by passing a current through the two injector leads, $I1$ and $I2$. The two superconducting probe leads, $P1$ and $P2$, are then used to measure the electron temperature by means of the proximity effect [102]. The measured temperatures as a function of heating power are shown in Fig. G.1.c, and were performed by the Italian research group lead by Stefano Rodarro. In addition to the electron temperature, Rodarro's group found the carrier concentration and mobility to be $n_{\text{carrier}} = 1.8 \pm 0.8 \times 10^{19}$ cm^{-3} and $\mu = 300 \pm 100$ cm^2/Vs, respectively, Ref [102], which gives an electrical conductivity of $\sigma = e\mu n_{\text{carrier}} = 8.7 \times 10^4$ Ω^{-1} m^{-1}. They also found that σ was essentially independent of temperature over the measured temperature range.

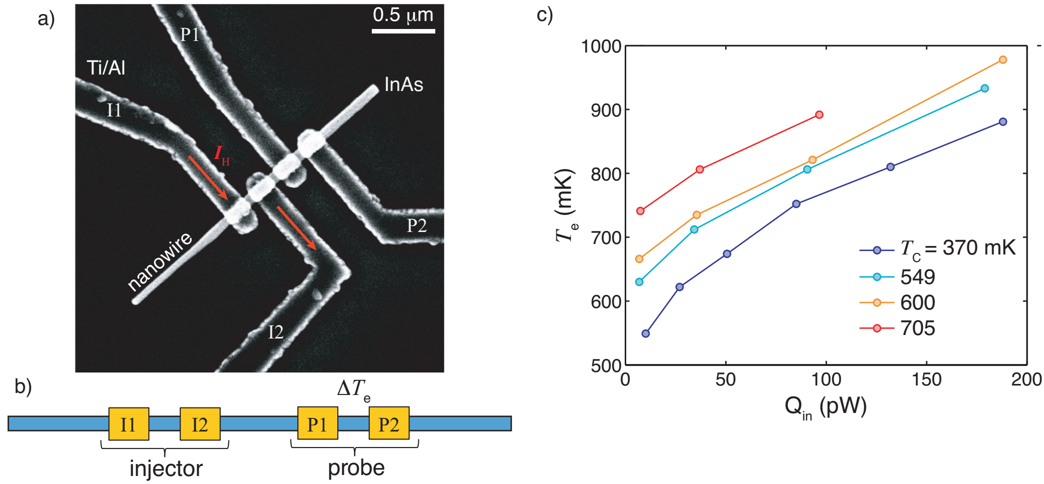

FIGURE G.1. (a) SEM of the InAs nanowire connected to superconducting Al leads. Joule heat is evolved in the nanowire under and between the two injector leads, $I1$ and $I2$, by passing a current through $I1$ and $I2$. (b) Schematic of the nanowire and the two pairs of superconducting leads. (c) Measured electron temperatures as a function of input power for background temperatures of 370, 549, 600, and 705 mK.

G.2. Model of the InAs nanowire with superconducting leads

In this section I will quickly go over the COMSOL model for the SNW system, with the intention of investigating the e-ph interaction strength in an InAs nanowire. Since the two systems are similar, most of the heating phenomena and assumptions in this system were covered in the HNW model discussed in Chapter 7, and will not be restated here.

G.2.1. Model geometry and the parameter set for the SNW-system

A 3D and top down view of the SNW simulation geometry are shown in Fig. G.2. The power delivered to the nanowire is assumed to be evenly distributed between the sections of nanowire beneath and between the injector leads, depicted as the hashed region in Fig. G.2.b. Through larger model geometries than that shown in Fig. G.2., it was found that the substrate and most of the leads were unnecessary for the SNW

simulations. Even for the largest injection powers, the purple faces identified in Fig. G.2.a, remained at the background temperature.

Since the electrical conductivity of the SNW nanowire was measured as a function of temperature, there are only four unknown parameters for the SNW system: $\{C_\mathrm{p}$, n_p, Γ_InAs, $n_\mathrm{InAs}\}$. By varying these parameters, the average simulated electron temperature under and between the probes can be matched to the experimental temperatures. Like the HNW parameter set, the goal here is to find a single parameter set that can reproduce the entire experimental data set, $\{T_\mathrm{e}^\mathrm{exp.}(T_0, Q_\mathrm{in})\}$.

G.2.2. Andreev reflections and electron heat loss in the SNW model

In addition to the assumptions made in the HNW, the SNW simulations assume that there is no electronic heat flowing from the nanowire to the superconducting leads. It is well known that the electronic thermal conductivity of a superconductor decreases to zero below the critical temperature [103, 104]. Such decreases in the electronic thermal conductivity, in conjunction with Andreev reflections [105], prevent the electron system from having a low-resistance thermal path to dissipate heat through. As such, the primary method for electrons to dissipate heat is through e-ph interaction. The phonon system can then easily dissipate this heat either through the Al leads or to the substrate. Like the HNW system, the prominent role of e-ph interaction makes the SNW system a good candidate to probe the e-ph interaction strength in InAs nanowires.

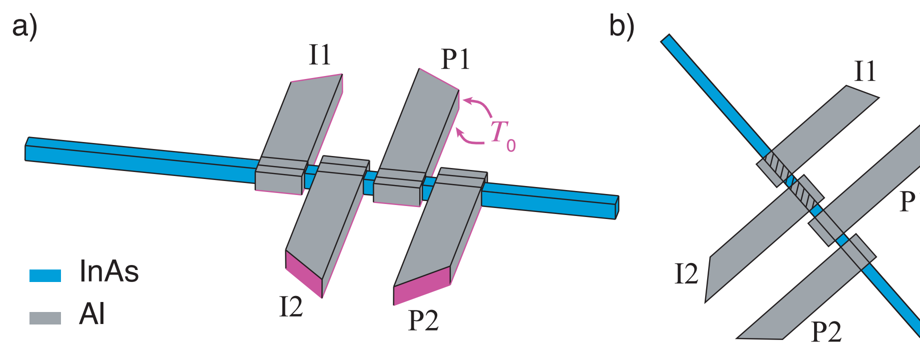

FIGURE G.2. COMSOL geometry for the SNW simulations. (a) The phonon boundary temperatures set to T_0 are the substrate-Al interfaces and the ends of all four Al leads. The hashed region in (b) represents the region in the nanowire where Joule heat is evolved; Joule heat is not evolved in the superconducting aluminum leads nor the rest of the nanowire.

APPENDIX H

NELDER-MEAD OPTIMIZATION METHOD

The Nelder-Mead optimization algorithm is a simplex method to find the minimum of a function of many variables first proposed in 1965, Ref [106]. A simplex is the generalization of closed geometrical objects with n+1 vertices in n-dimensional space. Examples in 2D and 3D are triangles and tetrahedra, respectively.

If a n-dimensional function f of the vector variable $\vec{x}$, where $\vec{x}$ has n components, needs to minimized, the Nelder-Mead method finds a minimum value through the following algorithm.

1. Evaluate the function values at the simplex vertices, and order them from best to worst. The terms 'best' and 'worst' here are subjective to the given problem.

$$f(\vec{x}_1) \leq f(\vec{x}_2) \leq \cdots \leq f(\vec{x}_{n+1}) \tag{H.1}$$

   The subscript here denotes the vertex index.

2. Using all but the worst vertex, $f(\vec{x}_{n+1})$, calculate the center of the points.

$$\vec{x}_0 = < \vec{x}_i > \tag{H.2}$$

3. Reflect the worst vertex about $\vec{x}_0$.

$$\vec{x}_r = \vec{x}_0 + \alpha(\vec{x}_0 - \vec{x}_{n+1}) \tag{H.3}$$

   Typically α is chosen to be 1.

4. At this point there are three cases to check:

   – If $f(\vec{x}_1) \leq f(\vec{x}_r) < f(\vec{x}_n)$, then replace the old worst point with the reflected vertex: $\vec{x}_{n+1} = \vec{x}_r$.

   – If $f(\vec{x}_r) < f(\vec{x}_1)$, then continue along this trajectory and replace the worst vertex: $\vec{x}_{n+1} = \vec{x}_e$.

$$\vec{x}_e = \vec{x}_0 + \gamma(\vec{x}_0 - \vec{x}_{n+1}) \tag{H.4}$$

   Here $\gamma > \alpha$ and typically chosen to be 2.

   – If $f(\vec{x}_n) < f(\vec{x}_r)$, then contract along this trajectory and replace the worst vertex: $\vec{x}_{n+1} = \vec{x}_c$.

$$\vec{x}_c = \vec{x}_0 + \rho(\vec{x}_0 - \vec{x}_{n+1}) \tag{H.5}$$

   Here $\rho < \alpha$ and typically chosen to be $1/2$.

5. Finally, collapse the simplex towards the best vertex.

$$\vec{x}_i = \vec{x}_1 + \sigma\left(\vec{x}_i - \vec{x}_1\right) \tag{H.6}$$

   Here σ is the collapsing rate and should be chosen for the given problem. Typically $\sigma = 1/2$. Return to step 1.

The NM method is not a foolproof method to optimize a function. If the simplex falls into a very flat region in f, the simplex can collapse in on itself before it reaches the optimum value. As a simplex collapses, the step size along at least one of the n-variable directions can become infinitesimally small, leading to infinitely long computation times. In addition to the simplex collapsing, if all the vertices of the initial simplex fall in a local optimization region, the simplex will be strongly confined

to this region and perform a local optimization. Due to these concerns, the size and placement of the initial simplex must be chosen wisely.

REFERENCES CITED

[1] G. Chen and A. Shakouri. Heat transfer in nanostructures for solid-state energy conversion. *J. Heat Transfer*, 124:242, April 2002.

[2] J. P. Fleurial. Thermoelectric power generation materials: technology and application opportunities. *JOM*, 61(4):79 – 85, 2009.

[3] Cronin B. Vining. An inconvenient truth about thermoelectrics. *Nature Materials*, 8(2):83 – 85, February 2009.

[4] Abram Fedorovich Ioffe. *Semiconductor thermoelements, and Thermoelectric cooling.* Infosearch, ltd., 1957.

[5] Robert R. Heikes and Roland S. Ure. *Thermoelectricity: Science and Engineering.* Interscience Publishers, 1961.

[6] K. R. Rao, editor. *Proceedings of the XI international conference on thermoelectrics*, October 1992. University of Texas at Arlington.

[7] B. Yang, W. L. Liu, J. L. Liu, K. L. Wang, and G. Chen. Measurements of anisotropic thermoelectric properties in superlattices. *Appl. Phys. Lett.*, 81(19): 3588–3590, Novem 2002.

[8] M. S. Dresselhaus, Gang Chen, Ming Y. Tang, Ronggui Yang, Hohyun Lee, Dezhi Wang, Zhifeng Ren, J. P. Fleurial, and Pawan Gogna. New directions for low-dimensional thermoelectric materials. *Adv. mater.*, 19:1043 – 1053, 2007.

[9] Akram I. Boukai, Yuri Bunimovich, Jamil Tahir-Kheli, Jen-Kan Yu, William A. Goddard, and James R. Heath. Silicon nanowires as efficient thermoelectric materials. *Nature*, 451:168 – 171, January 2008.

[10] M. Jonson and G. D. Mahan. Mott's formula for the thermopower and the wiedemann-franz law. *Phys. Lett. B*, 21(10):4223 – 4229, May 1980.

[11] N. Mingo. Thermoelectric figure of merit and maximum power factor in iii–v semiconductor nanowires. *Appl. Phys. Lett.*, 84(14):2652 – 2654, April 2004.

[12] David M.-T Kuo and Yia chung Chang. Thermoelectric and thermal rectification properties of quantum dot junctions. *Phys. Rev. B*, 81:205321, May 2010.

[13] Eric Hoffmann. *The Thermoelectric Efficiency of Quantum Dots in InAs/InP Nanowires.* PhD thesis, University of Oregon, October 2009.

[14] C. A. Domenicali. Irreversible thermodynamics of thermoelectric effects in inhomogeneous, anisotropic media. *Phys. Rev.*, 92(4):877 – 881, November 1953.

[15] G. Jeffrey Snyder and Eric S. Toberer. Complex thermoelectric materials. *Nature Materials*, 7:105 – 114, February 2008.

[16] V. P. Babin, T. S. Gudkin, Z. M. Dashevskii, L. D. Dudkin, E. K. Iordanishvili, V. I. Kaidanov, N. V. Kolomoets, O. M. Narva, and L. S. Stil'bans. Anisotropic synthetic thermoelectrics and their maximum capabilities. *Sov. Phys. Semicond.*, 8(4):478–481, April 1974.

[17] T. S. Gudkin, E. K. Iordanishvili, and E. É. Fiskind. Transverse cooling effect in a stratified medium with artificial anisotropy. *Sov. Tech. Phys. Lett.*, 4(5): 244–245, May 1978.

[18] Th. Zahner, R. Förg, and H. Lengfellner. Transverse thermoelectric response of a tilted metallic multilayer structure. *Appl. Phys. Lett.*, 73(10):1364 – 1366, September 1998.

[19] W. E. Bies, R. J Radtke, H. Ehrenreich, and E. Runge. Thermoelectric properties of anisotropic semiconductors. *Phys. Lett. B*, 65(085208), February 2002.

[20] B. Hackens, L. Gence, S. Faniel, C. Gustin, X. Wallart, S. Bollaert, A. Cappy, and V. Bayot. Tunable rectification and slope reversals in the i–v characteristics of ballistic nanojunctions. *Physica E*, 34:515 – 518, April 2006.

[21] S. de Haan, A. Lorke, J. P. Kotthaus, M. Bichler, and W. Wegscheider. Quantized transport in ballistic rectifers: sign reversal and step-like output. *Physica E*, 21:916 – 920, 2004.

[22] A. Löfgren, I Shorubalko, P. Omling, and A. M. Song. Quantum behavior in nanoscale ballistic rectifiers and artificial materials. *Phys. Rev.*, 67:195309, May 2003.

[23] Aimin M. Song. Room-temperature ballistic nanodevices. *Encyclopedia of Nanoscience and Nanotechnology*, 9(1):371 – 389, 2004.

[24] B. Hackens, L. Gence, C. Gustin, X. Wallart, S. Bollaert, A. Cappy, and V. Bayot. Sign reversal and tunable rectification in a ballistic nanojunction. *Appl. Phys. Lett.*, 85(19):4508 – 4510, November 2004.

[25] T. Christen and M. Büttiker. Gauge-invariant nonlinear electric transport in mesoscopic conductors. *Europhys. Lett.*, 35(7):523 – 528, September 1996.

[26] P. N. Butcher. Thermal and electrical transport formalism for electronic microstructures with many terminals. *J. Phys.: Condens. Matter*, 2:486 – 4878, February 1990.

[27] D.A. Pshenaĭ-Severin, Y. I. Ravich, and M. V. Vedernikov. An artificially anisotropic thermoelectric material with semiconducting and superconducting layers. *Semiconductors*, 34(10):1214–1218, April 2000.

[28] A. Kyarad and H. Lengfellner. Transverse peltier effect in tilted pb-bi_2te_3 multilayer structures. *Appl. Phys. Lett.*, 89(192103), November 2006.

[29] Lars Onsager. Reciprocal relations in irreversible processes. i. *Phys. Rev.*, 37(4): 405 – 426, February 1931.

[30] Lars Onsager. Reciprocal relations in irreversible processes. ii. *Phys. Rev.*, 38 (12):2265 – 2279, December 1931.

[31] John David Jackson. *Classical Electrodynamics*. John Wiley & Sons, Inc., 3 edition, 1999.

[32] Natthapon Nakpathomkun. *Thermoelectric properties of quantum does and other low-dimensional systems*. PhD thesis, University of Oregon, December 2010.

[33] J. C. Caylor, K. Coonley, J. Stuart, T. Colpitts, and R. Venkatasubramanian. Enhanced thermoelectric performance in pbte-based superlattice structures from reduction of lattice thermal conductivity. *Appl. Phys. Lett.*, 87:023105, July 2005.

[34] G. S. Nolas, H. Takizawa, T. Endo, H. Sellinschegg, and D. C. Johnson. Thermoelectric properties of sn-filled skutterudites. *Appl. Phys. Lett.*, 77(1):52 – 54, July 2000.

[35] Allon I. Hochbaum, Renkun Chen, Raul Diaz Delgado, Wenjie, Erik C. Garnett, Mark Najarian, Arun Majumdar, and Peidong Yang. Enhanced thermoelectric performance of rough silicon nanowires. *Nature*, 451(06381):163 – 168, January 2008.

[36] T. E. Humphrey, R. Newbury, R. P. Taylor, and H. Linke. Reversible quantum brownian heat engines for electrons. *Phys. Rev. Lett.*, 89(11):116801, September 2002.

[37] T. E. Humphrey and H. Linke. Quantum, cyclic, and particle-exchange heat engines. *Physica E*, 29:390 – 398, 2005.

[38] T. C. Harman, M. P. Walsh, B. E. LaForge, and G. W. Turner. Nanostructured thermoelectric materials. *J. Electron. Mater.*, 34(5):L19 – L22, February 2005.

[39] Terry M. Tritt and M. A. Subramanian. Thermoelectric materials, phenomena, and applications: A bird's eye view. *MRS Bull.*, 31:188 – 198, March 2006.

[40] Bed Poudel, Qing Hao, Yi Ma, Yucheng, Austin Minnich, Bo Yu, Xiao Yan, Dezhi Wang, Andrew Muto, Daryoosh Vashaee, Xiaoyuan Chen, Junming Liu, Mildred S. Dresselhaus, Gang Chen, and Zhifeng Ren. High-thermoelectric performance of nanostructured bismuth antimony telluride bulk alloys. *Science*, 320:634 – 638, May 2008.

[41] Jihui Yang and Francis R. Stabler. Automotive applications of thermoelectric materials. *J. Electron. Mater.*, 38(7):1245 – 1251, February 2009.

[42] Neil W. Ashcroft and N. David Mermin. *Solid State Physics*. Brooks Cole, 1 edition, January 1976.

[43] K. H. Goetz, D. Bimberg, A. V. Solomonov, G. F. Glinskii, and M. Razeghi. Optical and crystallographic properties and impurity incorporation of ga$_x$ln$_{1-x}$as (0.44 ¡x ¡ 0.49) grown by liquid phase epitaxy, vapor phase epitaxy, and metal organic chemical vapor deposition. *J. Appl. Phys.*, 54(8):4543 – 4552, August 1983.

[44] Thomas Heinzel. *Mesoscopic Electronics in Solid State Nanostructures*. Wiley, 2 edition, 2007.

[45] H. Linke, W. Sheng, A. Löfgren, Hongqi Xu, P. Omling, and P. E. Lindelof. A quantum dot ratchet: Experiment and theory. *Europhys. Lett.*, 44(3):341 – 347, September 1998.

[46] Colleen Marlow. *Electronic Quantum Interference in Semiconductor Billards*. Ph.d., University of Oregon, August 2005.

[47] M. Büttiker. Four-terminal phase-coherent conductance. *Phys. Rev. Lett.*, 57 (14):1761 – 1764, October 1986.

[48] M. Henny, S. Oberholzer, C. Strunk, and C. Schönenberger. 1/3-shot-noise suppression in diffusive nanowires. *Phys. Rev. B*, 59(4):2871 – 2880, January 1999.

[49] A. G. Pogosov, M. V. Budanstev, D. Uzur, A. Nogaret, A. E. Plotnikov, A. K. Bakarov, and A. I. Toropov. Thermopower of a multiprobe ballistic conductor. *Phys. Rev. B*, 66:201303(R), November 2002.

[50] Maxim G. Vavilov and A. Douglas Stone. Failure of the wiedemann-franz law in mesoscopic conductors. *Phys. Rev. B*, 72:205107, November 2005.

[51] Luis G. C. Rego and George Kirczenow. Quantized thermal conductance of dielectric quantum wires. *Phys. Rev. Lett.*, 81(1):232 – 235, July 1998.

[52] Andreas Greiner, Lino Reggiani, Tilmann Kuhn, and Luca Varani. Thermal conductivity and lorenz number for one-dimensional ballistic transport. *Phys. Rev. Lett.*, 78(6):1114 – 1117, February 1997.

[53] A. Greiner, L. Reggiani, and T. Kuhn. Comment on “quantized thermal conductance of dielectric quantum wires”. *Phys. Rev. Lett.*, 81(22):5037, November 1998.

[54] Luis G. C. Rego and George Kirczenow. Rego and kirczenow reply. *Phys. Rev. Lett.*, 81(22):5038, November 1998.

[55] Luis G. C. Rego and George Kirczenow. Fractional exclusion statistics and the universal quantum of thermal conductance: A unifying approach. *arXiv:cond-mat/9810016v1*, October 1998.

[56] P. Ramvall, N. Carlsson, P. Omling, L. Samuelson, W. Seifret, M. Stolze, and Q. Wang. Ga0.25in0.75as/inp quantum wells with extremely high and anisotropic two-dimensional electron gas mobilities. *Appl. Phys. Lett.*, 68(8): 1111 – 1113, February 1996.

[57] M. Larsson, D. Wallin, and H. Q. Xu. A highly tunable lateral quantum dot realized in ingaas/inp by an etching technique. *J. Appl. Phys.*, 103:086101, April 2008.

[58] Srijit Goswami, Christoph Siegert, Michael Pepper, Ian Farrer, David A. Ritchie, and Arindam Ghosh. Signatures of an anomalous nernst effect in a mesoscopic two-dimensional electron system. *Phys. Rev. B*, 83:073302, February 2011.

[59] Eric A. Hoffmann, Henrik A. Nilsson, Jason E. Matthews, Natthapon Nakpathomkun, Ann I. Persson, Lars Samuelson, and Heiner Linke. Measuring temperature gradients over nanometer length scales. *Nano Lett.*, 9(2):779–783, November 2009.

[60] Aimin M. Song, Pär Omling, Lars Samuelson, Werner Seifert, Ivan Shorubalko, and Herbert Zirath. Operation of ingaas/inp-based ballistic rectifiers at room temperature and frequencies up to 50 ghz. *Jpn. J. Appl. Phys.*, 40:909 – 911, July 2001.

[61] A. M. Song. Electron ratchet effect in semiconductor devices and artificial materials with broken centrosymmetry. *Appl. Phys. A*, 75(2):229 – 235, April 2002.

[62] M. Büttiker and D. Sánchez. Comment on “mesoscopic rectifiers based on ballistic transport”. *Phys. Rev. Lett.*, 90(11):119701, March 2003.

[63] Th. Zahner, R. Schreiner, R. Stierstorfer, O. Kus, S. T. Li, R. Roessler, J. D. Pedarnig, D. Bäuerle, and H. Lengfellner. Off-diagonal seebeck effect and anisotropic thermopower in $bi_2sr_2cacu_2o_8$ thin films. *Europhys. Lett.*, 40(6):673 – 678, December 1997.

[64] Th. Zahner, Ch. Stoiber, E. Zepezauer, and H. Lengfellner. Transverse thermoelectricity in a tilted metallic multilayer structure. *Int. J. Infrared Milli.*, 20(6):1103 – 1111, March 1999.

[65] K. Fischer, C. Stoiber, A. Kyarad, and H. Lengfellner. Anisotropic thermopower in tilted metallic multilayer structures. *Appl. Phys. A*, 78:323–326, March 2004.

[66] A. Kyarad and H. Lengfellner. Al–si multilayers: A synthetic material with large thermoelectric anisotrop. *Appl. Phys. Lett.*, 85(23), December 2004.

[67] A. Kyarad and H. Lengfellner. Angle-dependent photovoltaic effect in al–si multilayers. *Appl. Phys. Lett.*, 87:182113, October 2005.

[68] Rebekah Ann Derryberry. Artificial anisotropy for transverse thermoelectric heat flux sensing. Master's thesis, Virginia Polytechnic Institute and State University, April 2007.

[69] T. S. Gudkin, E. K. Iordanishvili, and E. É. Fiskind. Theory of an anisotropic thermoelectric cooling unit. *Sov. Phys. Semicond.*, 11(9):1048–1051, September 1977.

[70] A. E. Hansen, M. T. Björk, C. Fasth, C. Thelander, and L. Samuelson. Spin relaxation in inas nanowires studied by tunable weak antilocalization. *Phys. Rev. B*, 71(20):205328, May 2005.

[71] T. Sugaya, J. P. Bird, D. K. Ferry, A. Sergeev, V. Mitin, K. Y. Jang, M. Ogura, and Y. Sugiyama. Experimental studies of the electron–phonon interaction in ingaas quantum wires. *Appl. Phys. Lett.*, 81(4):727 – 729, July 2002.

[72] S. Kubakaddi. Electron-phonon interaction in a quantum wire in the bloch-gruneisen regime. *Phys. Rev. B*, 75(075309), February 2007.

[73] M. Prunnila. Electron–acoustic-phonon energy-loss rate in multicomponent electron systems with symmetric and asymmetric coupling constants. *Phys. Rev. B*, 75:165322, April 2007.

[74] Feng Zhou, Arden L. Moore, Jessica Bolinsson, Ann Persson, Linus Fröberg, Michael T. Pettes, Huijun Kong, Lew Rabenberg, Philippe Caroff, Darek A. Stewart, Natalio Mingo, Kimberly A. Dick, Lars Samuelson, Heiner Linke, and Li Shi. Thermal conductivity of indium arsenide nanowires with wurtzite and zinc blende phases. *Phys. Rev. B*, 83:205416, May 2011.

[75] Mikael Bjork. *Electron Transport in Semiconductor Nanowires.* PhD thesis, Lund Institue of Technology, Lund University, P. O. Box 118, SE-221 00 Lund, September 2004.

[76] Aveek Bid, Achyut Bora, and A. K. Raychaudhuri. Temperature dependence of the resistance of metallic nanowires of diameter ¿15 nm: Applicability of bloch-grüneisen theorem. *Phys. Rev. B*, 74:035426, August 2006.

[77] X. Zhou, S. A. Dayeh, D. Aplin, D. Wang, and E. T. Yu. Direct observation of ballistic and drift carrier transport regimes in inas nanowires. *Appl. Phys. Lett.*, 89:053113, August 2006.

[78] Shadi A. Dayeh, Edward T. yu, and Deli Wang. Transport coefficients of inas nanowires as a function of diameter. *Small*, 5(1):77 – 81, 2009.

[79] Feng Zhou, Ann Persson, Lars Samuelson, Heiner Linke, and Li Shi. Thermal resistance of a nanoscale point contact to an indium arsenide nanowire. *Appl. Phys. Lett.*, 99(063110), August 2011.

[80] E. A. Hoffmann, N. Nakpathomkun, A. I. Persson, H. Linke, H. A. Nilsson, and L. Samuelson. Quantum-dot thermometry. *Appl. Phys. Lett.*, 91(252114), December 2007.

[81] J. P. Small, Li Shi, and Philip Kim. Mesoscopic thermal and thermoelectric measurements of individual carbon nanotubes. *Solid State Commun.*, 127: 181–186, March 2003.

[82] K. Schwab, E. A. Henrikson, J. M. Worlock, and M. L. Roukes. Measurement of the quantum of thermal conductance. *Nature*, 404:974 – 977, April 2000.

[83] Deyu Li, Yiying Wu, Philip Kim, Li Shi, Peidong Yang, and Arun Majumdar. Thermal conductivity of individual silicon nanowires. *Appl. Phys. Lett.*, 83(14): 2934 – 2936, October 2003.

[84] Renkun Chen, Allon I. Hochbaum, Padraig Murphy, Joel Moore, Peidong Yang, and Arun Majumdar. Thermal conductance of thin silicon nanowires. *Phys. Rev. Lett.*, 101(105501), September 2008.

[85] Yu. A. Kosevich and A. V. Savin. Reduction of phonon thermal conductivity in nanowires and nanoribbons with dynamically rough surfaces and edges. *Europhys. Lett.*, 88(1), October 2009.

[86] R. C. Zeller and R. O. Pohl. Thermal conductivity and specific heat of noncrystalline solids. *Phys. Rev. B*, 4(6):2029 – 2041, May 1971.

[87] R. B. Stephens. Low-temperature specific heat and thermal conductiviy of noncrystalline dielectric solids. *Phys. Rev. B*, 8(6):2896 – 2905, September 1973.

[88] D. H. Santamore and M. C. Cross. Effect of phonon scattering by surface roughness on the universal thermal conductance. *Phys. Rev. Lett.*, 87(11): 115502, September 2001.

[89] D. H. Santamore and M. C. Cross. Effect of surface roughness on the universal thermal conductance. *Phys. Rev. B*, 63:184306, April 2001.

[90] Pierre Martin, Zlatan Aksamija, Eric Pop, and Umberto Ravaioli. Impact of phonon-surface roughness scattering on thermal conductivity of thin si nanowires. *Phys. Rev. Lett.*, 102:125503, March 2009.

[91] Davide Donadio and Giulia Galli. Atomistic simulations of heat transport in silicon nanowires. *Phys. Rev. Lett.*, 102:195901, May 2009.

[92] D. Y. Petrovykh, M. J. Yang, and L. J. Whitman. Chemical and electronic properties of sulfur-passivated inas surfaces. *Surf. Sci.*, 523:231 – 240, October 2003.

[93] R. P. Wang, G. Xu, and P. Jin. Size dependence of electron-phonon coupling in zno nanowires. *Phys. Rev. B*, 69(113303), March 2004.

[94] Jenny Nelson. *The Physics of Solar Cells*. Inperial College Press, 2009.

[95] Ho and et al. Thermal conductivity of the elements. *J. Phys. Chem. Ref. Data*, 1(2):182, 394, 1972.

[96] Gene Simmons and Herbert Wang. *Single crystal elastic constants and calculated aggregate properties: a handbook*. Cambridge, MA: M.I.T. P, 2 edition, 1971.

[97] J. W. Lynn, H. G. Smith, and R. M. Nicklow. Lattice dynamics of gold. *Phys. Rev. B*, 8(8):3493 – 3499, October 1973.

[98] M. Henny, H. Birk, R. Huber, C. Strunk, A. Bachtold, M Krüger, and C. Schönenberger. Electron heating effects in diffusive metal wires. *Appl. Phys. Lett.*, 71(6):773 – 775, August 1997.

[99] P. M. Echternach, M. R. Thoman, C. M. Gould, and H. M. Bozler. Electron-phonon scattering rates in disordered metallic films below 1 k. *Phys. Rev. B*, 46(16):10339–10344, October 1992.

[100] Sadao Adachi. *Handbook of Physical Properties of Semiconductors*, volume 2. Springer, 2004.

[101] Sadao Adachi. *Physical Properties of III-V Semiconductor Compounds: InP, InAs, GaAs, GaP, InGaAs, and InGaAsP*. Wiley, 1992.

[102] Stefano Roddaro, Andrea Pescaglini, Daniele Ercolani, Lucia Sorba, Francesco Giazotto, and Fabio Beltram. Hot-electron effects in inas nanowire josephson junctions. *Nano. Res.*, 4(3):259 – 265, March 2011.

[103] C. B. Satterthwaite. Thermal conductivity of normal and superconducting aluminum. *Phys. Rev.*, 125(3):873 – 876, February 1962.

[104] Ludwig Tewordt. Theory of the intrinsic electronic thermal conductivity of superconductors. *Phys. Rev.*, 129(2):657 – 663, January 1963.

[105] Francesco Giazotto, Tero T. Heikkilä, Arttu Luukanen, Alexander M. Savin, and Jukka P. Pekola. Opportunities for mesoscopics in thermometry and refrigeration: Physics and applications. *Rev. Mod. Phys.*, 78:217 – 274, January 2006.

[106] J. A. Nelder and R Mead. A simplex method for function minimization. *Computer Journal*, 7(4):308 – 313, August 1965.